

2007

Investigation of low level neutron radiation on tantalum alloys for radioisotope power system applications

Chadwick Douglas Barklay
University of Dayton

Follow this and additional works at: https://ecommons.udayton.edu/graduate_theses

Recommended Citation

Barklay, Chadwick Douglas, "Investigation of low level neutron radiation on tantalum alloys for radioisotope power system applications" (2007). *Graduate Theses and Dissertations*. 1400.
https://ecommons.udayton.edu/graduate_theses/1400

This Dissertation is brought to you for free and open access by the Theses and Dissertations at eCommons. It has been accepted for inclusion in Graduate Theses and Dissertations by an authorized administrator of eCommons. For more information, please contact mschlange1@udayton.edu, ecommons@udayton.edu.

INVESTIGATION OF LOW LEVEL NEUTRON RADIATION ON TANTALUM
ALLOYS FOR RADIOISOTOPE POWER SYSTEM APPLICATIONS

Dissertation

Submitted to

The School of Engineering

UNIVERSITY OF DAYTON

In Partial Fulfillment of the Requirements for

The Degree

Doctor of Philosophy in Materials Engineering

by

Chadwick Douglas Barklay

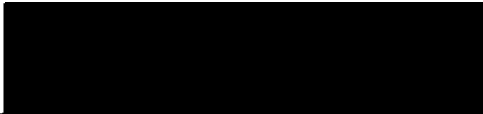
UNIVERSITY OF DAYTON


Dayton, Ohio

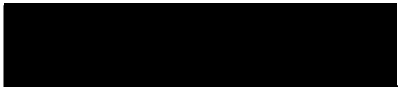
May, 2007


INVESTIGATION OF LOW LEVEL NEUTRON RADIATION ON TANTALUM
ALLOYS FOR RADIOISOTOPE POWER SYSTEM APPLICATIONS



APPROVED BY:

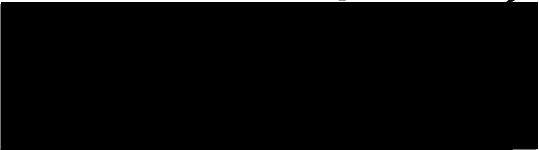

Daniel Eylon, D.Sc.
Committee Chairman
Professor and Director,
Materials Engineering


Margaret F. Pinnell, Ph.D.
Committee Member
Assistant Professor,
Mechanical Engineering


Daniel P. Kramer, Ph.D
Committee Member
Senior Scientist,
University of Dayton Research
Institute


Donald L. Moon, Ph. D.
Associate Dean
School of Engineering


P. Terrence Murray, Ph.D. 
Committee Member
Professor, Materials Engineering


Mr. Gerald Shaughnessy, M.S.
Committee Member
Associate Professor, Mathematics


Joseph E. Sariba, Ph.D., P.E.
Dean, School of Engineering

ABSTRACT

INVESTIGATION OF LOW LEVEL NEUTRON RADIATION ON TANTALUM ALLOYS FOR RADIOISOTOPE POWER SYSTEM APPLICATIONS

Barklay, Chadwick D.

University of Dayton, 2007

Dr. Daniel Kramer, Technical Advisor

Tantalum alloys have been used by the U.S. Department of Energy (USDOE) as structural materials for space nuclear power systems such as Radioisotopic Thermoelectric Generators (RTG) since the 1960s. The thrust of this thesis research is to investigate the effects of low-level neutron radiation on the mechanical and microstructural properties of two tantalum alloys, Ta-10%W and T-111 (Ta-8%W-2%Hf), which have been used to encapsulate radioactive fuel for space nuclear power systems. Ta-10%W and T-111 test specimens were exposed to a neutron fluence level (1.2×10^{15} nvt) at temperatures less than $<0.2 T_m$, which is equivalent to the cumulative fluence associated with the 30-year mission life of a RTG. This fluence level resulted in an atomic displacement damage of approximately 3.0×10^{-7} dpa in both alloys.

In T-111 test specimens, this level of atomic displacement damage produced an approximate 6.6% reduction in the tensile ductility, an approximate two-order of magnitude increase in the stress rupture time, and a two-order of magnitude reduction in steady state creep rate. These observations are statistically significant at the 0.05 significance level. Through the employment of Transmission Electron Microscopy it was determined that the interaction of the defects produced by atomic displacement damage with moving $a_0/2\langle 111 \rangle$ screw dislocations increased the magnitude of cross-slip of the screw dislocations, thus leading to a five-fold increase in dislocation density and a pronouncement of the ordering of dislocations into mosaic patterns of cellular or subgranular arrangements at the boundaries of cells/subgrains. In addition, the experimental results determined that an atomic displacement damage of approximately 3.0×10^{-7} dpa did not produce a statistically significant effect on the mechanical or microstructural properties of Ta-10%W when subjected to a strain rate of 0.0017 s^{-1} .

The culmination of this research is the development of a phenomenological model based on the experimental data that can be used to determine the minimum creep rate of irradiated T-111 within the parameters bounded by this research. The results of this research are significant because they provide a basic understanding of the strength mechanisms in two tantalum alloys (Ta-10%W and T-111) resulting from neutron radiation at temperatures $< 0.2 T_m$. This greatly enhances the level of understanding of potential irradiation hardening

mechanisms in both alloys. Thus, space power system designers can more confidently extrapolate relevant mechanical-property trends of T-111 and Ta-10%W encapsulation materials as a function of neutron irradiation doses and internal pressure levels which correspond to actual RTG service lifetimes.

ACKNOWLEDGEMENTS

I would like to express my utmost gratitude to the three individuals who made my graduate education successful. They have shown continued support, guidance, and encouragement during this research.

To Amy, my wife and best friend, thank you for your continued love, support, and understanding of the pressures of graduate school. I love you.

To my advisor, Dr. Daniel Kramer, I am eternally grateful for the opportunity to work with him again. His expertise, encouragement, mentorship and countless hours of discussions were pivotal in getting me to this point.

To my committee chair, Dr. Daniel Eylon, thank you for urging me to continue my graduate education.

I am grateful to the Dayton Area Graduate Studies Institute (DAGSI) whose financial and functional support made the pursuit of a Ph.D. possible. I would also like to thank Mr. Timothy Frazier of the USDOE and Dr. Bill Moddeman of BWXT Pantex without whose support none of this research would have been possible. I would also like to thank Dr. Larry Allard, Dr. James Bentley, Dr. Jane Howe, Loy (Gib) Gibson and Dorothy Coffey of Oak Ridge National Laboratory

for their TEM expertise; Steve Goodrich, Dale Grant, Carl Sjoblom and Mike Gonzales, of the University of Dayton Research Institute for their mechanical testing support; Robin Oldfield and Mark Fuchs of the University of Dayton Safety Department for their continuous support; Joseph Talnagi, Kevin Herminghuysen and Andrew Kauffman of the Ohio State University Research Reactor Laboratory for their invaluable assistance before, during and after the irradiation of the specimens used in this study. Many thanks to Robert Stringer, Scott McBride, and Gregg Moedl of Idaho National Laboratory for their invaluable assistance along the way.

Finally, I would like to pay tribute to a fellow graduate student that always inspired me; G. Sean Crossman. May his family always remember how he loved them and take comfort in the fact that he always inspired others around him with his passion.

This research was sponsored in part by the Office of Nuclear Energy, US Department of Energy, under grant DE-FG07-05ID14642 with the University of Dayton Research Institute.

TABLE OF CONTENTS

ABSTRACT	iii
ACKNOWLEDGEMENTS	vi
TABLE OF CONTENTS	viii
LIST OF FIGURES	xiii
LIST OF TABLES	xvii
LIST OF SYMBOLS, ABBREVIATIONS, AND SPECIAL NOMENCLATURE ..	xix
INTRODUCTION	1
1.1 Tantalum	6
1.2 Tantalum-Tungsten Alloys	8
1.3 Mechanical Properties of T-111 and Ta-10%W	10
1.4 Creep of Materials	13
1.5 Low-Temperature Creep	17
1.5.1 Cross Slip	17
1.5.2 Intersection of Dislocations	19
1.5.3 Lattice Friction	19
1.5.4 Dislocation-Point Defect Interaction.....	20
1.5.5 Review.....	21
1.6 Radiation Effects on Materials	22
1.6.1 Atomic Displacement.....	23
1.6.2 Impurity Production	24

1.7 Summary 27

LITERATURE REVIEW 28

2.1 Overview 28

2.2 Effects of Neutron Irradiation on Metals 30

2.3 Effects of Neutron Irradiation on Tantalum Alloys 33

2.4 Experimental Motivation 36

RESEARCH OBJECTIVES 38

3.1 Thesis Statement..... 40

EXPERIMENTAL METHODS 41

4.1 Material Characterization..... 41

4.1.1 Grain Size..... 42

4.1.2 Microhardness..... 44

4.1.3 Recrystallization State 45

4.2 Test Specimen Preparation 48

4.3 Test Specimen Cleaning 50

4.4 Oxidation Behavior Determination 52

4.4.1 Experimental Procedure 53

4.5 Test Specimen Irradiation..... 55

4.5.1 Determination of Irradiation Parameters..... 55

4.5.2 Irradiation Facility 56

4.5.3 Test Specimen Irradiation 57

4.5.4 Gamma Spectrometry 62

4.5.5 Safety 63

4.6 Tensile Testing	66
4.6.1 Set-up	66
4.6.2 Experimental Design Matrix	68
4.6.3 Testing	70
4.7 Low-Temperature Creep/Stress Rupture.....	72
4.7.1 Background	72
4.7.2 Experimental Design Matrix	73
4.7.3 Creep/Stress Rupture Testing.....	75
4.8 Scanning Electron Fractography	77
4.8.1 Sample Preparation.....	77
4.9 Transmission Electron Microscopy	79
4.9.1 Background	79
4.9.2 Sample Preparation.....	81
RESULTS AND DISCUSSION	84
5.1 Oxidation Experiments of Ta-10%W and T-111	85
5.1.1 Weight Changes of Ta-10%W and T-111 at 300°C and 400°C	85
5.1.2 Effects of the Irradiation Environment on T-111.....	88
5.1.3 Summary	89
5.2 Gamma Spectrometry	91
5.3 Neutron Damage.....	92
5.3.1 Total Flux Determination	92
5.3.2 Displacement Damage Calculation.....	94
5.3.3 Discussion	95

5.3.4 Visible Defect Density	97
5.4 Tensile Testing of Irradiated and Non-irradiated Specimens	101
5.4.1 Discussion	105
5.5 Low Temperature Creep/Stress Rupture Testing of Irradiated and Non-irradiated Specimens	107
5.6 Development of Steady-State Creep Model	113
5.6.1 Apparent Activation Energy for Creep	113
5.6.2 Stress Function Determination	116
5.6.3 Minimum Creep Rate Equations	122
5.6.4 Correlation of Minimum Creep Rate and Radiation Damage...	123
5.6.5 Discussion	125
5.7 Scanning Electron Microscope Fractography	126
5.7.1 Fractography of Ta-10%W	127
5.7.2 Fractography of T-111.....	128
5.7.3 Discussion	130
5.8 Transmission Electron Microscopy	132
5.8.1 Microstructural Analysis of T-111.....	132
5.8.2 Microstructural Analysis of Ta-10%W	136
5.8.3 Dislocation Density Discussion	139
5.8.4 Evolution of Dislocation Structure	141
SUMMARY AND CONCLUSIONS	145
6.1 Summary	145
6.2 Conclusions.....	148

FUTURE RESEARCH 152

REFERENCES 154

APPENDIX A Gamma Spectrometry Data 164

APPENDIX B Tensile Test ANOVA Data..... 167

APPENDIX C Creep/Stress Rupture Test ANOVA Data 184

DISCLAIMER 191

LIST OF FIGURES

Figure 1.0.1. Alan Bean removing the SNAP-27 on the Apollo 12 mission in November 1969.	1
Figure 1.0.2. Cutaway of the SNAP-27 RTG. The converter was 46.0 cm high and 40.0 cm across the fins and produced 63.5 We with a mass of 19.6 kg.	3
Figure 1.1.1. Periodic Table of the Elements Highlighting Hafnium, Tantalum and Tungsten.	7
Figure 1.3.1. Effect of Test Temperature on Tensile Properties of Recrystallized Ta-10%W and T-111 Sheet Material.	11
Figure 1.3.2. Effect of Test Temperature on the Percent Elongation of Recrystallized Ta-10%W and T-111 Sheet Material.	12
Figure 1.4.1. Generic creep curve showing the three stages of creep.....	15
Figure 1.5.1. Cross Slip of a Screw Dislocation.	18
Figure 1.5.2. Slip systems in bcc materials.....	18
Figure 1.6.1. The interaction of ionizing radiation with materials.	23
Figure 1.6.2. Displacement damage created by an incident neutron on a material lattice.	24
Figure 1.6.3. Reaction path of the s-process in the region of the Hf, Ta and W isotopes.	25
Figure 2.1.1. Tensile Elongations of Ta-10%W after Neutron Irradiation at 70°C.	29
Figure 4.1.1. Photomicrograph of Representative Ta-10%W Sample Microstructure.....	43
Figure 4.1.2. Photomicrograph of Representative T-111 Sample Microstructure.....	44
Figure 4.1.3. Effect of Annealing on Hardness of Ta-10%W.....	46

Figure 4.1.4. Effect of Annealing on Hardness of T-111.	47
Figure 4.2.1. A section of sheet material after WEDM of mechanical test specimens and "cutouts."	49
Figure 4.5.1. The OSURR at full power.	56
Figure 4.5.2. A) OSURR at full power with AIC shown in foreground; B) Watlow ceramic heater with thermocouples and electric cabling attached.....	59
Figure 4.5.3. The PI lowering the cadmium wrapped experiment package into the AIC at the OSURR.....	61
Figure 4.6.1. Instron 55R1122 Tensile Test Machine.	67
Figure 4.6.2. Instron 2712-015 Pneumatic Side Action Grips.	68
Figure 4.6.3. Watlow MB1A1JN2-C12 Band Heater.	71
Figure 4.7.1. ATS model 2370 creep/stress rupture test system.	76
Figure 4.8.1. JEOL JSM-840 SEM.....	78
Figure 4.9.1. HF-2000 FEG-TEM.....	80
Figure 5.1.1. Oxidation Weight Gains of Ta-10%W and T-111 in Air.....	87
Figure 5.1.2. Oxidation Rate of Ta-10%W and T-111 in Air.....	87
Figure 5.1.3. Low-temperature creep/stress rupture results of two T-111 specimens tested at 25°C with a load of 620 MPa.	89
Figure 5.1.3. Differential Flux versus Energy of Research Experiment Package in the OSURR at 450 KW.	93
Figure 5.3.2. Observable Defect Density versus Displacement Damage for Fe, Ta, Ta-10%W and T-111.....	99
Figure 5.4.1. Tensile test results of irradiated and non-irradiated Ta-10%W samples. The samples with a failure strain of 15% were tested at 300°C; samples with a failure strain of approximately 25% were tested at 25°C.....	102
Figure 5.4.2. Tensile test results of irradiated and non-irradiated T-111 samples. The samples with a failure strain between 22-26% were tested at 300°C; samples with a failure strain between 29- 35% were tested at 25°C.....	104

Figure 5.4.3. Tensile elongation vs. displacement damage (dpa) behavior of Ta-10%W and T-111. The dashed lines represent the Primary Investigator's hypothesized behavior of both alloys.....	106
Figure 5.5.1. Creep/stress rupture test results of irradiated (8B/10A) and non-irradiated (5A/5B) Ta-10%W samples tested at 25°C with a load of 100 ksi.	109
Figure 5.5.2. Creep/stress rupture test results of irradiated (T4A) and non-irradiated (T1A/T1B) T-111 samples tested at 25°C with a load of 90 ksi.	110
Figure 5.6.1. Determination of Apparent Activation Energy for Creep of Irradiated and Non-irradiated T-111.	114
Figure 5.6.2. Determination of Apparent Activation Energy for Creep of Irradiated and Non-irradiated Ta-10%W.....	115
Figure 5.6.3. Variation of Temperature Compensated Strain Rate with $[\sinh(\alpha\sigma)]^n$ for Irradiated T-111.....	118
Figure 5.6.4. Variation of Temperature Compensated Strain Rate with $[\sinh(\alpha\sigma)]^n$ for Non-irradiated T-111.	119
Figure 5.6.5. Variation of Temperature Compensated Strain Rate with $[\sinh(\alpha\sigma)]^n$ for Irradiated Ta-10%W.	120
Figure 5.6.6. Variation of Temperature Compensated Strain Rate with $[\sinh(\alpha\sigma)]^n$ for Non-irradiated Ta-10%W.....	121
Figure 5.7.1. SEM photomicrograph of fracture surface of a rupture tested non-irradiated Ta-10%W sample (5C).	127
Figure 5.7.2. SEM photomicrograph of fracture surface of a rupture tested non-non-irradiated Ta-10%W sample (8C).	128
Figure 5.7.3. SEM photomicrograph of fracture surface of a rupture tested non-irradiated T-111 sample (T1C).	129
Figure 5.7.4. SEM photomicrograph of fracture surface of a rupture tested irradiated T-111 sample (T4C).	129
Figure 5.7.5. Slip step formation resulting in serpentine glide and ripples on a dimple wall.....	131
Figure 5.8.1. Bright field TEM image of recrystallized T-111.	132

Figure 5.8.2. Bright field TEM image and electron diffraction pattern of a rupture tested non-irradiated T-111 sample. 133

Figure 5.8.3. Reference [112] zone-axis diffraction pattern and stereogram centered on [112]..... 134

Figure 5.8.4. Bright field TEM image of a rupture tested irradiated T-111 sample..... 135

Figure 5.8.5. Bright field TEM image of recrystallized Ta-10%W..... 136

Figure 5.8.6. Bright field TEM image of a rupture tested non-irradiated Ta-10%W sample. 137

Figure 5.8.7. Bright field TEM image of a rupture tested irradiated Ta-10%W sample..... 138

Figure A.1. Gamma-spectrometry Results for Irradiated Ta-10%W Mechanical Test Specimen 8C..... 165

Figure A.2. Gamma-spectrometry Results for Irradiated T-111 Mechanical Test Specimen T6C..... 166

LIST OF TABLES

Table 1.2.1. Physical properties of tantalum, Ta-10%W and T-111.	8
Table 1.2.2. Specification for the Composition of Tantalum, Ta-10%W and T-111 (ppm wt. %).	9
Table 1.3.1. Mechanical Properties of Recrystallized T-111 and Ta10%W at 25°C.	10
Table 1.6.1. Half-life, decay mode, decay energy and daughter nucleus of the created Hf, Ta and W isotopes.	26
Table 4.1.1. Specification for composition of Tantalum, Ta-10%W and T-111 (ppm wt. %).	42
Table 4.1.2. ASTM Grain Size of the Materials used in this Research.	43
Table 4.1.3. Vickers Harness of the Materials used in this Research.....	45
Table 4.5.1. Grouping of the experimental runs for the OSURR.	58
Table 4.6.1. The 2^4 full factorial design of experiments matrix.	69
Table 4.7.1. The $2v^{5-1}$ fractional factorial design of experiments matrix.....	74
Table 5.1.1. Data of oxidation experiments on Ta-10%W and T-111 at 300°C and 400°C.....	86
Table 5.3.1. Irradiated Materials Data and dpa Calculation for Ta-10%W and T-111.	95
Table 5.4.1. Tensile test results. * Note: 108°C is the result of self heating during irradiation.....	101
Table 5.5.1. Creep/stress rupture test results. Notes: * denotes, due to self-heating during irradiation; ** denotes, did not fail.	107
Table 5.6.1. Apparent Activation Energies for Creep of Irradiated and Non-irradiated T-111 and Ta-10%W.	115
Table 5.6.2. Calculated variables associated with equation 5.6.1.	117

Table 5.8.1. Dislocation density (m^{-2}) of T-111 and Ta-10%W in varying conditions. 139

LIST OF SYMBOLS, ABBREVIATIONS, AND SPECIAL NOMENCLATURE

$\bar{\sigma}_d$	The displacement cross section for a particular material (barns)
ψ	Normalized fluence rate (n/cm ²)
η	Averaged defect production efficiency
σT_{dam}	Averaged damage energy cross-section (barns-keV)
ϕ_{tot}	The total neutron flux of (n/cm ² -s)
(xyz)	Miller indices of a crystallographic plane
{xyz}	Miller indices of a family of crystallographic planes
<xyz>	Miller indices of a family of crystallographic equivalent directions
²³⁸ PuO ₂	Plutonium-238 dioxide
ANOVA	Analysis of variance, a statistical test used to detect differences in two or more means and can analyze the effect of multiple independent variables on one or more dependent variables
atm	Standard atmosphere, a unit of pressure
barn	A unit of nuclear cross section; the effective circular area that one particle presents to another as a target for an encounter. One barn equals 10 ⁻²⁴ cm ²
°C	Celsius
Ci	Curie, the unit used to describe the intensity of radioactivity in a sample of material. The curie is equal to 3.7 x 10 ¹⁰ disintegrations per second
DBTT	Ductile to brittle transition temperature

DIC	Differential interference contrast, a method of contrast microscopy that yields images with a shadowy, three-dimensional relief effect.
dpa	Displacements per atom, equals the average number of displacements per lattice atom for a given fluence
$\dot{\epsilon}$	Secondary or steady state creep rate, (m/s)
E_c	Apparent activation for creep (kJ/mole)
E_d	Effective threshold displacement energy (keV)
Epithermal Neutrons	Neutrons with a kinetic energy greater than that of thermal agitation.
eV	Electron-Volts, amount of energy gained by a single unbound electron when it falls through an electrostatic potential difference of one volt
F-test	An overall statistical test of the null hypothesis that group means of the dependent variables do not differ. It is also used to test the significance of each main and any interaction effects.
fluence	The product (or integral) of particle or radiation flux and time, expressed in units of particles or energy per square centimeter (nvt)
flux	The number of neutrons passing through a unit area in unit time
ft	Feet
g	Gram
hr	Hour
in	Inch
J	Joules = 1 Newton-meter = $1 \text{ kg-m}^2 \text{ s}^{-2}$
K	Kelvin
keV	Kilo-electron volts

ksi	Kilo-pounds per square inch
kV	Kilo-Volt
kW	Kilo-watt
LEM	Lunar Excursion Module
m	Meter
m/s	Meters per second
MeV	Mega-electron volts
MPa	Mega-Pascals
n	Neutron, as expressed in n/cm^2 for nvt or n/cm^2 -s for nv
nm	Nano-meter
nv	Unit measure of flux in n/cm^2 -sec
nv	Neutron flux (n/cm^2 -s)
nvt	Unit measure of fluence in n/cm^2
nvt	Neutron fluence rate (n/cm^2)
p	A statistical significance level which indicates the probability that the differences observed in the data is due to chance
PI	Primary Investigator
Plutonium-238	A radioactive isotope of plutonium with a half-life of 86.41 years
ppm	Parts per million
R	Universal Gas Constant = $8.3145 \text{ J mol}^{-1} \text{ K}^{-1}$
Radiogenic	A nuclide that is produced by a process of radioactive decay
RCA	Radiation Control Areas

rem	Roentgen equivalent man, a unit used in radiation protection to measure the amount of damage to human tissue from a dose of ionizing radiation
RTG	Radioisotopic Thermoelectric Generator
s	Second
SNAP	System for Nuclear Auxiliary Power, an early generation RTG
t	Irradiation time (s)
T-111	Tantalum – 8 wt.% Tungsten – 2 wt.% hafnium
Ta-10%W	Tantalum – 10 wt.% Tungsten
T _m	Homologous temperature in Kelvin
torr	Vacuum level with a scale of 0 to 760 torr with 760 being equal to atmospheric pressure at sea level
USDOE	U.S. Department of Energy
UTS	Ultimate tensile strength
V	Volts
W	Watts
W _e	Watts-electric
W _t	Watts-thermal
wt. %	Weight percent
Zone axis	A straight line passing through the center of a crystal, to which all the planes of a given zone are parallel
γ	Gamma radiation, electromagnetic radiation characterized as having the highest frequency and energy, and also the shortest wavelength
μm	Micro-meter, 10 ⁻⁶ m

CHAPTER I

INTRODUCTION

"There is no such thing as a new idea. We simply take a lot of old ideas and put them into a mental kaleidoscope. We give them a turn and they make new and curious combinations." - Mark Twain

Radioisotope Thermoelectric Generators, commonly referred to as RTGs, provide electric power to spacecraft through the thermoelectric conversion of the decay heat of the radioactive isotope Plutonium-238. The electric power produced by the RTGs has powered the instruments, computers, radio transmitters and attitude thrusters on various spacecraft and has powered lunar seismic experiments.¹ Figure 1.0.1 shows astronaut Alan Bean removing the

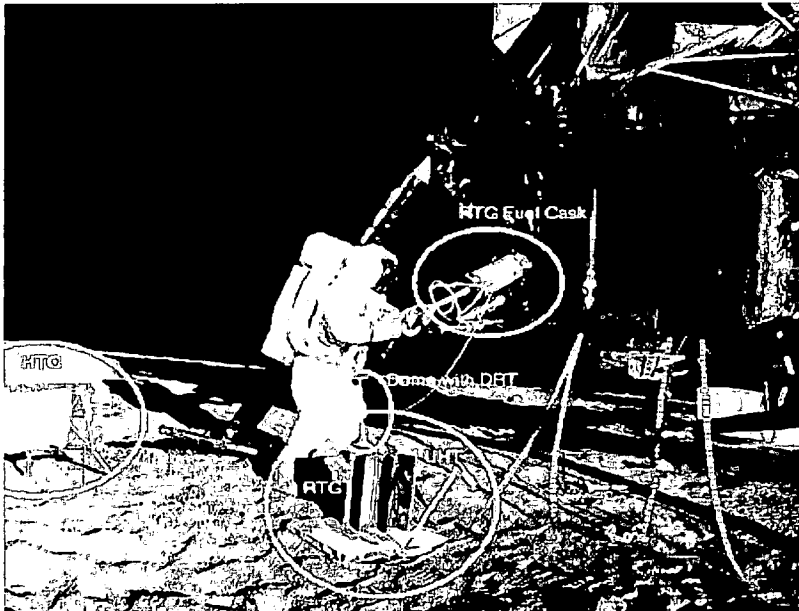


Figure 1.0.1. Alan Bean removing the SNAP-27 on the Apollo 12 mission in November 1969.

Plutonium-238 heat source from the Apollo Lunar Excursion Module (LEM) which was used to power a SNAP-27 (Systems for Nuclear Auxiliary Power) RTG used for lunar seismic experiments.

The first RTG was put into service for a space application in June 1961, on a Navy navigational satellite. Advances in RTG systems were made with the development and flight of SNAP 19 (Systems for Nuclear Auxiliary Power) aboard Nimbus III, launched in April 1969. The SNAP 19 represented a major milestone in the development of long-lived, highly reliable isotope power systems for space use by NASA.² The SNAP 27 generator was developed to power five seismic experiments left on the Moon by the Apollo 12, 14, 15, 16 and 17 astronauts.¹ Figure 1.0.2 shows a cutaway of a SNAP-27 RTG, which uses a tantalum alloy to encapsulate the plutonium-238 heat source. The continuing operation of these generators provided new dimensions of data about the Moon and the universe. Four SNAP 19 nuclear generators later provided the electrical power for each of the two NASA Jupiter flyby spacecraft known as Pioneers 10 and 11, which were launched in the early 1970s.²

The United States has an outstanding record of safety in using RTGs on 24 missions over the past three decades.³ While RTGs have never caused a spacecraft failure on any of these missions, they have been on-board three missions which experienced malfunctions for other reasons. In all cases, the RTGs performed as designed. More than 30 years have been invested in the engineering, safety analysis and testing of RTGs. Safety features are

incorporated into the RTGs' design and extensive testing has demonstrated that they can withstand physical conditions more severe than those expected from most accidents.³

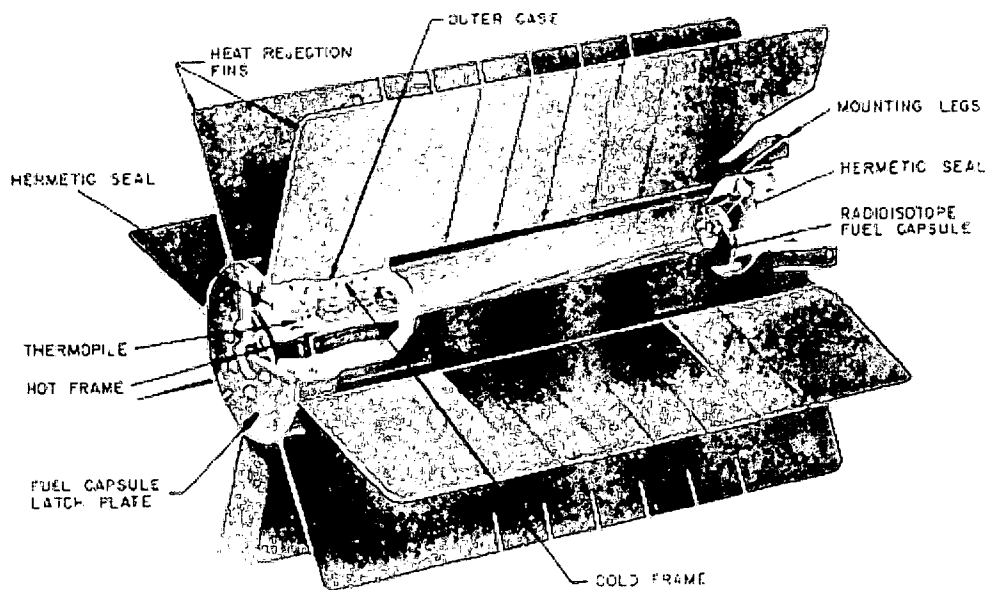


Figure 1.0.2. Cutaway of the SNAP-27 RTG. The converter was 46.0 cm high and 40.0 cm across the fins and produced 63.5 We with a mass of 19.6 kg.

Any penetrating radiation that escapes a RTG heat source is of potential concern. RTG safety efforts revolve around containing the radioactive fuel in case of an accident during a critical time in the mission, such as launch or re-entry. Multiple layers of special material, such as tantalum alloys, encapsulate the plutonium-238 fuel to contain it under both normal and accident conditions.

Extensive testing and analysis have been conducted to demonstrate that the encapsulated Plutonium-238 fuel remains intact even after Earth re-entry and impact. The Apollo 13 accident and subsequent re-entry of the RTG, without any

material release, provides further proof of this safety principle.³ The primary objective in the qualification testing of an encapsulation layer for the plutonium-238 fuel is to select tests that will demonstrate the ability of the design to withstand Earth re-entry and impact. Some of the qualification tests include: 1) external hydrostatic pressure tests of 100 MPa to determine capsule survivability if subjected to deep sea pressure;²⁴ 2) impact tests up to 150 meters per second to determine capsule survivability in the event of a transportation accident;²⁴ and 3) internal pressure stress rupture tests at various temperatures and pressures to determine capsule survivability in the event of a fire.²⁴ This type of rigorous testing and analysis also includes a full characterization of the materials used in the design of the plutonium-238 fuel encapsulation layer. These tests include: chemical and microstructural analysis, tensile, yield elongation, modulus, hardness and low and high temperature creep/stress rupture.

However, all of this extensive testing and analysis has failed to take into consideration any possible effects of the radiation emitted from the plutonium-238 fuel on the mechanical properties of the materials used to fabricate the encapsulation layer. This is primarily because the prevailing assumption regarding the effects of low fluence levels of neutron radiation, emitted by the plutonium-238 fuel in RTGs, produces correspondingly negligible levels of irradiation damage in the encapsulation materials.

Tantalum is a metal with a high-melting temperature and a good combination of properties that make it useful for a number of applications. It has already gained acceptance in electronic components, chemical equipment, missile technology²⁵ and its alloys have been used extensively in the encapsulation of the Plutonium-238 fuel used in RTGs.^{24, 26}

The following sections are intended to provide sufficient background regarding the primary focus of this research during the investigation of the effects of low level neutron radiation on the two primary tantalum alloys (Ta-10%W and T-111) used to encapsulate ²³⁸PuO₂ fuel in some radioisotope power system applications.

1.1 Tantalum

Refractory metals consist of those elements that have a bcc crystal lattice structure, a melting point of 2000°C or greater and a ratio of less than 1 for the melting point of their primary oxide to the melting point of the elemental metal.⁴ This definition applies to niobium, molybdenum, tungsten and tantalum which are in Group VA and VIA of the Periodic Table (Figure 1.1.1). Titanium, zirconium and hafnium are considered reactive metals which have an hcp crystal lattice structure and are in Group IVA of the Periodic Table.⁴

Compared to other elements, tantalum has a high melting point (2996°C), which is second only to tungsten (3410°C). Tantalum's tolerance for interstitial elements and high-solid solubility for other refractory and reactive metals, and its relatively high modulus of elasticity (186 GPa) are attractive characteristics for an alloy base material.⁴

GROUP
IA

☐ Solids
☐ Liquids
☐ Gases
☐ Artificially Prepared

Atomic Number — 26
Symbol — Fe
Name — Hydrogen
Atomic Weight — 1.0079

7

1.2 Tantalum-Tungsten Alloys

Tantalum and tantalum alloys provide a combination of properties not found in many refractory metals. These include excellent fabricability, low ductile-to-brittle transition temperature, high melting point (Table 1.2.1), and a moderately high elastic modulus. Due to these unique features, tantalum base alloys have been among the most attractive materials for applications in the aerospace and nuclear industries. As a result, the high-temperature mechanical properties of these alloys were the subject of considerable interest from both a theoretical and technical viewpoint in the 1960s, which led to several investigations on creep and stress-rupture of pure tantalum and tantalum alloys during that decade.⁴

Material	Density (g/cm³)	Melting Point (°C)
Ta ⁴	16.6	2996
Ta-10%W ⁵	16.8	3035
T-111 ⁸	16.72	2982

Table 1.2.1. Physical properties of tantalum, Ta-10%W and T-111.

Many studies have addressed the macroscopic mechanical response of unalloyed tantalum and tantalum-tungsten alloys over a wide range of deformation conditions.⁶ In general, pure tantalum exhibits mechanical behavior typical of bcc metals with flow stress being extremely sensitive to strain-rate and temperature. The addition of tungsten as an alloying element causes significant changes in mechanical behavior with an increase in yield stress, an increase in work hardening, and a decrease in strain rate and temperature sensitivity.⁷

Researchers have observed that the mechanical behavior of tantalum-tungsten alloys resembles that of fcc metals.⁷

T-111 is basically a single-phase solid-solution tantalum-tungsten alloy containing nominally 8-percent tungsten and 2-percent hafnium. The 2-percent hafnium level was originally selected on the basis of ductility considerations necessary for aerospace and space powers systems applications.⁸ The amount of interstitials such as oxygen, carbon, nitrogen, and hydrogen significantly affects the strength and ductility of the alloy.⁸ Thus, limits are placed on these elements as shown in Table 1.2.2.

Material	C	N	O	H	Fe	Ni	Mo	W	Hf	Ta
Tantalum	<300	<150	<300	<100	<200	<200	-	<300	-	Bal.
Ta-10%W	<50	<50	<100	<10	<100	<100	<300	8.5 -11%	-	Bal.
T-111	<50	<50	<100	<10	<50	<50	<200	7.0 - 9.0%	1.8 -2.4%	Bal.

Table 1.2.2. Specification for the Composition of Tantalum, Ta-10%W and T-111 (ppm wt. %)⁵.

Most tantalum alloys readily oxidize at elevated temperatures and it is recommended that T-111 should not be heated above 316°C in air.⁸ Above this temperature, the alloy absorbs interstitials from the air and therefore should be heated in a good vacuum ($< 10^{-6}$ torr), or in a protective atmosphere such as argon or helium.⁸ An oxidation study (Sections 4.4 and 5.1) was conducted on T-111 and Ta-10%W to ensure that any potential deleterious oxidation effects from heating in air did not occur during the experimental phases of this research.

1.3 Mechanical Properties of T-111 and Ta-10%W

All high-temperature refractory alloys are generally designed to be used in the stress-relieved condition rather than the fully recrystallized condition, in order to take advantage of the higher strength present in the stress-relieved condition.²²

The recrystallization temperature depends on the amount of cold- or warm-work and also on the exposure time. The temperature to fully recrystallize 75% cold-worked alloy T-111 has been reported to be 1650°C for a 1 hour anneal.²²

For comparison purposes, the mechanical properties of recrystallized T-111 and Ta-10%W at 25°C are provided in Table 1.3.1.

Property	T-111	Ta-10%W
UTS (MPa)	772-780 ⁵	549 - 620 ⁵
Yield (MPa)	662-694 ⁵	462 - 503 ⁵
Elongation (%)	17.9-21.8 ⁵	16 ⁵
Modulus (GPa)	178 ²²	163-207 ⁵

Table 1.3.1. Mechanical Properties of Recrystallized T-111 and Ta10%W at 25°C.

Noticeably, none of the properties included in Table 1.3.1 for T-111 and Ta-10%W are associated with properties resulting from creep/stress rupture. The characterization of the creep/stress rupture behavior of plutonium-238 fuel encapsulation materials is critical to ensure that RTG design requirements are met. Data for the creep testing at low and elevated temperatures is not included due to the considerable variability in the literature regarding the behavior of these alloys. This is primarily due to differences in material chemistry and

microstructure, and testing conditions such as temperature, applied stress and environment (inert atmosphere, vacuum, etc.).

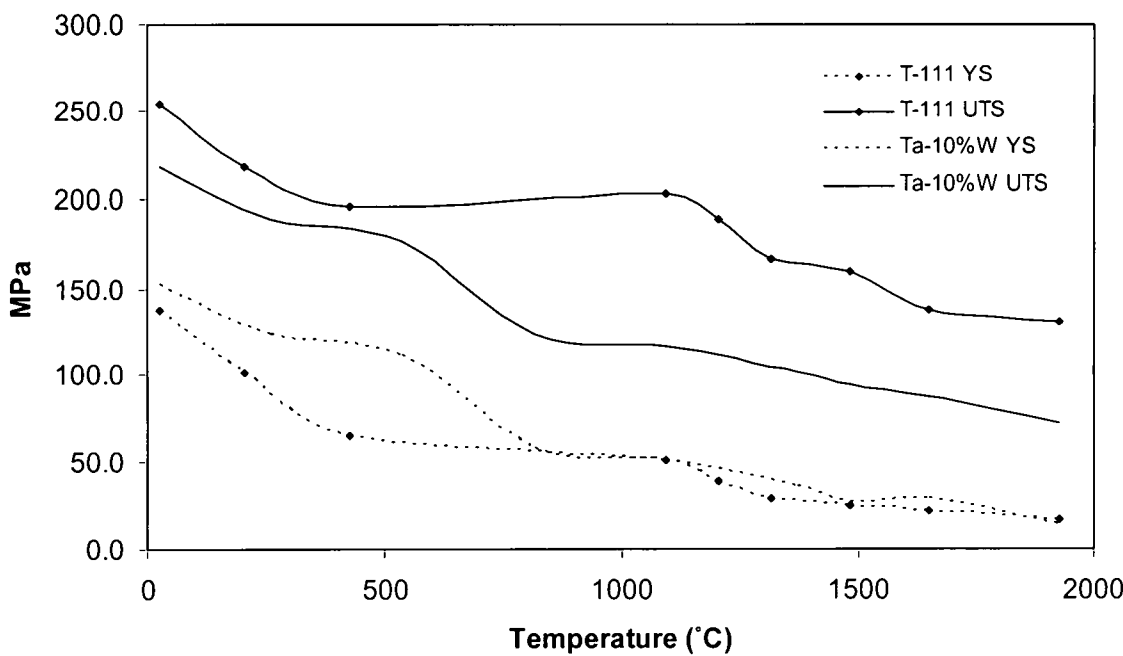


Figure 1.3.1. Effect of Test Temperature on Tensile Properties of Recrystallized Ta-10%W and T-111 Sheet Material.⁵

The ultimate tensile strength for Ta-10%W and T-111 has been measured by several researchers. Figures 1.3.1 and 1.3.2 summarizes the ultimate tensile (UTS) and yield strength (YS), and elongation data obtained from tensile tests on recrystallized specimens.⁵ In addition to these properties, tantalum and its alloys exhibit a pronounced temperature and strain rate sensitivity. Zinkle²² noted for T-111 that dynamic strain aging occurs at temperatures between approximately 500-1000°C for typical tensile strain rates of $\sim 10^{-3} \text{ s}^{-1}$. Dynamic strain aging (DSA) is manifested by a negative strain rate sensitivity, which means the UTS and other strength properties decrease with increasing strain rate.

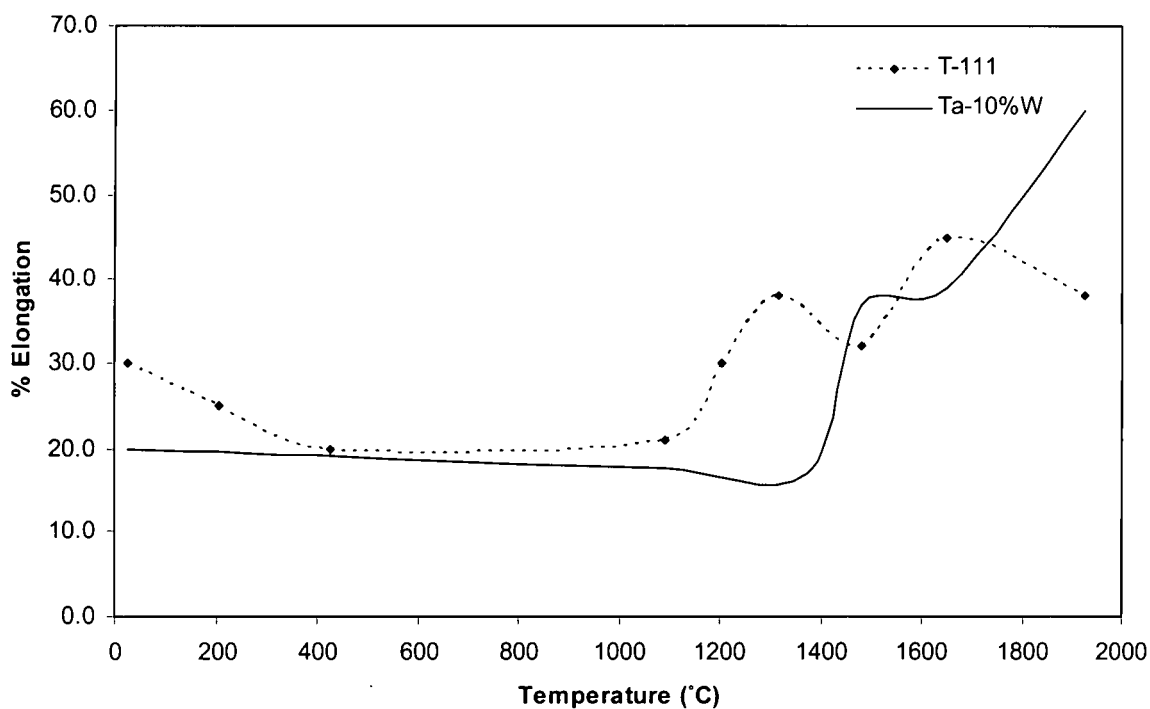


Figure 1.3.2. Effect of Test Temperature on the Percent Elongation of Recrystallized Ta-10%W and T-111 Sheet Material.⁵

1.4 Creep of Materials

Creep is the term used to describe the tendency of a material to deform permanently to relieve stresses. Material deformation occurs as a result of long term exposure to levels of stress that are below the yield or ultimate strength of the material. Creep behavior is more pronounced in materials as they are subjected to thermal environments ranging from ambient up to their melting point. The temperatures at which creep tests are conducted are measured relative to the melting point (homologous temperature, T_m) of the material being tested.

Creep is not a failure mode, but is considered a damage mechanism. Depending on the material being tested the deformation mechanism will vary depending on the stress level and exposure temperature. If the magnitude of the applied stress, relative to the material's yield stress for a given temperature, is sufficiently high when coupled with a protracted duration then creep deformation may result in failure (stress rupture). Rather than failing suddenly by fracture, the material permanently strains over a longer period of time until it finally fails. This makes creep deformation a "time-dependent" deformation of the material.

The rate of creep deformation is a function of the material properties, exposure time, exposure temperature and the applied load (stress). The dependence of steady state creep rate on stress is typically described by one of the following phenomenological relations⁹:

1. The power law - $\dot{\epsilon} \propto A\sigma^n$
2. The exponential Law - $\dot{\epsilon} \propto Ae^{B\sigma}$
3. The Sinh law - $\dot{\epsilon} \propto A[\text{Sinh}(\alpha\sigma)]^n$

Where n is the stress function and A is a dimensionless constant which has values of the order of unity to as large as 10^{16} and is dependent on thermodynamic variables.¹⁰ There is ample evidence that for many materials the value of n may change from 3 to 7 at higher stresses¹⁰ (dislocation creep) and to about 1 at lower stresses (Nabarro-Herring or Coble creep).¹¹

Initially during creep testing, the strain rate slows with increasing strain. This is known as primary creep, which is graphically shown in Figure 1.4.1. Secondary or steady-state creep is when the strain rate eventually reaches a minimum and becomes near-constant. This regime is considered to be the most well understood of the three creep regimes. The "creep strain rate" commonly discussed in the literature is typically the rate in this secondary stage. The stress dependence of this rate depends on the creep mechanism. As shown in Figure 1.4.1, during tertiary creep, the strain-rate exponentially increases with strain.

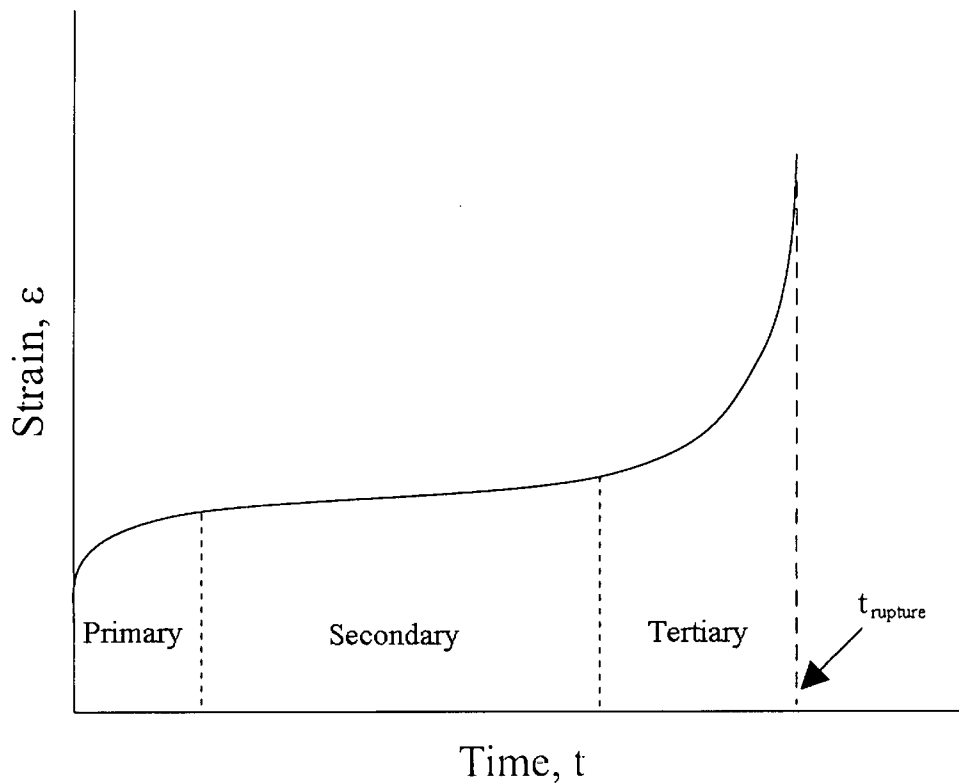


Figure 1.4.1. Generic creep curve showing the three stages of creep.

In this present research on the two discussed tantalum alloys, the creep mechanism can be best described as dislocation creep; due to the relatively low exposure temperature and high applied stress. At these conditions creep is controlled by the movement of dislocations.¹⁰

When a stress is applied to a material, plastic deformation occurs due to the movement of dislocations in the slip plane. Materials contain a variety of defects, for example; solute atoms, which act as obstacles to dislocation motion. Creep arises from this because of the phenomenon of dislocation glide. At lower temperatures dislocations within the lattice can kink or jog upon encountering

obstacles to their motion and move to an adjacent slip plane, thus allowing further deformation to occur.

The focus of this research is on the low-temperature creep/stress rupture behavior of both T-111 and Ta-10%W that has been exposed to low-levels of neutron radiation. Since the early 1960s, there have been copious amounts of creep data generated regarding refractory alloys,⁶ which includes both T-111 and Ta-10%W at elevated temperatures. However, there is very little literature regarding the low-temperature creep behavior of these alloys and nothing in the literature regarding of the low-temperature creep/stress rupture behavior of T-111 or Ta-10%W that has been exposed to low-levels of neutron radiation.

1.5 Low-Temperature Creep

At temperatures less than $0.4 T_m$, creep is governed by non-diffusion controlled mechanisms.¹¹ According to Garofalo¹² there are three thermally activated mechanisms that possibly control low-temperature creep in metals and alloys:

1. Cross-slip
2. Intersection of dislocations
3. Lattice friction arising from Peierls forces

The low-temperature creep/stress rupture behavior of both T-111 and Ta-10%W is affected by a combination of all three of these mechanisms. Therefore each will be address separately.

1.5.1 Cross Slip

Cross slip is restricted to screw dislocations.¹³ To a screw dislocation, all directions around its axis look the same, and it can glide on any plane as long as it moves parallel to its original orientation.¹³ Figure 1.5.1 depicts the cross slip of a screw dislocation from one slip plane to another.

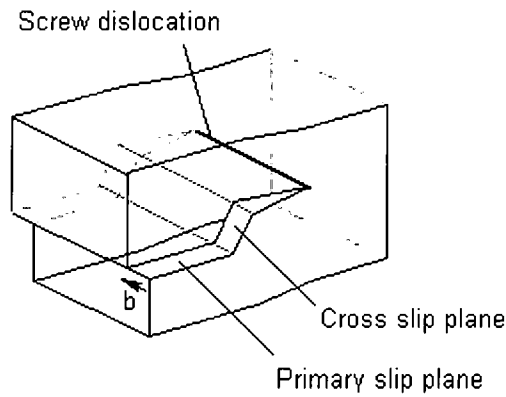


Figure 1.5.1. Cross Slip of a Screw Dislocation.

Therefore, a screw dislocation can cross slip from one plane to another only if both planes contain a common slip direction.¹³ A Burgers vector is a vector that denotes the amount and direction of atomic displacement which occurs within a materials lattice when a dislocation moves.¹³ The Burgers vector for screw dislocations are parallel to the dislocation line and for anisotropic materials, screw dislocations prefer certain crystallographic planes in which its energy is lowest.¹² The bcc crystal structure has 48 possible slip systems including $\langle 111 \rangle \{110\}$, $\langle 111 \rangle \{112\}$, and $\langle 111 \rangle \{123\}$ along which crystallographic slip can occur.¹³ Some of these slip systems in the bcc crystal structure are shown in Figure 1.5.2.

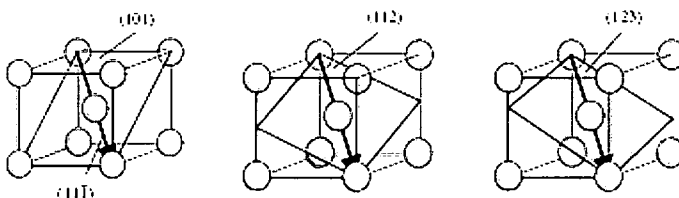


Figure 1.5.2. Slip systems in bcc materials.

When dislocations gliding in a primary slip plane are arrested by a sessile dislocation (a dislocation with a Burgers vector not in the direction of slip thus is immobile under applied force) or other obstacles, their screw component can cross-slip into an intersecting plane which has a common slip direction with the primary slip plane.¹²

1.5.2 Intersection of Dislocations

Another mechanism of low-temperature creep occurs when dislocations moving in the slip plane cut through other dislocations intersecting the active slip plane. This mechanism is called intersection of dislocations.¹³ The intersection of two dislocations results in a small step or jog in the dislocation line, which restricts the motion of the dislocations¹³ and contributes to the reduction in the rate of secondary creep.

1.5.3 Lattice Friction

In bcc crystals, for screw dislocations to glide from one plane to another they must overcome energy barriers, which requires high stress levels at low temperatures.¹⁴ The resistance opposed by the lattice to this motion is called lattice friction, or Peierls stress, which is a function of the symmetry of the bcc lattice and is not due to the nature of the chemical bonding of the atoms in the lattice.¹⁴

Therefore, the mobility of screw dislocations is comparatively very low but strongly temperature dependent.¹⁴ Thus, the activation energy for overcoming lattice friction is entirely a thermal process, and above $0.15 T_m$ the mechanical behavior of bcc and fcc materials becomes very similar.¹⁴

As strain increases during the transient phase of low-temperature creep there is experimental evidence shows that dislocation density also increases, thus indicating generation or multiplication of dislocations. This increase in dislocation density is observed at dislocation tangles and subboundaries with a relative decrease in dislocation density within the subgrains. However, this relative decrease within the subgrains does not compensate for the increased density at tangles and subboundaries. This indicates that multiplication of dislocations may occur by a process such a double cross-slip and that immobilization occurs at tangles or subboundaries.¹²

1.5.4 Dislocation-Point Defect Interaction

In addition to the three thermally activated mechanisms that control low temperature creep, discussed in the Sections 1.5.1 though 1.5.3, it is necessary to also discuss the interaction dislocations with point defects within a material's lattice. As will be discussed in greater detail in Section 1.6, the effect of the collision of high-energy atomic particles, such as neutrons, will create interstitials and vacancies in metals and alloys.¹³ Dislocations and irradiation produced point defects will interact elastically¹³ and exert large strain fields in the lattice of

irradiated metals, thus pinning dislocations. The effects of the lattice strains produced by neutron irradiation damage is dependent on environmental conditions such as irradiation temperature and mechanical testing parameters that include testing temperature, and stress and strain rates. The effects of neutron radiation on alloys investigated in this research will be discussed in greater detail in Sections 2.2 and 2.3.

1.5.5 Review

As discussed, the primary mechanisms that control low-temperature creep in metals and alloys are:

1. Cross-slip
2. Intersection of dislocations
3. Lattice friction arising from Peierls forces

Each of these mechanisms involves the interaction of dislocations with other dislocations, intrinsic forces within the material's lattice or with other obstacles. In essence, low temperature-creep behavior of metals is a function of all three of these mechanisms. The focus of this research is to determine the influence of low levels of neutron irradiation on the mechanical properties of two specific tantalum alloys by determining the interaction of the material's dislocations with the lattice defects produced by radiation equivalent to that produced by a RTG during a mission lifetime. The following sections will discuss the overall effects of neutron radiation on materials.

1.6 Radiation Effects on Materials

Ionizing radiation is either particle radiation or electromagnetic radiation in which an individual particle/photon carries enough energy to ionize an atom or molecule by completely removing an electron from its orbit. Figure 1.6.1 schematically shows the interaction of ionizing radiation (atomic ions- α , electrons- β , photons- γ , and neutrons- n). The ionizing radiation of interest during this research is neutron radiation because this is the type of ionizing radiation emitted by the $^{238}\text{PuO}_2$ encapsulated fuel in RTGs. Neutrons are particularly efficient at causing the following general types of radiation effects on materials:

1. Atomic Displacement – Displacement of atoms from their normal lattice position which may create vacancies and/or interstitials, or cause an interchange of dissimilar atoms in the lattice structure.
2. Impurity Production – Transmutation of nuclei into other nuclei, which may be radioactive, through neutron capture (activation).

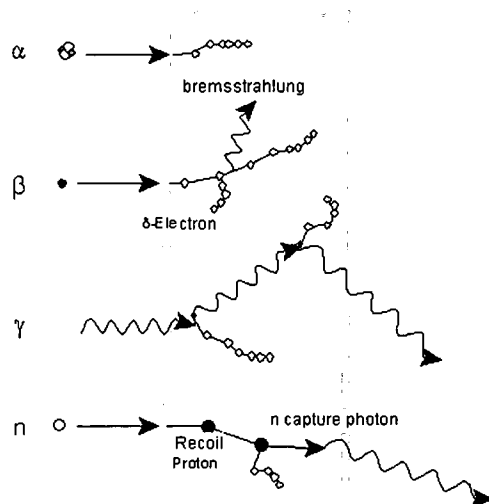


Figure 1.6.1. The interaction of ionizing radiation with materials.

1.6.1 Atomic Displacement

A major source of neutron irradiation damage in metals is the displacement of atoms from their normal lattice sites. Specific to neutrons, atomic displacement occurs when a neutron elastically collides with an atom and ejects it from its normal lattice position.¹⁵ The ejected atom is known as a primary knock-on, which, in turn, may cause a cascade of atomic displacements before eventually coming to rest. Figure 1.6.2 schematically shows how a displaced atom can become an interstitial and how the position the atom formerly occupied becomes a vacancy. Together the interstitial and vacancy are referred to as a Frenkel pair. Additionally, some displaced atoms can lead to secondary displacements. For example, the displaced atom may collide with and replace another atom within the structure of the material.

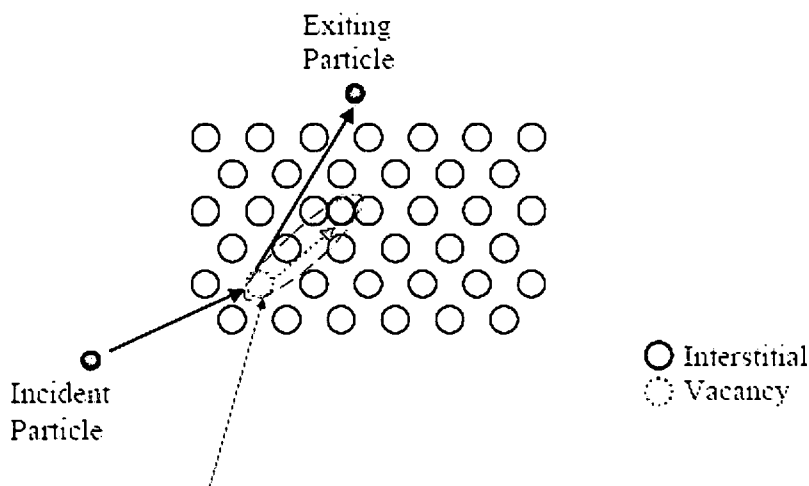


Figure 1.6.2. Displacement damage created by an incident neutron on a material lattice.

This displacement of atoms by irradiation is described in terms of displacements per atom (dpa), which is a measure of the average number of times an atom is displaced from its lattice position.¹⁵ The number of dpa associated with a particular irradiation depends on the amount of energy deposited in the material by the neutrons.

1.6.2 Impurity Production

In addition to displacement damage, a neutron can be absorbed by an atom of the irradiated alloy, resulting in a transmutation reaction that produces a new metal atom and hydrogen and/or helium gas atoms within the alloy being irradiated. Indications are that small amounts of new metal atoms have little effect on properties.¹⁵

The s-process or slow-neutron-capture-process occurs at lower fluxes, on the order of 10^5 to 10^{11} (n/cm²-s). Although the irradiation of the materials studied in this research occurred at slightly higher flux, it is still considered an s-process. Under these conditions the rate of neutron capture by atomic nuclei is slow relative to the rate of radioactive beta-decay. This process produces stable isotopes. The s-process differs from the more rapid r-process and the proton-capture or p-process in terms of reaction pathways.

Figure 1.6.3 graphically shows, using dark arrows, the reaction path of the s-process in the region of the hafnium, tantalum and tungsten isotopes. The stable hafnium, tantalum and tungsten nuclei capture a neutron, thus producing ¹⁸¹Hf, ¹⁸²Ta and ¹⁸⁷W.

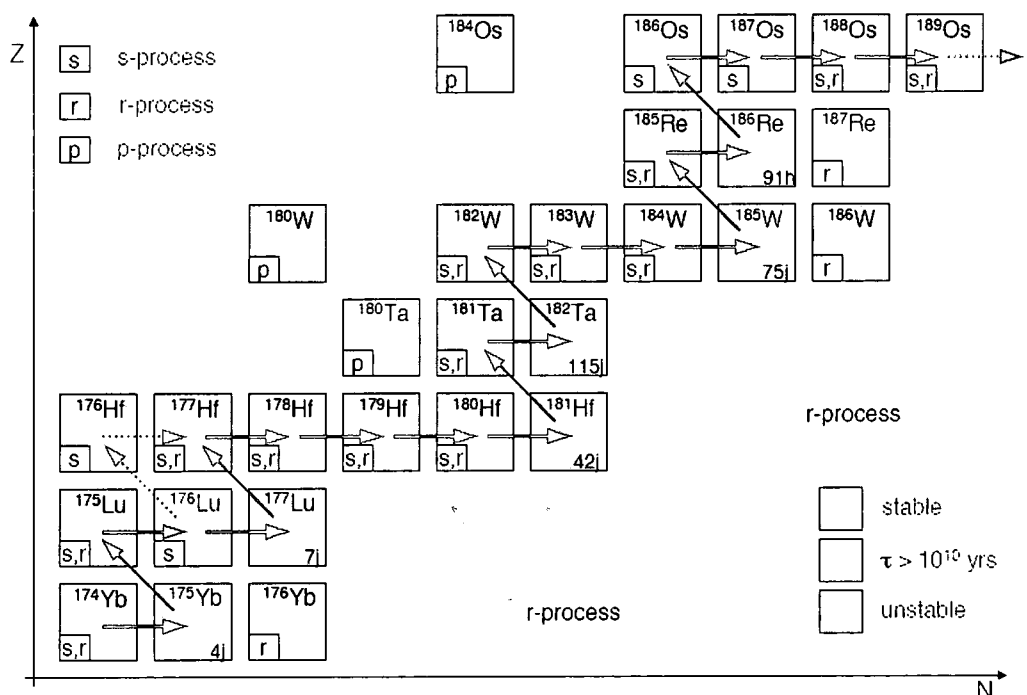


Figure 1.6.3. Reaction path of the s-process in the region of the Hf, Ta and W isotopes.

Table 1.6.1 shows the half-life, decay mode, decay energy and daughter nucleus of the created isotopes. Decay energy is the energy equivalent to the difference in atomic mass between the nuclide undergoing radioactive decay and its daughter nuclide, all in their nuclear ground states.

Irradiated Parent Nucleus	Parent Half -Life $T_{1/2}$	Decay Mode	Decay Energy (MeV)	Daughter Nucleus
$^{181}_{72}\text{Hf}$	42.39 days	β^- : 100 %	1.030	$^{181}_{73}\text{Ta}$
$^{182}_{73}\text{Ta}$	114.43 days	β^- : 100 %	1.814	$^{182}_{74}\text{W}$
$^{187}_{74}\text{W}$	23.9 hours	β^- : 100 %	1.311	$^{187}_{75}\text{Re}$

Table 1.6.1. Half-life, decay mode, decay energy and daughter nucleus of the created Hf, Ta and W isotopes.

1.7 Summary

The previous sections were intended to provide sufficient background regarding the primary focus of this research during the investigation of the effects of low level neutron radiation on the two primary tantalum alloys (Ta-10%W and T-111) used to encapsulate $^{238}\text{PuO}_2$ fuel in some radioisotope power system applications.

CHAPTER II

LITERATURE REVIEW

"I start where the last man left off." - Thomas A. Edison

2.1 Overview

Historically, the objectives of the majority of the research associated with studying the effects of irradiation on materials has been focused on the characterization of the damage process in structural materials during the operation of nuclear reactors.¹⁶

As a result, the prevailing assumptions regarding the effects of low fluence levels of neutron radiation that produces correspondingly low levels of irradiation damage (<0.001 dpa) on the tantalum alloys used in radioisotope powers systems are at most negligible.¹⁶ Other bcc refractory metals such as niobium and molybdenum have been widely investigated, however, studies on the low-level radiation response of tantalum is quite limited. Thus, there is little if any published data at the lower damage levels (<0.000001 dpa) that are associated with the $^{238}\text{PuO}_2$ fuel in RTGs. Dr. Steven Zinkle (Corporate Fellow and director of Oak Ridge National Laboratory's Materials Science and Technology Division) reinforced this observation during a visit and stated that only the effects of neutron irradiation on the physical and mechanical properties of Ta-10%W and

T-111 at fluence levels > 0.001 dpa are well characterized.¹⁶ Figure 2.1.1 is a graph provided by Dr. Zinkle that presents tensile elongation vs. displacement damage (dpa) of Ta-10%W after neutron irradiation at 70°C.¹⁶ It should be noted that no data is shown for displacement damage less than 0.001 dpa. The line labeled "Total Elongation" between 35% and 4% is extrapolated. But this is the principle area of interest regarding displacement damage associated with ^{238}Pu fueled RTGs, which is the thrust of this research. Although the effects of neutron irradiation on these materials require further investigation at the lower fluence level, Dr. Zinkle did state that minor effects on the ductility of these alloys should be observed.¹⁶

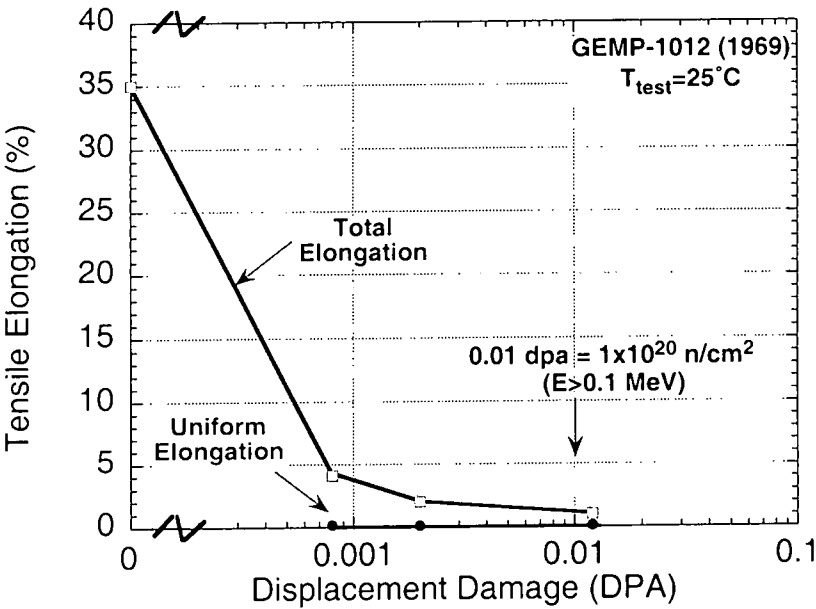


Figure 2.1.1. Tensile Elongations of Ta-10%W after Neutron Irradiation at 70°C.¹⁶

2.2 Effects of Neutron Irradiation on Metals

All metals have a crystalline microstructure whose atoms are arranged in a well-defined lattice where each atom has an equilibrium position. Ideally, there should be no imperfections in the atomic arrangement. However, imperfections exist due to the presence of impurities and alloying elements. Further irregularities can be introduced by plastic deformation, as any alteration in the regularity of the lattice will alter the properties of a material. Microstructural defects on the atomic level will lead to macrostructural defects.¹⁷

Neutron radiation tends to “destroy” crystal order which alters properties by producing several types of defects. The most important material damage types leading to failure are atomic displacement and gas production.¹⁷

Atomic displacements are the fundamental process of radiation damage in metals. They result from the transfer of kinetic energy as a charged particle passes through matter and elastically collides with an atom thus displacing it from its lattice position. As previously mentioned, vacancy-interstitial pairs (Frenkel defects) are formed when energetic particles collide with atoms, ejecting them from stable lattice sites. These displaced atoms finally lose their energy and occupy positions other than normal lattice sites, thus becoming interstitials.¹⁵ The presence of interstitials and vacancies makes it more difficult for dislocations to move through the lattice, usually increasing the strength and reducing the

ductility of a material.^{13,15} The production of Frenkel defects is the dominating cause for property changes in irradiated materials.¹⁷

Early studies on highly irradiated metals (>1.0 dpa) clearly demonstrated that irradiation at low temperatures (<100°C) produced pronounced hardening, which is typically accompanied by a severe decrease in uniform plastic elongation as measured in uniaxial tensile tests.¹⁸ This decrease in tensile ductility associated with low temperature neutron irradiation was the topic of numerous studies performed in the 1960s, and the phenomenon was commonly referred to as low temperature radiation embrittlement.¹⁸

These initial efforts in the 1950s and 1960s led to many studies regarding the effects of moderate to high levels of irradiation (0.001 - 10.0 dpa) on the creep behavior of metals and alloys. The results show that the effect of irradiation on the resistance to creep is complicated in character because it is a function of both temperature and strain rate. Strain-hardening, is an increase in mechanical strength due to plastic deformation. At low temperatures, dislocations do not anneal out of the material, but their density continues to increase as the material is strained.¹⁹ The interactions of the increasing density of dislocations results in a corresponding increase in strength and reduction in ductility. The strain-hardening effect of irradiation manifests itself at testing temperatures below 0.5 T_m .¹⁹

Strain-hardening is more pronounced in metals irradiated at low temperature due to increases in matrix hardness as the presence of radiation-induced defects that act as obstacles to dislocation motion increase.¹⁸ Depending on the level of irradiation, there can be a five-fold increase in the density of screw dislocations which is accompanied by a decrease in strain rate during creep.¹⁹

Overall, the existing mechanical properties database is very limited for irradiated tantalum alloys, especially at the fluence levels of interest to the present research. However, some qualitative trends for tantalum alloys may be inferred from the larger database on irradiated vanadium alloys.²³

2.3 Effects of Neutron Irradiation on Tantalum Alloys

Consideration of tantalum alloys for space nuclear power systems must include an understanding of possible changes in mechanical properties due to potential irradiation damage. To date, there are very few reports in the literature on the mechanical properties of irradiated tantalum and tantalum alloys.²² The minimum work that has been reported was performed at high fluence levels (>0.001 dpa), which is commensurate with the fluence levels associated with fission or fusion reactors. What can be extracted from the literature shows that results tend to follow trends seen in the behavior of other BCC alloys under irradiation.²² These high neutron fluence levels and the resulting lattice damage reported in the literature are often several orders of magnitude greater than the corresponding fluence levels and lattice damage associated with the $^{238}\text{PuO}_2$ fuel in RTGs.

Regardless of these “gaps” in knowledge, Ta-10%W and T-111 are the preferred tantalum alloys for space nuclear power applications due to their favorable physical and mechanical properties and compatibility with $^{238}\text{PuO}_2$ fuel.²⁰ However, potential issues exist that could limit their use such as:

- Unknown lower operating temperature limits due to radiation embrittlement;²¹
- Uncertainties in long-term thermal and neutron irradiation stability of the precipitates responsible for high creep strength;²¹
- Lack of recent industrial experience in fabricating tantalum alloys.⁴

In general, exposure of BCC alloys to neutron irradiation typically causes a significant increase in strength at low temperatures ($<0.3T_m$) with a corresponding reduction in elongation,²¹ which is generally pronounced even for doses as low as ~ 1 dpa.²² However, there are no known mechanical studies in the literature of irradiated T-111 at irradiation temperatures up to 650°C ($<0.3T_m$) for:

- Yield and ultimate strength;²²
- Stress rupture and creep;²² and
- Ductile to brittle transition temperature.²²

Additionally, there are very few studies on the mechanical properties of refractory alloys irradiated and tested at temperatures above $0.3T_m$. There are no known fracture toughness measurements on high temperature refractory alloys of molybdenum, tungsten and tantalum following neutron irradiation at any dose or temperature.²³ The Charpy V-notch impact database on irradiated high temperature refractory alloys is also virtually nonexistent.²³

What the literature shows is that significant radiation hardening has been observed in Ta-(8-10%)W alloys irradiated at 415°C and 640°C to a fluence of $1.9 \times 10^{26} \text{ n/m}^2$, whereas very little hardening occurred at an irradiation temperature of 800°C .²³ This neutron fluence level is commensurate with a

fluence level associated with a fission or fusion reactor and results in a neutron displacement damage of 2.5 dpa in Ta (10 dpa in steel).²³ Since the matrix hardening in Ta-(8-10%)W at 415°C and 640°C is well above the level which produces brittle behavior in vanadium alloys, it is likely that Ta alloys are embrittled at these irradiation conditions.²² What this means is that the effect of radiation damage effectively anneals out in tantalum-tungsten alloys at temperatures above 800°C ($\sim 0.3 T_m$).

The “gaps” in knowledge regarding the effects of low fluence levels of neutron radiation and the corresponding low levels of neutron displacement damage (< 0.001 dpa) in Ta-(8-10%)W alloys form the foundation of the focus of this thesis research.

2.4 Experimental Motivation

The fundamental motivation for deriving and proving a hypothesis that takes into account the effects of low levels of irradiation on the mechanical properties of materials used in Radioisotope Power Systems is the major deficiency of experimental data that covers the spectrum of materials, irradiation and thermal conditions associated with Radioisotope Power System designs.

It is clear that Radioisotope Power Systems components with design lifetimes of up to ~30 years cannot reach end-of-life fluence levels in laboratory experiments. This necessitates the expedited use of high neutron fluences in order to simulate a 30-year mission life under laboratory conditions.

Historically, design validation activities of structural materials for radioisotope power systems have included accelerated pressure burst testing of inert capsules.²⁴⁻²⁵ This is performed on pressurized capsules to extrapolate values for the expected end-of-life pressure that result from the production of helium from the decay of ^{238}Pu .²⁵⁻²⁶ However, this has limitations since there has always been significant variability in the qualification of pressure burst data as it is not fully predictive, and most importantly, it may not explicitly incorporate material aging or irradiation effects.²⁵ In essence, these tests do not simulate real world applications.

Tantalum alloys need significant research and development in areas such as fabrication and irradiation effects before being qualified for use in Space Nuclear Radioisotope Power Systems.²⁷

The application of short irradiation times using higher neutron flux testing reactors, such as the Ohio State Research Reactor (OSURR), can provide data that corresponds to the neutron fluence levels associated with the 30-year mission life of a RTG. However, the acute irradiation exposure from a fission reactor may not yield identical material responses as a chronic exposure from a 30-year exposure to $^{238}\text{PuO}_2$. However, for the purposes of this research the relative difference in the effects on the mechanical properties in Ta-10%W and T-11 due to acute versus chronic neutron radiation exposures is considered to be negligible.

CHAPTER III

RESEARCH OBJECTIVES

"A problem well stated is a problem half-solved." - Charles Kettering

The long term effects of neutron fluence levels commensurate with the 30-year mission life of a RTG on the mechanical properties of T-111 and Ta-10%W are not known. The $^{238}\text{PuO}_2$ fuel in a RTG produces significant amounts of alpha-particles and neutron displacement damage. Alpha-particles (helium ions) are produced by the radioactive decay of ^{238}Pu and result in increasing pressure within the encapsulation layer of an RTG as the unit ages. The potential material "damage" from the emitted neutrons from the $^{238}\text{PuO}_2$ fuel is a function of the proximity to the $^{238}\text{PuO}_2$ fuel to the encapsulation layer of T-111 or Ta-10%W. As previously discussed, the lack of fundamental understanding of the effect of "RTG levels" of neutron irradiation on the deformation and failure mechanisms in two tantalum alloys (T-111 and Ta-10%W) at irradiation temperatures below 350°C led to the initiation of this research. The objectives of this research are:

1. To characterize the low-temperature creep deformation and failure modes and to develop low-temperature creep/stress rupture data for irradiated Ta-10%W and T-111.

2. Neutron Irradiation - To elucidate the interaction of neutron irradiation damage and low-temperature creep/stress rupture mechanisms for T-111 and Ta-10%W, which are not thoroughly discussed in literature or studied in detail.
3. Irradiation Temperature - To determine the effects of the interaction of irradiation fluence and temperature on the mechanical properties of irradiated Ta-10%W and T-111.

Achievement of these objectives will provide a basic understanding of the strength mechanisms of two tantalum alloys (Ta-10%W and T-111) resulting from neutron radiation at temperatures below 350°C. This will enhance the level of understanding of potential irradiation hardening mechanisms in both Ta-10%W and T-111 alloys.

The results this research will enable more confident extrapolation of relevant mechanical-property trends of T-111 and Ta-10%W encapsulation materials for neutron irradiation doses and internal pressure levels which correspond to actual RTG service lifetimes. This should provide space power system designers with information and material options for future applications that will support ambitious long duration and higher power space related missions.

3.1 Thesis Statement

Changes in the response of the mechanical properties of tantalum alloys Ta-10%W and T-111 resulting from exposure to low-levels of neutron irradiation ($<10^{16}$ nvt) at temperatures less than 350°C can be predicted by analysis of the dislocation network of both materials.

CHAPTER IV

EXPERIMENTAL METHODS

*"Research is what I'm doing when I don't know what I'm doing."
- Wernher Von Braun*

4.1 Material Characterization

Conducting a characterization of the starting materials for this research is important to ensure that they have similar microstructural, chemical, and physical properties. All of the materials used in this research were in their fully recrystallized state in order to minimize any anomalous variability of the response of the mechanical properties to the effect of neutron irradiation.

The three main aspects of the characterization of both tantalum alloys (Ta-10%W and T-111) used in this research are: grain size, microhardness and determination of the recrystallization state. Additionally, these materials were purchased by the USDOE in the 1970's in support of space power systems applications and were certified by the manufacturer and the USDOE to meet specification. Therefore, a full chemical analysis was not conducted. Table 4.1.1 shows the chemical specification limits for tantalum, Ta-10%W and T-111.⁵

Material	C	N	O	H	Fe	Ni	Mo	W	Hf	Ta
Tantalum	<300	<150	<300	<100	<200	<200	-	<300	-	Bal.
Ta-10W	<50	<50	<100	<10	<100	<100	<300	8.5 - 11%	-	Bal.
T-111	<50	<50	<100	<10	<50	<50	<200	7.0 - 9.0%	1.8 - 2.4%	Bal.

Table 4.1.1. Specification for composition of Tantalum, Ta-10%W and T-111 (ppm wt. %).⁵

4.1.1 Grain Size

Grain size is a measure of the areas or volumes of grains in a polycrystalline material, usually expressed as an average when the individual sizes are fairly uniform. Grain size is reported in terms of number of grains per unit area or volume, average diameter, or as a grain-size number derived from area measurements.

A material's grain size is important because it has an affect on mechanical properties.. Grain size of the sample materials was determined in accordance with ASTM Standard E112²⁸ using a polished and etched sample and optical microscopy by means of Differential Interference Contrast (DIC) illumination. See Figures 4.1.1 and 4.1.2 for micrographs showing the grains structure of the Ta-10%W and T-111 starting materials.

The grain size for the Tantalum alloy samples used in support of this research are shown in Table 4.1.2.

Material	Grain Size ²⁸	Mean Intercept
Ta-10%W	ASTM 6	48 μm
T-111	ASTM 7	34 μm

Table 4.1.2. ASTM Grain Size of the Materials used in this Research.

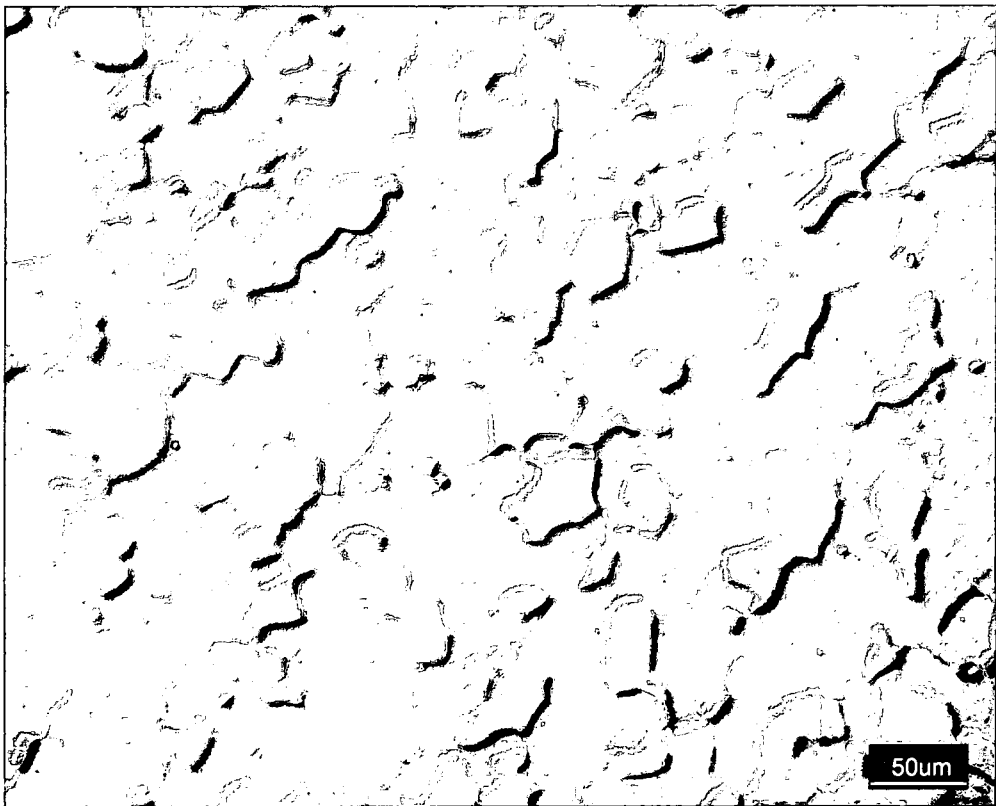


Figure 4.1.1. Photomicrograph of Representative Ta-10%W Sample Microstructure.

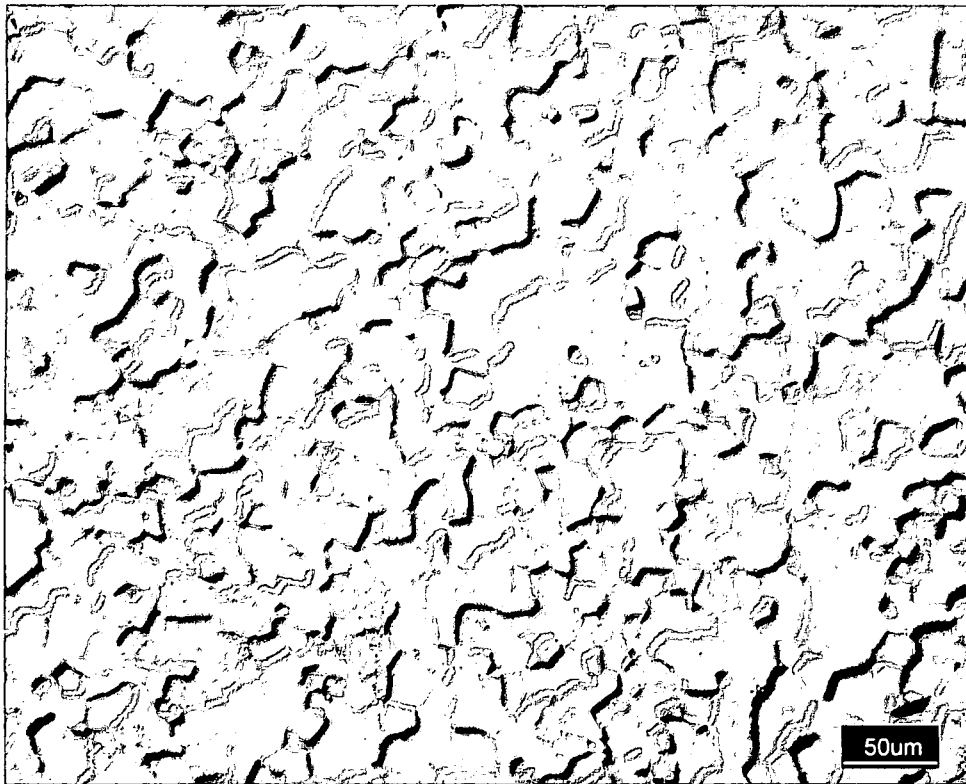


Figure 4.1.2. Photomicrograph of Representative T-111 Sample Microstructure.

4.1.2 Microhardness

Microhardness testing used an indentation method for measuring the hardness of a material on a microscopic scale. For this research, a precision diamond indenter was impressed into the material at a load of 500 g. The impression length, measured microscopically, and the test load was used to calculate a hardness value.

The indentations were made using a Vickers microhardness tester with a square-based pyramid indenter (Vickers hardness scale). The hardness impressions were precisely located with the microscope to perform tests on microscopic features. The hardness values obtained are useful as an indicator of materials

properties and expected service behavior. Conversions from microhardness values to tensile strength and other hardness scales (e.g. Rockwell) are available for many metals and alloys.

The Vickers hardness values for the tantalum alloy samples used in support of this research are shown in Table 4.1.3.

Material	Hardness (HV ₅₀₀)
Ta-10%W	241.7
T-111	278.9

Table 4.1.3. Vickers Hardness of the Materials used in this Research.

4.1.3 Recrystallization State

A fully recrystallized grain structure is largely strain-free and characterized by few, if any, dislocations within the grains and no concentrations of dislocations at grain boundaries. The mechanical properties of a recrystallized metal are those of the original, unstrained metal, except when changed by differences in grain size and preferred orientation. Recrystallization is also accompanied by a further decrease in stored energy, as measured calorimetrically, as well as by a complete elimination of residual stresses.

The recrystallization temperature of tantalum-tungsten alloys depends on the amount of cold- or warm-work and also on the working time. The temperature to

fully recrystallize 75% cold-worked T-111 has been reported to be 1650°C for a 1-hour anneal.²² A comparison of the hardness values for Ta-10%W and T-111 with Figures 4.1.3 and 4.1.4, respectively, confirms that both the Ta-10%W and T-111 materials used in this research are fully recrystallized.

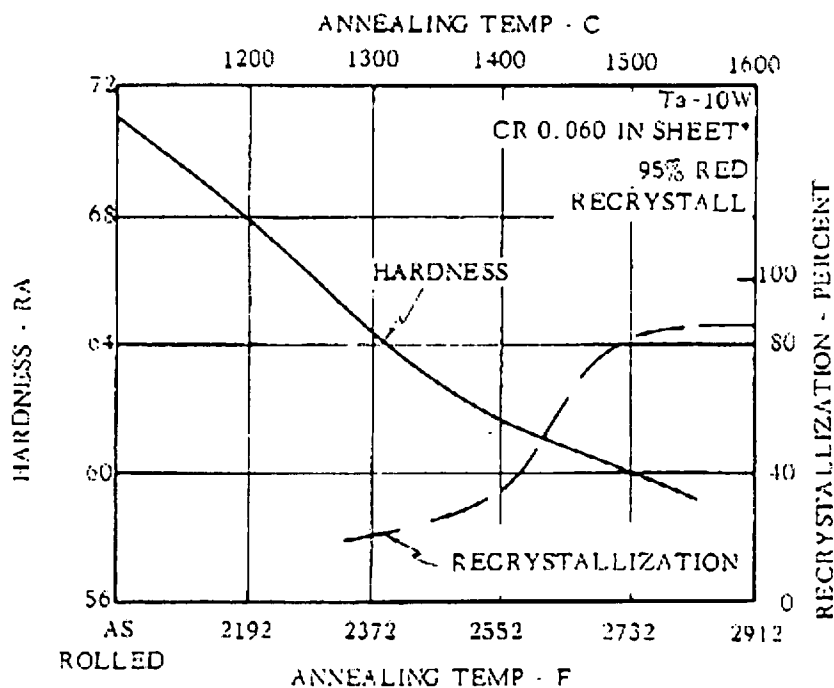


Figure 4.1.3. Effect of Annealing on Hardness of Ta-10%W.⁵

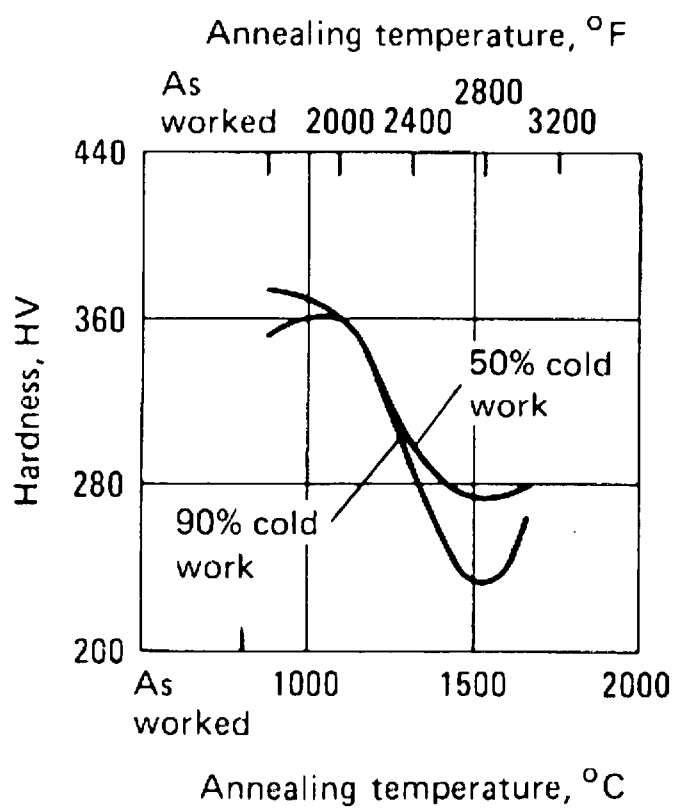


Figure 4.1.4. Effect of Annealing on Hardness of T-111.⁵

4.2 Test Specimen Preparation

All metallurgical and test specimens were obtained from 0.051 cm thick sheet stock via Wire Electrical Discharge Machining (WEDM). Figure 4.2.1 shows a representative section of the sheet material after completion of the WEDM process that resulted in the formation of mechanical test specimens and “cutouts” that were used for other non-destructive and destructive analyses. The length of the mechanical test specimens is parallel to the rolling direction of the starting sheet materials. The prepared mechanical test specimens are 7.62 cm long with a gauge length of 2.54 cm and a gauge width of 0.635 cm. The grip area is 1.575 cm long by 1.575 cm wide.

This type of specimen meets the requirements of ASTM Standard E8²⁹ and is in accordance with ASTM Standard E139³⁰. The specimen’s size has little effect on the material’s creep and rupture properties, provided that the material is not anisotropic or has been subjected to an environment to results in any appreciable surface corrosion.

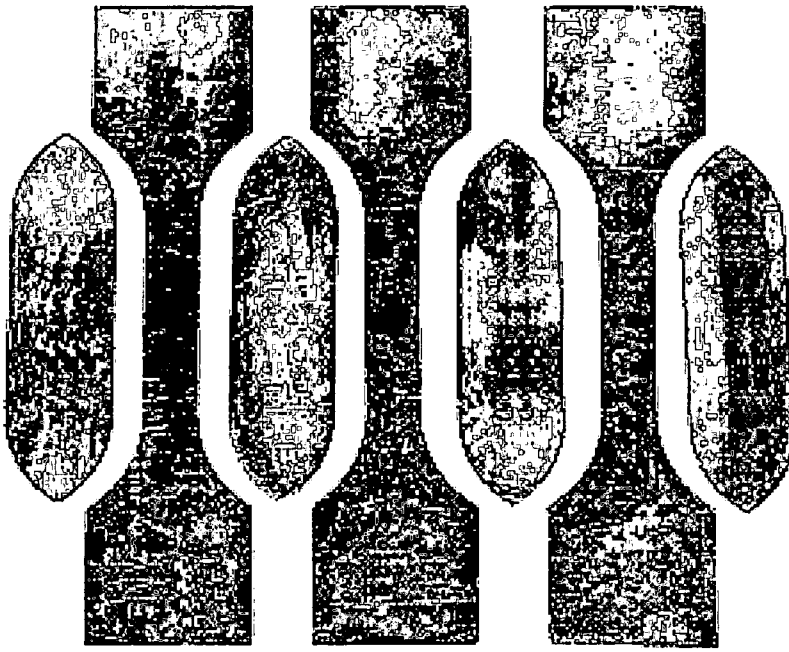


Figure 4.2.1. A section of sheet material after WEDM of mechanical test specimens and “cutouts.”

4.3 Test Specimen Cleaning

T-111 is sensitive to very small amounts of contamination by iron, copper and zinc.⁶ In order to ensure that residual brass from the WEDM does not introduce any anomalous variables into the testing results, all of the test specimens were thoroughly cleaned by immersing the samples in a commercial concentrated nitric acid solution (about 70% HNO₃) heated to 100°C.

The redox reaction between copper metal and concentrated nitric acid is complex, and depends on the concentration of the nitric acid and the temperature of the reaction mixture. Initially, with the concentrated nitric acid solution, the reaction is:



The mixture becomes green colored due to complexes of Cu²⁺ and NO₂ being formed, and brown fumes are evolved. When the acid becomes more dilute as the reaction proceeds, reduction to NO is likely. None of this affects the eventual outcome, which is a solution of copper(II) aquo ions and nitrate ions together with the aquo ions of [Cu(H₂O)₆]²⁺ and [Zn(H₂O)₆]²⁺. Once the residual brass was dissolved the samples were submersed in a hot distilled water bath (~ 90°C), thoroughly rinsed with distilled water, rinsed with isopropyl alcohol and then allowed to air dry.

In accordance with the cleaning procedure for tantalum alloy components used on RTG components provided by Oak Ridge National Laboratory (ORNL), the samples were then ultrasonically degreased for 10 minutes in EW-18100-01, Cole-Parmer® Micro-90® cleaning solution. This concentrated cleaning solution works at any concentration, rinses clean and safely replaces chromic acid, which is the preferred initial acid cleaning agent for tantalum and tantalum alloys. After degreasing, the samples were submersed in a distilled water bath, thoroughly rinsed with distilled water, rinsed with isopropyl alcohol and then allowed to air dry. The samples were then acid cleaned for three minutes in a volume mix of 20% HNO_3 , 10% HF , 70% distilled water; then submersed in a distilled water bath, thoroughly rinsed with distilled water, rinsed with isopropyl alcohol and then allowed to air dry. Once the samples were cleaned they were not wiped with paper or cloth or handled without the use of lint free gloves.

4.4 Oxidation Behavior Determination

Oxygen contamination of Ta-10%W and T-111 during irradiation and mechanical testing can yield misleading test data. The main concern with oxygen contamination in the Group V metals (vanadium, niobium and tantalum) is oxygen absorption. The absorption of a few atomic percent of oxygen (1 at. % = 892 ppm) in tantalum increases hardness, tensile strength, and modulus of elasticity, but decreases elongation and reduction in area.³¹

In bcc metals and alloys such as Ta-10%W and T-111 it has been observed that the average oxygen concentration in sheet specimens is directly proportional to time and oxygen pressure and inversely proportional to the specimen thickness with no observable surface reaction product.³¹

The oxygen absorption rate of metals at high temperatures ($> 0.3 T_m$) and oxygen partial pressures greater than 1 atm is limited by the diffusion rate of oxygen in the metals under investigation. However, at lower temperatures ($< 0.3 T_m$) the absorption of oxygen is surface-reaction limited.³²

Unfortunately, the highly specialized tensile and creep testing that is capable of testing refractory alloys at elevated temperatures ($> 0.3 T_m$) in a vacuum ($< 10^{-6}$ torr) are only available at a few locations including Oak Ridge National Laboratory and NASA Glenn Research Center. Additionally, the technical obstacles associated with irradiating specimens in a vacuum in the Ohio State

Research Reactor (OSURR) were too complex to be resolved within the timeframe of this research. Therefore, the focus of this research was bound by oxidation threshold temperatures of the two selected tantalum alloys.

4.4.1 Experimental Procedure

The objective of this experiment is to assess the effects of low temperature ($< 0.3 T_m$) oxidation of Ta-10%W and T-111 in air and minimal oxygen pressure environments on mechanical properties of these alloys.

To determine the oxidation behavior of the Ta-10%W and T-111 specimens used in this research, as outlined in Section 4.2, test specimens were obtained from 0.051 cm thick sheet stock via Wire Electrical Discharge Machining (WEDM). Figure 4.2.1 shows a representative section of the sheet material after completion of the WEDM process that resulted in the formation of mechanical test specimens and "cutouts." For the purposes of the oxidation experiment, multiple "cutouts" were used with separate cutouts being employed for different temperature runs.

Oxygen concentration was determined by measuring weight change. The test samples were weighed and heated in a furnace in atmospheric laboratory air at 300°C and 400°C. At periodic intervals the samples were removed from the furnace, weighed and then reinserted into the furnace.

Additionally, in order to validate that the mechanical properties of the specimens used in this research are unaffected by the atmosphere associated with irradiating specimens in the Ohio State Research Reactor (OSURR), a T-111 specimen was heated to 350°C for four hours in an inert atmosphere that contained ~1000 ppm O₂. The specimen was then creep tested at 25°C with a load of 620 MPa so that the results could be straightforwardly compared to those of the experimental design matrix outlined in section 4.7.2.

4.5 Test Specimen Irradiation

4.5.1 Determination of Irradiation Parameters

The 238-Plutonium isotope has a spontaneous fission rate of 1.1×10^3 fission/s-g and a very high heat output of 0.567 W/g. Also, it has very high alpha activity (283 times higher than 239-Plutonium) and a specific activity of 17.5 Ci/g, which makes it a much higher source of neutron emission from the alpha→n reaction.

The Department of Energy specification for 238-Plutonium Dioxide Fuel Pellets³³ allows a maximum neutron emission rate of 6000 neutrons/s-g of 238-Plutonium. A hypothetical RTG design that contains 2500g of 238-Plutonium will have a total neutron emission rate of 1.5×10^7 neutrons/s. Extrapolated to the expected 30-year lifespan of a RTG, the total neutron emission is approximately 1.5×10^{16} neutrons. Assuming the material is 1.0 cm from the fuel surface the total neutron fluence is approximately 1.2×10^{15} neutrons/cm² (nvt). During this research it was determined that a four-hour exposure in the OSURR produced a neutron fluence of approximately 1.2×10^{15} nvt.

Ta-10%W and T-111 specimens were irradiated at two temperatures, 25°C and 350°C, to a neutron fluence of 1.2×10^{15} nvt. Exposure to neutrons causes radiation damage in the target material that is dominated by displacements within the atomic structure and is described quantitatively by the number of displacements per atoms (dpa) over a certain period of time. The level of dpa depends on the level of the particle flux as well as on the flux spectrum since the

damage energy cross section is energy dependent. Based on available data by Broeders and Konobeyev³⁴ the estimated damage imparted to the irradiated Ta-10%W and T-111 specimens are in the low 10^{-7} dpa range.

4.5.2 Irradiation Facility

The test samples were irradiated at The Ohio State Nuclear Test Laboratory using the OSURR. The OSURR is a low-enriched uranium (LEU) fuel (19.5% enriched U_3Si_2) reactor, which has a licensed operating power of 500 kW and a thermal neutron flux of approximately 1.5×10^{13} neutrons/(cm^2 -sec). Figure 4.5.1 shows the OSURR in operation at full power. The glow in and around the reactor is Cherenkov radiation, which is the electromagnetic radiation emitted when a charged particle passes through the water at a speed greater than the speed of light in water.

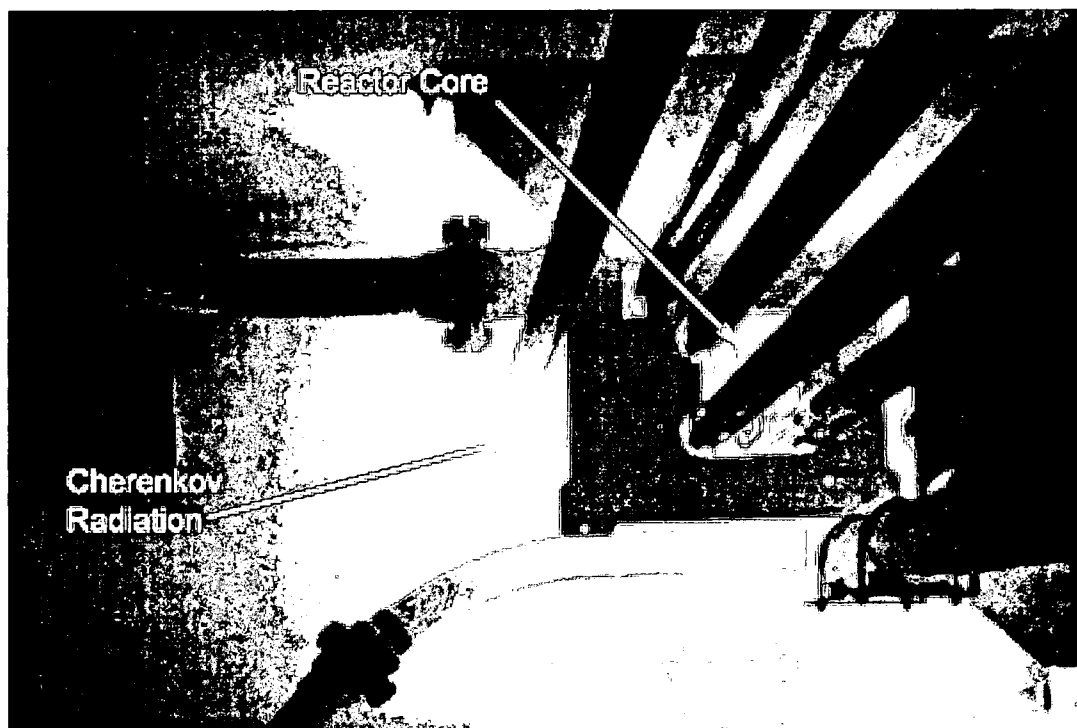


Figure 4.5.1. The OSURR at full power.

The OSURR experimental facilities include:

- 1.3" Central Irradiation Facility (CIF)
- Two 6" beam ports
- 2" rabbit tube
- 3.5" Auxiliary Irradiation Column (AIC)

For the purposes of this research, irradiation occurred in the 3.5" Auxiliary Irradiation Column (AIC) of the Ohio State Research Reactor (OSURR), shown in Figure 4.5.2, in an inert thermal environment that replicates the operating environment within a RTG. Samples irradiated for 4 hours in the AIC were exposed to a neutron fluence of 1.2×10^{15} nvt, which is roughly equivalent to the exposure materials experience during the 30-year lifespan within a $^{238}\text{PuO}_2$ fueled RTG. Fluence (or integrated flux) is the product (or integral) of particle or radiation flux and time, expressed in units of particles (neutrons) or energy per square centimeter.

4.5.3 Test Specimen Irradiation

In accordance with the Design of Experiments in Sections 4.6.2 and 4.7.2 the Ta-10%W and T-111 mechanical test specimens and cutouts, prepared per Section 4.2, were separated into four groups for the experimental runs. Table 4.5.1 shows the grouping of the experimental runs.

Group	Irradiation Level (nvt)	Irradiation Temperature (°C)
1	0	25
2	0	350
3	1.2×10^{15}	25
4	1.2×10^{15}	350

Table 4.5.1. Grouping of the experimental runs for the OSURR.

Since the specimens and cutouts in Groups 2 through 4 would be exposed to the reactor environment, it was considered prudent to place all the samples of each group together and wrap them with tantalum foil secured by tantalum wire. The intent was to mitigate and/or minimize any potential environmental effects associated with the inert atmosphere in the 3.5" Auxiliary Irradiation Column (AIC). The samples of each group were randomly stacked, alternating each layer between Ta-10%W and T-111. All individual and tantalum wrapped specimens were handled with lint free cloths and gloved hands to prevent contamination from human body oils and other potential laboratory contaminants. To minimize moisture and oxygen contamination, the tantalum foil wrapped groups specimens were then stored in a portable storage container that was evacuated and backfilled 5 times each with argon gas.

To heat the specimens within in the reactor's AIC to the appropriate test temperature a Watlow full cylindrical ceramic fiber heater (shown in Figure 4.5.2B) was employed with a Cole-Palmer Digi-Sense advanced temperature controller and an Omega four channel data logger. The ceramic fiber heater, has an iron-chrome-aluminum heating element and ceramic fiber insulation made of an alumina-silica composition, held together by an inorganic binder. The ceramic fiber heater, prior to experimental use, was baked-out at 900°C for 8-hours to minimize the potential for contamination of the tantalum wrapped specimens.

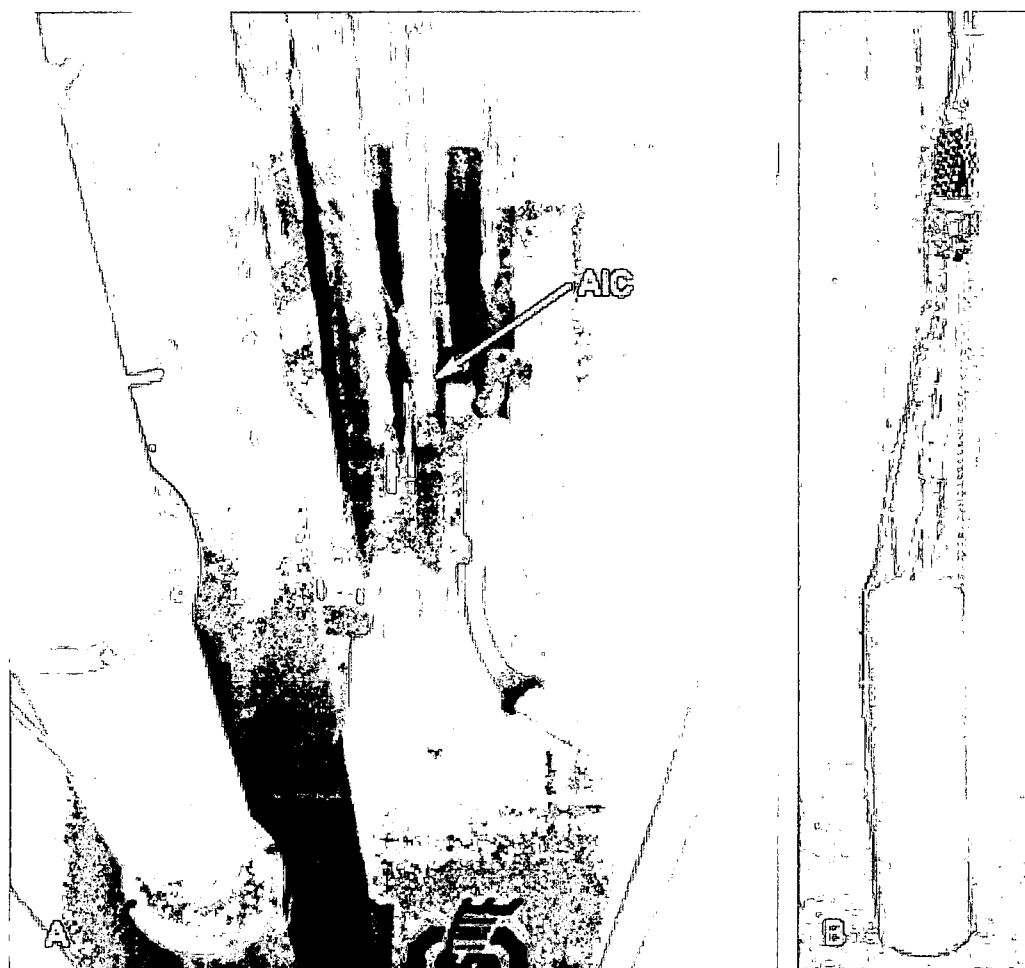


Figure 4.5.2. A) OSURR at full power with AIC shown in foreground; B) Watlow ceramic heater with thermocouples and electric cabling attached.

The cylindrical ceramic fiber heater used to irradiate the test specimens was wrapped with 0.102 cm thick cadmium sheet material to suppress thermal flux. Cadmium has a large absorption cross-section for neutrons below 0.4 eV and drops off to a negligible level above this energy. Thus, cadmium shielding effectively removes "thermal" neutrons below the "cadmium cutoff energy" of 0.4 eV and provides away to differentiate the thermal and epithermal neutrons. Figure 5.3.1 in the Results and Discussion chapter of this research shows the suppression of the thermal (Maxwellian) flux component quite clearly. Approximately, 95% of the flux has energy above the cadmium cutoff energy of 0.4 eV. Therefore, the majority of the neutron flux used to irradiate the test specimens is mostly epithermal flux.

There were a total of three reactor runs; one with the reactor at zero power (Group 2) and two at full power (Groups 3 and 4). For each reactor run the appropriate group of samples were loaded into the ceramic fiber heater and lowered into the AIC. The AIC was then sealed with a 24 inch long Teflon plug that provided a feed-through for the umbilical cable, which is comprised of two Type K high-temperature monitoring thermocouples, one Type K high-temperature control thermocouple, the ceramic fiber heater electrical cable, and the argon purge and atmospheric monitoring tubing.

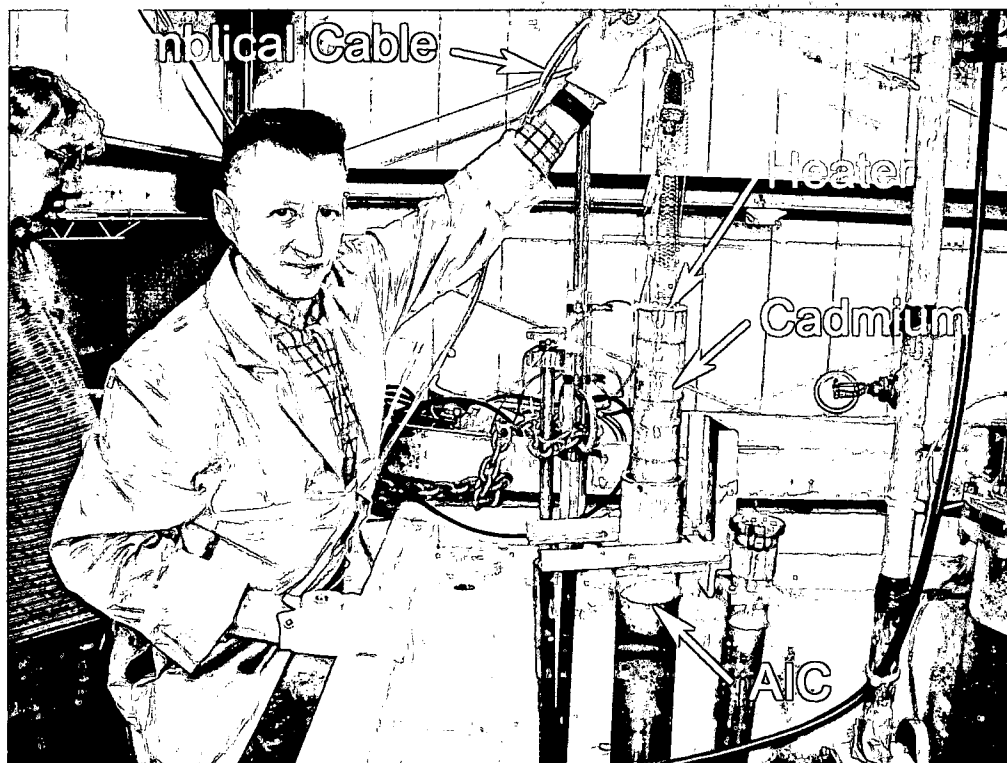


Figure 4.5.3. The PI lowering the cadmium wrapped experiment package into the AIC at the OSURR.

Before powering up the ceramic fiber heater and the reactor, the AIC was purged with commercially pure argon gas. The oxygen levels were continuously monitored using a MSA Passport PID II gas monitor. Once an oxygen level of <1000 ppm O_2 was achieved the ceramic fiber heater was powered up to the appropriate test temperature. After the appropriate test temperature for the specimens located in the ceramic fiber heater was achieved and stabilized, the sequence to bring the reactor online was initiated. At this stage the Passport O_2 monitor was turned off due to concerns of contaminating the monitor with radiogenic argon, which was activated in the AIC by thermal neutrons produced while the reactor was in operation. Although the O_2 levels were not actively

monitored, the AIC was continuously purged with argon at approximately 1 liter/min during operation of the reactor.

The reactor was operated at a full power level of 450 kW, which yielded a neutron flux of 8.23×10^{10} nv. The experiments were run at full power for duration of 4-hours each, which produced a total fluence of approximately 1.2×10^{15} nvt (8.23×10^{10} nv multiplied by 14400 s) for each run. As discussed previously, this neutron fluence level is equivalent to the cumulative fluence associated with the 30-year mission life of a RTG

4.5.4 Gamma Spectrometry

Gamma (γ) spectroscopy is a radiochemistry measurement method that determines the energy and count rate of gamma rays emitted by radioactive substances. The method of γ -spectrometry allows the qualitative and quantitative analysis of the radionuclides in a material by analyzing the energy spectrum of the γ -quanta emitted after the β - or α -decay of the radionuclides in the material.

The equipment used in γ -spectrometry includes a high-purity Ge (HPGe) detector, a pulse sorter (multi-channel analyzer), and associated amplifiers and data readout devices. The OSURR high-purity Ge (HPGe) detector system is located inside a copper-lined, lead-brick housing and used to detect γ -rays.

Once each irradiation run was complete the test specimens were allowed to remain in the AIC for approximately two weeks. This allowed sufficient time for the short-lived high-energy isotopes (^{187}W) generated during the reactor run to decay to stable non-radioactive isotopes. After this "cooling off" period the samples were removed from the heater/AIC and were measured using a hand-held radiation monitor. The average surface dosimetry reading of each Group of specimens was approximately 2.0 rem/hr. The specimens were then separated and individually analyzed using a PC-based high-resolution γ -spectroscopy system at the Ohio State Nuclear Test Laboratory to determine the isotope and activity levels of the test specimens.

4.5.5 Safety

Both the Primary Investigator and Dr. Dan Kramer were approved by the University of Dayton's Radiation Safety Committee to be "Authorized Users" of radioactive material. Additionally, a protocol for this research was written, submitted for approval, and approved by the aforementioned committee. The protocol outlines the use, storage, security, risks, hazards, exposure and monitoring techniques associated with handling the irradiated test specimens. Additionally, the University of Dayton's radioactive materials license was amended to include isotopes that were generated during this research.

4.5.5.1 Security Measures

All irradiated test samples are stored in a lead shielded storage container within a locked repository (KL-142A), which is controlled by the University of Dayton's Office of Environmental Safety/Risk Management. Key control of this repository is strictly managed by the Environmental Safety/Risk Management Office and the Primary Investigator. Additionally a material control log is maintained that traces the material from arrival, testing and thru final disposition.

4.5.5.2 Shipping

All shipping of irradiated material from the Ohio State Nuclear Test Laboratory to the University of Dayton and from the University of Dayton to Oak Ridge National Laboratory were conducted in accordance with 49 CFR 173, which prescribes requirements to be observed in preparing hazardous materials for shipment by air, highway, rail, or water, or any combination thereof.³⁵

4.5.5.3 Disposal of Irradiated Materials

Once the research is complete, the irradiated samples will be packaged and shipped in accordance with DOT regulation 49 CFR 173 to The Ohio State Nuclear Test Laboratory, which has agreed to be responsible for the final disposition and disposal of the test samples in accordance with their waste disposal procedures and protocol.

4.5.5.4 Risk Mitigation

Control measures are employed by the Primary Investigator to reduce the level of personnel radiation exposure as much as reasonably possible. These measures include, but are not limited to: training; employing ALARA (As Low As Reasonably Achievable) principles through time, distance and shielding; use of protective clothing when needed (i.e. gloves/laboratory smock); external radiation dosimetry; periodic room surveys; and implementation of administrative control and access measures to the material.

Additionally, the Office of Environmental Safety/Risk Management has established Radiation Control Areas (RCA) in campus laboratories where the testing of the irradiated materials is conducted. RCAs are clearly marked and barricaded areas within a laboratory where access is restricted and requires enhanced controls for radiation exposure.

Although all of the testing equipment necessary to complete this research is not located in one campus laboratory, the testing of irradiated samples may not occur in two campus laboratories simultaneously. This requirement was imposed by the Radiation Safety Committee to mitigate the necessity of managing multiple radiation control areas simultaneously and to reduce the probably of unintended radiation exposure to campus students and faculty.

4.6 Tensile Testing

4.6.1 Set-up

Set-up tensile tests were conducted at various temperatures and strain rates using an Instron 55R1122 tensile test machine with a 1000 pound load cell (Figure 4.6.1), 200 lb capacity Instron 2712-015 pneumatic side action grips (Figure 4.6.2), and Instron Bluehill 2 software. The objective of these tests was to characterize the mechanical properties of the two alloys. Initially, two strain rates and test temperatures were selected and a design of experiments (DoE) was developed to determine the effects of the variables of irradiation levels, strain rate, and test and irradiation temperatures. However, due to limited availability of the tensile test facility and the desire to minimize personnel radiation exposure, it was determined that only one strain rate would be used. In accordance with Gourdin's work with T-111, a strain rate of 0.0017 s^{-1} was selected in order to elucidate any variation in the work hardening mechanisms resulting from the experimental variables.³⁶ Irradiated and non-irradiated Ta-10%W and T-111 tensile specimens were tested at 25°C and 300°C.

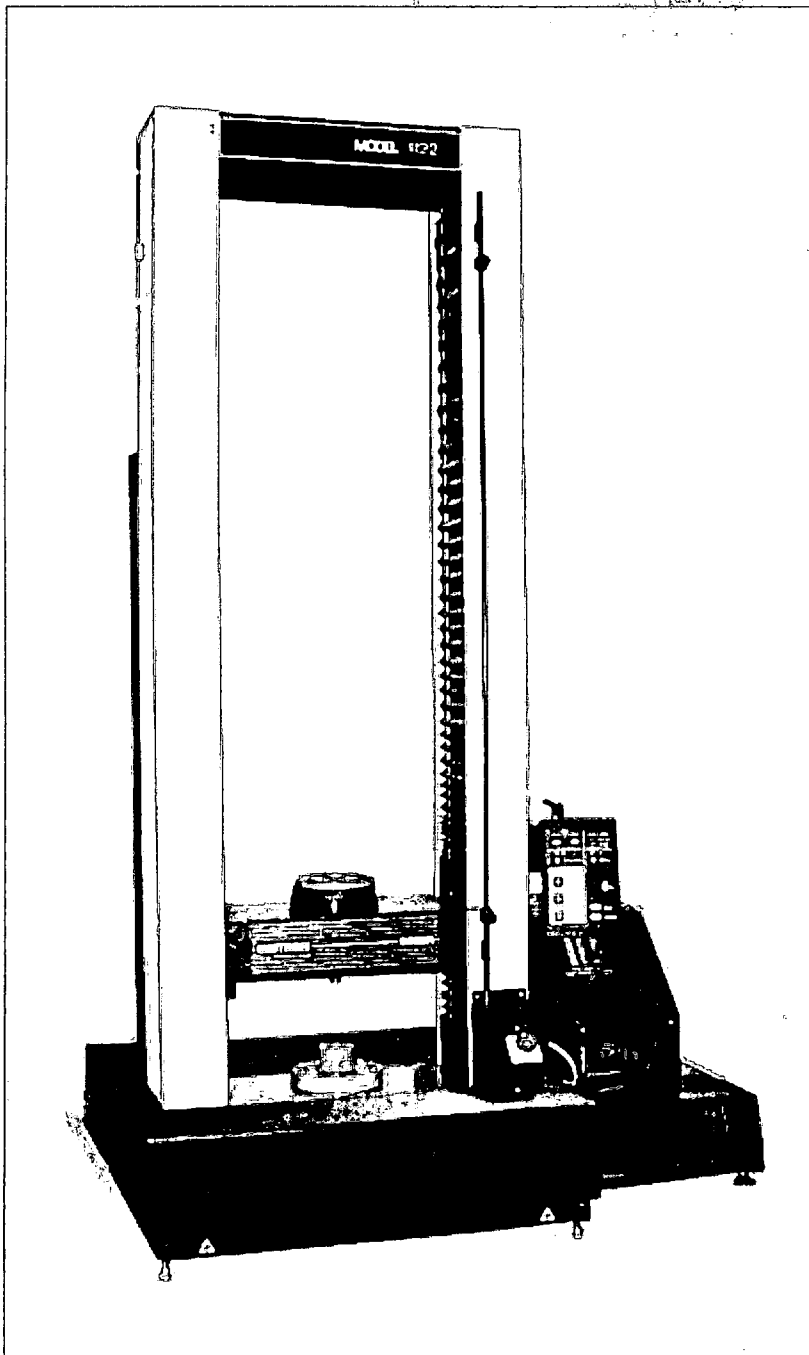


Figure 4.6.1. Instron 55R1122 Tensile Test Machine.

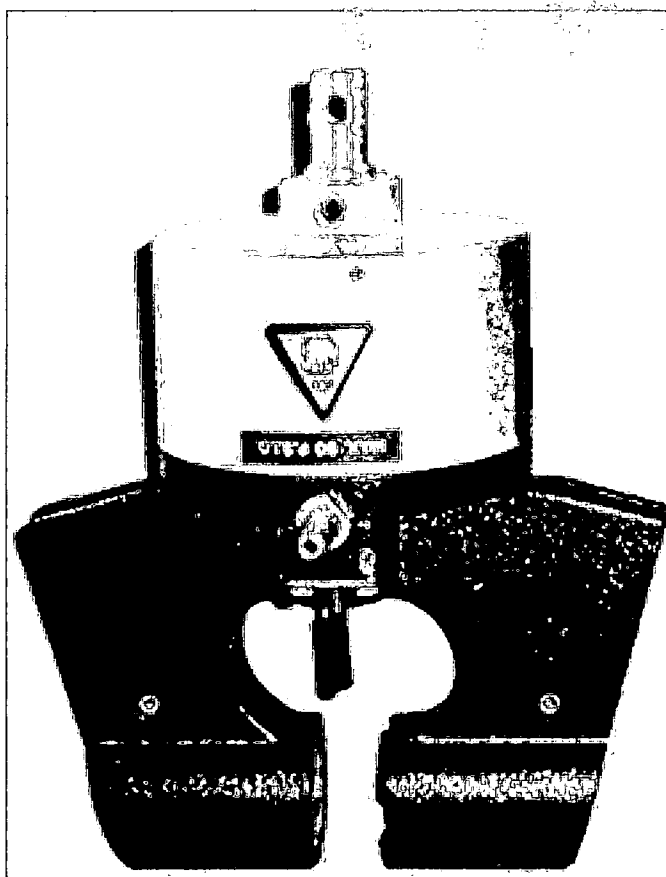


Figure 4.6.2. Instron 2712-015 Pneumatic Side Action Grips.

4.6.2 Experimental Design Matrix

Originally, a $2\sqrt{5-1}$ fractional factorial design of experiments was designed for the tensile experiments associated with this research. However, as discussed in Section 4.6.1, a single strain rate was selected thus reducing the number of factors from five to four. Therefore, the tensile experiments incorporated a 2^4 full factorial design of experiments³⁷ as shown in Table 4.6.1. This allowed for a systematic and efficient approach to the experimentation and yielded relevant statistical information. There are several advantages with a factorial design compared to the more traditional one-factor-at-a-time approach. The two main advantages are:

- a) The ability to detect and estimate interactions among the factors under study; and
- b) The possibility to reduce the number of tests necessary to obtain sufficient information.

Test Condition Number	Material	Irradiation Level (10^{15} nvt)	Irradiation Temp ($^{\circ}\text{C}$)	Tensile Temp ($^{\circ}\text{C}$)
1	Ta-10W	0	25	300
2	T-111	0	25	25
3	Ta-10W	1.2	25	25
4	T-111	1.2	25	300
5	Ta-10W	0	350	25
6	T-111	0	350	300
7	Ta-10W	1.2	350	300
8	T-111	1.2	350	25
9	Ta-10W	0	25	25
10	T-111	0	25	300
11	Ta-10W	1.2	25	300
12	T-111	1.2	25	25
13	Ta-10W	0	350	300
14	T-111	0	350	25
15	Ta-10W	1.2	350	25
16	T-111	1.2	350	300

Table 4.6.1. The 2^4 full factorial design of experiments matrix.

In the full factorial design, shown in Table 4.6.1, the independent variables of irradiation fluence, irradiation temperature and tensile test temperature are varied simultaneously according to the factorial design matrix. Due to limited Ta-10%W

and T-111 material availability, the tensile experiments only incorporated one replication.

Once the tensile testing was completed, the effects of the three separate independent variables (irradiation fluence, irradiation temperature and tensile test temperature) on the tensile properties of both Ta-10%W and T-111 were studied. An Analysis of Variance (ANOVA) was employed to determine the effect of each of the independent factors on the tensile properties of yield, UTS, modulus and elongation. To test the differences between individual sample means of yield, UTS, modulus and elongation, F-tests were performed as part of the ANOVA. The F-test is an overall test of the null hypothesis that group means of the dependent variable do not differ. It is also used to test the significance of each main and any interaction effects. The significance level, p , which indicates the probability that the differences observed in the data is due to chance, was chosen as 0.05. For all tests, $p < 0.05$ indicates that any differences in the yield, UTS, modulus and elongation are significant.

4.6.3 Testing

In accordance with Table 4.6.1, Ta-10%W and T-111 mechanical test specimens were tensile tested using an Instron 55R1122 tensile test machine with a 1000 pound load cell, 200 lb capacity Instron 2712-015 pneumatic side action grips and Instron Bluehill 2 software. A constant strain rate of 0.0017 s^{-1} was used to test all the specimens. A total of four irradiated and four non-irradiated Ta-10%W

and T-111 specimens were tested at 25°C and an equal amount of samples were tested at 300°C. To heat the specimens a Watlow MB1A1JN2-C12 Band Heater (Figure 4.6.3) was employed with a Cole-Palmer Digi-Sense advanced temperature controller. All heated specimens, were allowed to thermally equilibrate for 300 seconds before initiation of the test. The test duration was approximately 180 seconds depending on the sample elongation. All individual specimens were handled with lint free cloths and gloved hands to prevent contamination from human body oils and other potential laboratory contaminants.

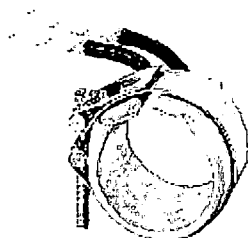


Figure 4.6.3. Watlow MB1A1JN2-C12 Band Heater.

4.7 Low-Temperature Creep/Stress Rupture

4.7.1 Background

Because tantalum and tantalum alloys are extremely sensitive to environmental contamination (such as oxidation, etc.), mechanical testing of these materials at elevated temperatures must be conducted using equipment also designed to test specimens in high-vacuum environments ($<1 \times 10^{-6}$ torr). There are very few creep test units in the United States that are equipped to test materials at elevated temperatures while under high-vacuum conditions.³⁸

For this research evaluation of the static tensile creep and stress rupture behavior was conducted at the UDRI High Temperature Mechanical Testing Laboratory. The High Temperature Mechanical Testing Laboratory houses 16 high-temperature creep frames with furnaces capable of operating at 1600°C for extended periods. This facility employs a unique laser interferometry system to measure tensile strain.

However, UDRI does not possess the capability to conduct elevated temperature creep testing in a high-vacuum ($<1 \times 10^{-7}$ torr) environment. As detailed in Sections 4.4 and 5.1, an analysis was conducted to determine the environmental effects, if any, of testing both Ta-10%W and T-111 in air at temperatures consistent with the service temperature ($<400^\circ\text{C}$) of these materials in several power system applications. The analysis discussed in Section 4.4 and 5.1 shows that exposure in air at temperatures below 400°C for periods of time consistent

with the duration of this elevated temperature rupture testing does not have a deleterious effect on the mechanical properties of either T-111 or Ta-10%W. Therefore, tensile creep data was generated in air at temperatures less than 0.15 T_m (~400°C) by measuring creep strain as a function of time, applied stress, and temperature.

The stress rupture resistance was evaluated by continuing each creep test until the specimen ruptures. For each material investigated, a minimum of two temperatures and two stresses were used to establish the stress and temperature sensitivities of the creep and stress rupture behavior.

4.7.2 Experimental Design Matrix

Specific to the creep experiments associated with this research a 2_v^{5-1} fractional factorial design³⁷ of experiments was employed. In this experimental design no main effects are confounded with any 2-factor or 3-factor interactions. However, main effects are confounded with 4-factor interactions. In the fractional factorial design, shown in Table 4.7.1, the factors irradiation level, irradiation temperature, creep load, and creep temperature are varied simultaneously according to the generic factorial design matrix. Due to limited Ta-10%W and T-111 material availability, the low-temperature creep/stress rupture experiments incorporated only two replications.

Test Condition Number	Material	Irradiation Level (10^{15} nvt)	Irradiation Temp ($^{\circ}\text{C}$)	Creep Load (MPa)	Creep Temp ($^{\circ}\text{C}$)
1	Ta-10W	0	25	620	300
2	T-111	0	25	620	25
3	Ta-10W	1.2	25	620	25
4	T-111	1.2	25	620	300
5	Ta-10W	0	350	620	25
6	T-111	0	350	620	300
7	Ta-10W	1.2	350	620	300
8	T-111	1.2	350	620	25
9	Ta-10W	0	25	690	25
10	T-111	0	25	690	300
11	Ta-10W	1.2	25	690	300
12	T-111	1.2	25	690	25
13	Ta-10W	0	350	690	300
14	T-111	0	350	690	25
15	Ta-10W	1.2	350	690	25
16	T-111	1.2	350	690	300

Table 4.7.1. The 2_5^{5-1} fractional factorial design of experiments matrix.

Once the low-temperature creep/stress rupture testing was completed, the effects of four separate independent variables (irradiation fluence, irradiation temperature, creep load and creep test temperature) on the low-temperature creep/stress rupture properties of both Ta-10%W and T-111 were studied. An Analysis of Variance (ANOVA) was employed to determine the effect of each of the independent factors on the low-temperature creep/stress rupture properties of rupture time, elongation and steady state creep rate. To test the differences between individual sample means of rupture time, elongation and steady state creep rate, F-tests were performed as part of the ANOVA. The F-test is an

overall test of the null hypothesis that group means of the dependent variable do not differ. It is used to test the significance of each main and any interaction effects. The significance level, p , which indicates the probability that the differences observed in the data is due to chance, was chosen as 0.05. For all tests, $p < 0.05$ indicate that any differences in the rupture time, elongation and steady state creep rate are significant.

4.7.3 Creep/Stress Rupture Testing

In accordance with the Table 4.7.1, Ta-10%W and T-111 mechanical test specimens were creep/stress rupture tested using four individual Applied Test Systems (ATS) model 2370 creep/stress rupture test systems (Figure 4.7.1). These ATS precision lever arm testers incorporate a number of enhanced design features allowing them to have a load accuracy of $\pm 0.5\%$. The frames are equipped with a 20:1 lever arm and were retrofitted with a novel video capture system for this research that incorporates an Intel CS430/CS431 PC camera coupled with Windows based personal computer. The video capture system has the capability to perform time lapse imaging set to user specified intervals and with a sensitivity to detect displacements as low as $6.35 \times 10^{-5}\text{m}$. The developed video capture software compiles the images and stores them as a Windows compatible video file. The video capture system acquires the sample elongation on the load-pan side of the lever arm at periodic intervals. The compiled video for a given test is then converted to raw elongation/time data, which is suitable for analysis.

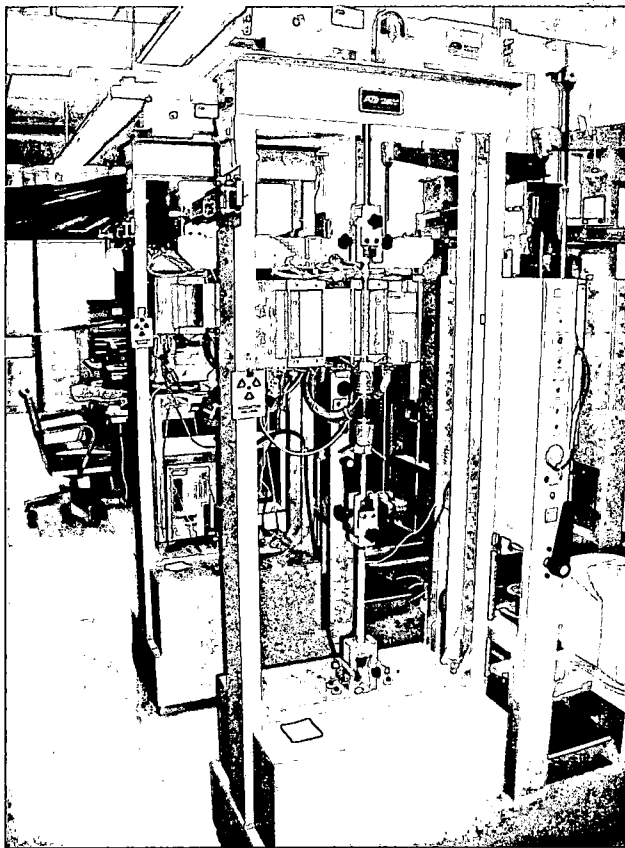


Figure 4.7.1. ATS model 2370 creep/stress rupture test system.

A Watlow MB1A1JN2-C12 Band Heater (Figure 4.6.3) controlled by a Cole-Palmer Digi-Sense advanced temperature controller was employed to heat the irradiated and non-irradiated Ta-10%W and T-111 specimens to 300°C. All sixteen specimens were allowed to thermally equilibrate for 300 seconds before initiation of each test. All thirty-two specimens were handled with lint free cloths and gloved hands to prevent contamination from human body oils and other potential laboratory contaminants.

4.8 Scanning Electron Fractography

For the purposes of this research Scanning Electron Microscopy (SEM) is an essential tool for characterizing the fracture surfaces of irradiated and non-irradiated Ta-10%W and T-111 tensile and/or stress rupture specimens. The fracture surfaces of the stress ruptured samples of irradiated and non-irradiated Ta-10%W and T-111 were examined using a JEOL JSM-840 SEM (Figure 4.8.1) to document any difference in the failure modes and/or mechanism due to effects of neutron irradiation. This research was conducted at the Metallography Laboratory at the University of Dayton Research Institute (UDRI), located in Dayton, Ohio.

4.8.1 Sample Preparation

Failure analysis specimens for SEM analysis were sectioned from irradiated and non-irradiated Ta-10%W and T-111 using a precision wire saw. Care was taken to collect any filings from the irradiated samples. These filings are stored with the remaining irradiated test specimens in KL-142A, and will remain there until shipped to the OSURR for disposal upon the termination of this research. The specimen sizes were approximately 0.63 cm wide x 0.31 cm long x 0.05 cm thick. In most cases the entire fracture surface was removed from the tested specimen. The samples were cleaned with methyl alcohol, dried and then secured to a JEOL specimen mount using conductive double sided adhesive discs. All individual specimens were handled with lint free cloths and gloved hands to

prevent contamination from human body oils and other potential laboratory contaminants.

The JEOL JSM-840 is a thermal emission SEM with an accelerating voltage ranging from 200 V to 40 kV. Its magnification ranges from 10x to 300kx with a resolution of 4 nm.

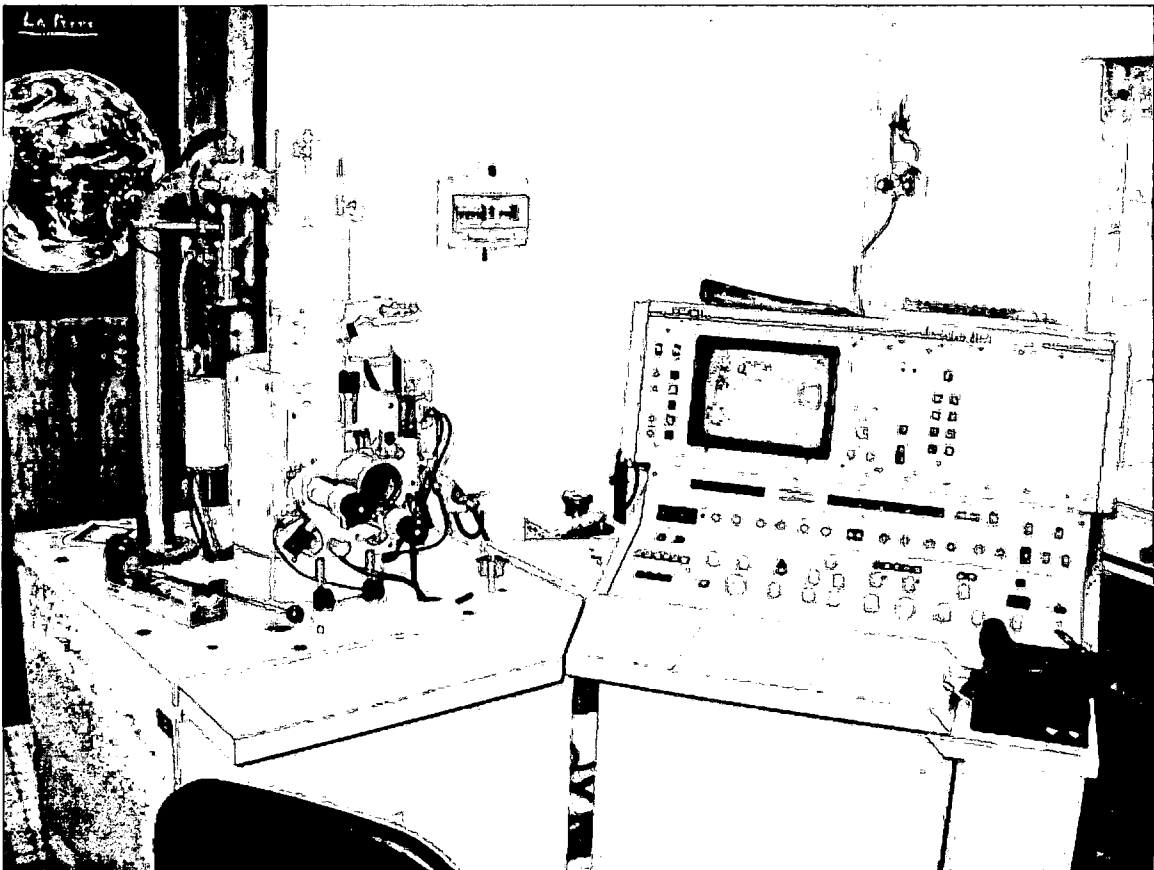


Figure 4.8.1. JEOL JSM-840 SEM.

4.9 Transmission Electron Microscopy

4.9.1 Background

In support of this research, selecting analytical techniques that can obtain elemental surface analysis and surface imagery with high spatial resolution was employed to elucidate the hypothesis that T-111 exhibited increased levels of dislocation pinning from the interstitial defects resulting from the neutron irradiation displacement damage as compared to Ta-10%W. A Transmission Electron Microscope (TEM) coupled with Electron Diffraction and Energy Dispersive X-ray Spectroscopy (EDS) was selected.

The Hitachi H-7600 TEM located in the University of Dayton's Nanoscale Engineering Science and Technology (NEST) Laboratory only has a maximum accelerating voltage of 120 kV. This TEM is designed specifically for applications in research fields such as biology, medicine, polymers and other advanced materials. Unfortunately, the accelerating voltage required to effectively conduct TEM analysis of high atomic number (Z) materials such as tantalum and tungsten is 200 kV.

As a result, the Primary Investigator contacted the Materials Analysis User Center (MAUC) of the High Temperature Materials Laboratory (HTML) at Oak Ridge National Laboratory, located in Oak Ridge, Tennessee. This and five other user centers at HTML are available to researchers in industry, universities, and federal laboratories.

The TEM selected to support this research was a Hitachi HF-2000 field-emission gun transmission (FEG) TEM located at ORNL's HTML (Figure 4.9.1). This TEM has a 1-nm spatial resolution, an energy dispersed X-ray spectrometer (EDS), and a Gatan imaging filter/energy loss spectrometer. The sample preparation and microscopy was conducted under research proposal HTML20006-040 pursuant to User Agreement UA-91-026 between UT-Battelle, LLC and the University of Dayton Research Institute.

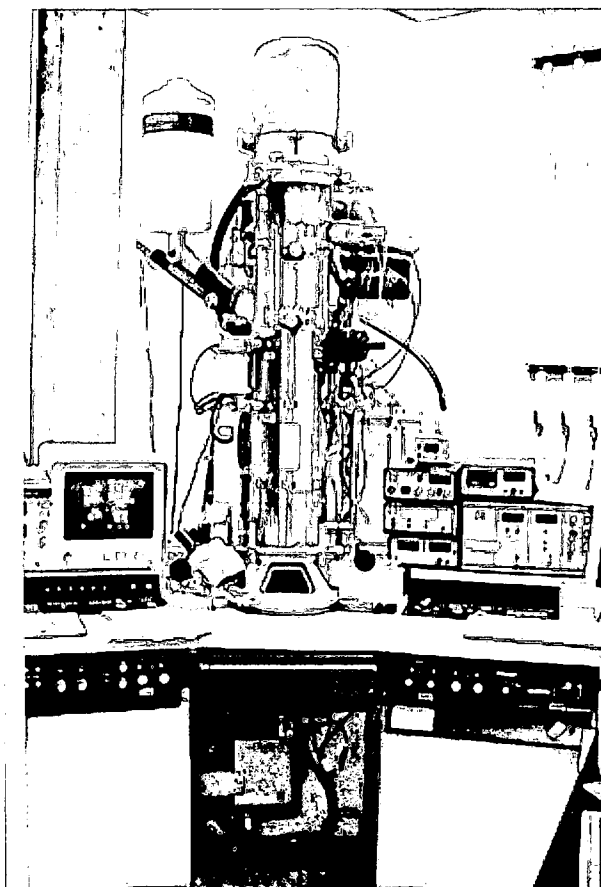


Figure 4.9.1. HF-2000 FEG-TEM.

4.9.2 Sample Preparation

TEM samples were prepared utilizing one of the two methods: 1) electropolishing and 2) focused ion beam (FIB) micro-milling.

1. Electropolishing was conducted utilizing a Struers TenuPol-3 device with an electrolytic acid solution of Methanol-7% Sulfuric Acid at -12/-15°C, 12v, a flow of 2.8 and a sensitivity of 8.5. In this process electrolyte flows from nozzles containing the cathode connections to the specimen that serves as the anode. Electropolishing is accomplished through the formation of an anodic film of electrolyte on the specimen surface. Through an electro-chemical reaction, this film removes material from the specimen's surface. Due to the current distribution within the specimen, electropolishing results in an overall smoothing of the specimen surface. Cooling of the electrolyte and the specimen to low temperatures is highly beneficial because it slows the electropolishing process. This minimizes the heat of reaction on the specimen and prevents vaporization of the electrolyte. The specimen thickness in areas of analysis must be less than 100 nm.

The thin foils were prepared by a double jet electropolishing. Several 3 mm diameter cylinders were cut out from the long axis of the fracture specimen or along the rolling direction of the control samples. The cylinders were sectioned with a precision wire saw in order to obtain

representative specimens adjacent to the fracture surface for TEM analysis.

2. Sample preparation on some samples employed a Hitachi FB-2000 FIB (Focused Ion Beam Micromill), which uses Gallium ions (Ga^+) to preferentially remove material. This device allows for the simultaneous observation and cross sectioning of a sample at any specified location. One key advantage to this method of sample preparation is that both the FIB and TEM employ a common sample holder thus facilitating the handling of samples between the two systems. This prevents sample damage, contamination, cracking, or loss during sample transfer. Approximately 2-3 samples/day can be processed from FIB milling to TEM observation, which is larger by an order of magnitude than electropolishing. The specimen thickness is 50-60 nm.

Unfortunately, the FIB process did not consistently yield samples suitable for microstructural analysis. The T-111 and Ta-10%W samples processed with focused ion beam showed amorphization damage by the ion beam. Instead of pursuing the development of parameters to remove the amorphization damage caused during the FIB preparation by "soft milling" it was decided to electropolish all the samples used in this research.

Dislocation substructures in the strained materials were studied using a transmission electron microscope (TEM) under an accelerating voltage of 200 kV. Each thin foil was examined under varying tilt angles with respect to the electron beam. EDS analysis was performed using a fine electron probe of less than 2 nm in diameter with an average X-ray count time of 100 seconds.

CHAPTER V

RESULTS AND DISCUSSION

"There are two possible outcomes: If the result confirms the hypothesis, then you've made a measurement. If the result is contrary to the hypothesis, then you've made a discovery."
- Enrico Fermi

This chapter describes the mechanics for achieving the conclusions presented in this research. The organization and discussion of the results of this research are presented in a sequence that allows for the logical progression of the embedded analysis to show that the conclusions are defensible.

5.1 Oxidation Experiments of Ta-10%W and T-111

5.1.1 Weight Changes of Ta-10%W and T-111 at 300°C and 400°C

Changes in oxygen concentration of Ta-10%W and T-111 were determined as a function of time and temperature by heating separate specimens in a furnace in atmospheric laboratory air at 300°C and 400°C then measuring weight change of the specimens at periodic intervals. The raw data of these experiments are shown in Table 5.1.1. The Ta-10%W and T-111 specimens tested at 300°C were exposed to atmospheric laboratory air for a total of approximately 300 hours, whereas samples testing in the same environment at 400°C were exposed for a total of 480 hours.

As shown in Figure 5.1.1, the weight gains of Ta-10%W and T-111 samples due to oxidation in air (209,460 ppm O₂) at 300°C and 400°C are initially parabolic and become linear with time. As shown is Figure 5.1.2, the oxidation rates at 400°C for both materials are initially high but decrease rapidly over time, ultimately converging to a constant rate.

Time (hr)	Mass Ta10W (gr)	Weight Gain Ta10W (mg/cm ²)	Weight Gain Ta10W (ppm O ₂)	Oxidn. Rate Ta10W (ppm/hr)	Mass T-111 (gr)	Weight Gain T-111 (mg/cm ²)	Weight Gain T-111 (ppm O ₂)	Oxidn. Rate T-111 (ppm/hr)
300°C								
0	1.8624	0	0	0	1.7419	0	0	0
2	1.8624	0.0000	0.00	0.00	-	-	-	-
20	1.8624	0.0000	0.00	0.00	-	-	-	-
44	1.8624	0.0000	0.00	0.00	-	-	-	-
67	-	-	-	-	1.7421	0.1346	157.73	2.35
120	1.8624	0.0000	0.00	0.00	-	-	-	-
307	-	-	-	-	1.7422	0.2019	236.59	0.77
310	1.8624	0.0000	0.00	0.00	-	-	-	-
400°C								
0	1.9306	0	0	0	1.7080	0	0	0
1	1.9306	0.0000	0.00	0.00	1.7080	0.0000	0.00	0.00
4	1.9307	0.0625	72.72	18.18	1.7081	0.0659	77.26	19.32
24	1.9310	0.2499	290.88	12.12	1.7082	0.1318	154.53	6.44
48	1.9312	0.3749	436.32	9.09	1.7083	0.1978	231.79	4.83
174	1.9315	0.5624	654.48	3.76	1.7085	0.3296	386.31	2.22
480	1.9317	0.6874	799.92	1.67	1.7090	0.6592	772.63	1.61

Table 5.1.1. Data of oxidation experiments on Ta-10%W and T-111 at 300°C and 400°C.

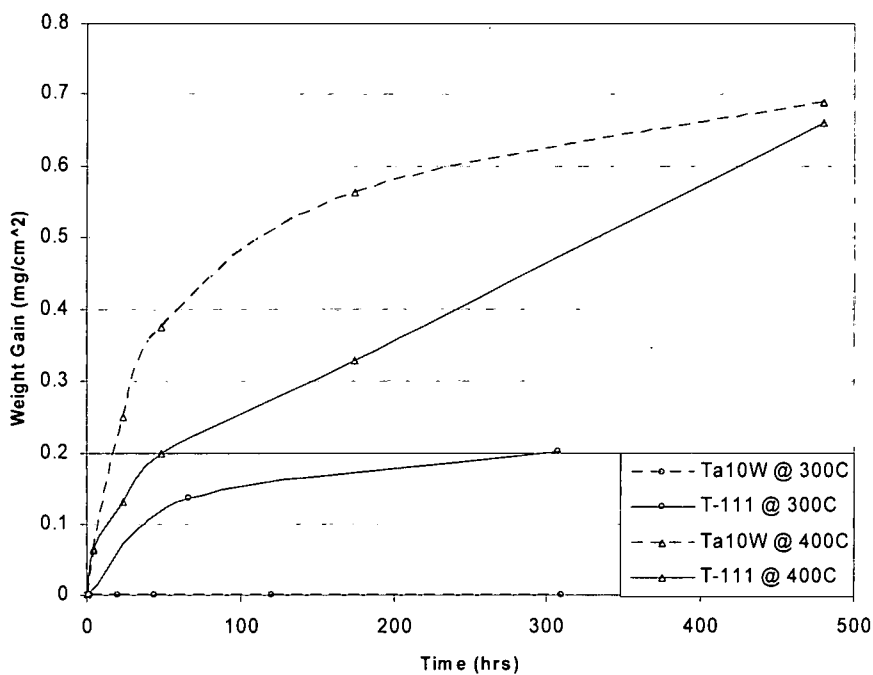


Figure 5.1.1. Oxidation Weight Gains of Ta-10%W and T-111 in Air.

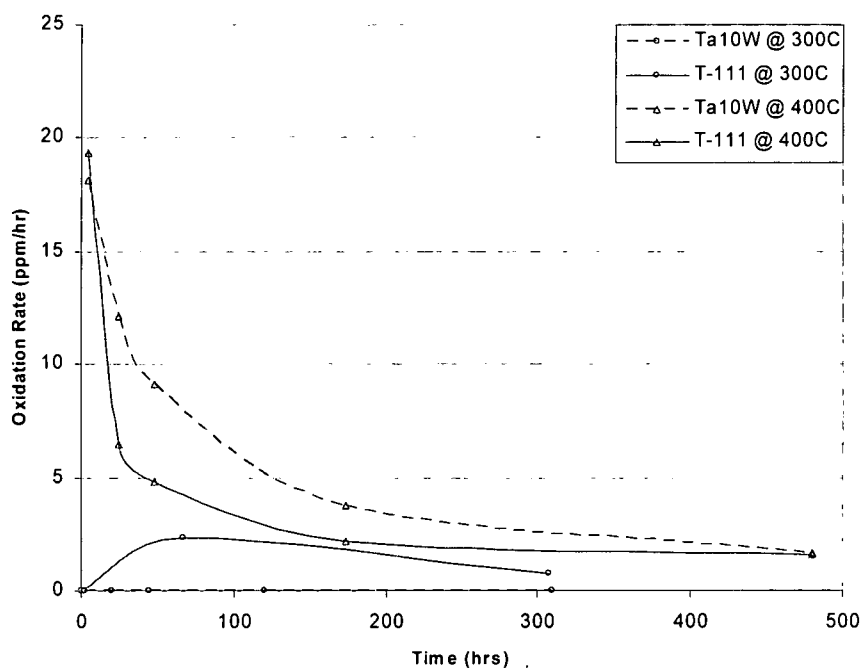


Figure 5.1.2. Oxidation Rate of Ta-10%W and T-111 in Air.

At 300°C the oxidation rate behavior of both materials is negligible. These results confirm that oxidation of Ta-10%W and T-111 at temperatures below 400°C is non-diffusion controlled and primarily superficial.

5.1.2 Effects of the Irradiation Environment on T-111

Both materials show weight gains as a result of exposure to atmospheric laboratory air at 400°C, but this does not provide any verification of the effect of the <1000 ppm O₂ at 350°C irradiation environment on the mechanical properties of the specimens used in this research. Therefore, a T-111 specimen was heated to 350°C for 4-hours in an inert atmosphere that contained <1000 ppm O₂. The specimen was then creep tested at 25°C with a load of 620 MPa.

Figure 5.1.3 compares the low-temperature creep/stress rupture results of two T-111 specimens tested at 25°C with a load of 620 MPa. The results represented by the solid line are from the specimen that was exposed to 350°C for 4-hours in an inert atmosphere that contained <1000 ppm O₂; whereas the results represented by the dashed line are from a virgin non-irradiated T-111 specimen. Figure 5.1.3 shows that there is no significant difference in the data between these two samples.

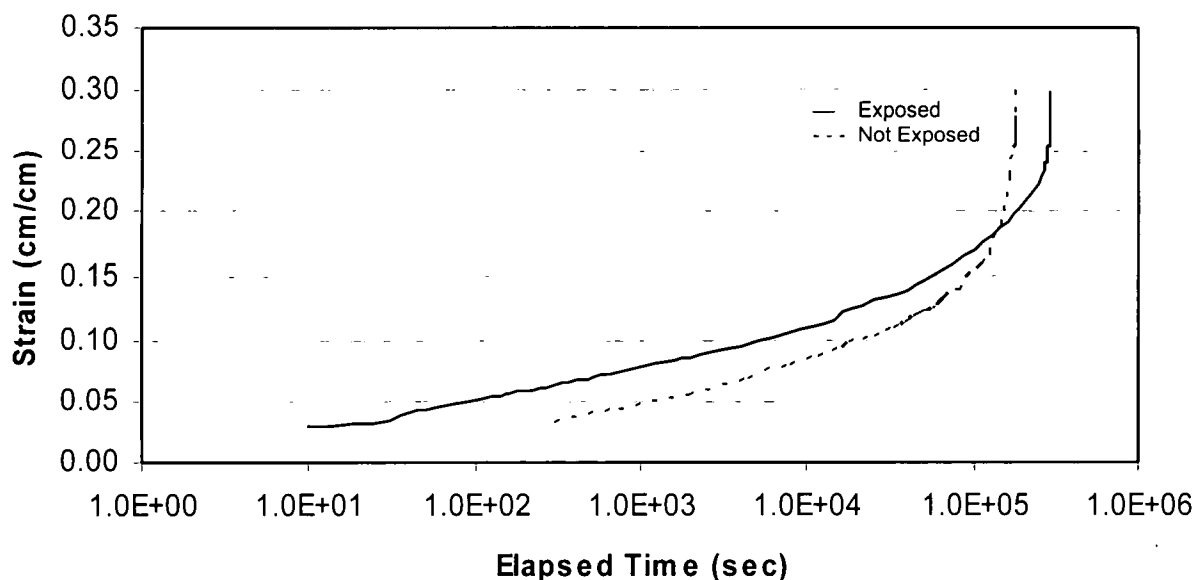


Figure 5.1.3. Low-temperature creep/stress rupture results of two T-111 specimens tested at 25°C with a load of 620 MPa.

5.1.3 Summary

In general, the weight gains of Ta-10%W and T-111 due to oxidation in air at temperatures less than 400°C are initially parabolic and become linear with time. Additionally, the oxidation rates 400°C for both materials are initially high but decrease rapidly over time ultimately converging to a constant rate. At 300°C the oxidation rate behavior of both materials is negligible. These results confirm that oxidation of Ta-10%W and T-111 at temperatures below 400°C is non-diffusion controlled and primarily superficial. These results are consistent with observations for the oxidation of tantalum.³⁹

Furthermore, it is shown that heating T-111 specimens to 350°C in an inert atmosphere that contains (<1000 ppm O₂) has a negligible effect on the

mechanical properties of the specimens tested in this research. This is significant because it definitively demonstrates that changes in the mechanical properties of Ta-10%W and T-111 resulting from the 4-hour irradiation in the OSURR result from the effects of the neutron irradiation and not any potential oxidation effects associated with heating the specimens to 350°C in <1000 ppm O₂ atmosphere.

5.2 Gamma Spectrometry

The Ta-10%W and T-111 specimens irradiated during this research were subjected to γ -spectrometry to determine the specific activity of the ^{181}Hf and ^{182}Ta isotopes formed as a result of the slow-neutron capture process. The resulting specific activities of ^{181}Hf and ^{182}Ta were used to calculate the neutron fluence associated with the irradiation runs in the OSURR.

The data shown in Appendix A are representative γ -spectrometry results for irradiated Ta-10%W and T-111 mechanical test specimens respectively. Although the γ -spectrometry results of all of the mechanical test specimens show the amount of radioactive activity in each sample, the cumulative data of all the samples has more relevance in demonstrating that the 49 CFR 173 transportation requirements for radioactive material and the University of Dayton License for Radioactive Material are not exceeded during shipment and storage respectively.

As a result of exposing Ta-10%W and T-111 to a neutron fluence level of 1.2×10^{15} nvt, approximately 20 $\mu\text{Ci/g}$ of isotope ^{182}Ta are formed in both Ta-10%W and T-111, and 0.2 $\mu\text{Ci/g}$ of isotope ^{181}Hf is formed in T-111 as a result of the slow-neutron capture process.

The neutron spectrum, total fluence and material damage will be discussed in Section 5.3.

5.3 Neutron Damage

5.3.1 Total Flux Determination

Figure 5.3.1 is a histogram depicting the differential flux of the neutrons emitted by the OSURR versus the energy of those neutrons. Fundamentally, this spectrum represents the flux that the irradiated specimens were exposed to within the cadmium wrapped ceramic fiber heater in the AIC during operation of the reactor. This measurement was determined by:

- a) running the reactor at 50 kW and irradiating cadmium shielded copper, gold and cobalt wires;
- b) conducting γ -spectrometry of the wires to extrapolate the reactor flux measurements; then
- c) scaling up the results to a reactor power of 450 kW, which is the power level used during the specimen irradiation experiments.

The cumulative total flux was obtained by summing the flux over the range of energies, which yields a total flux of 8.23×10^{10} nv. Multiplying the total flux by the 4-hour irradiation time yields a total fluence of approximately 1.2×10^{15} nvt.

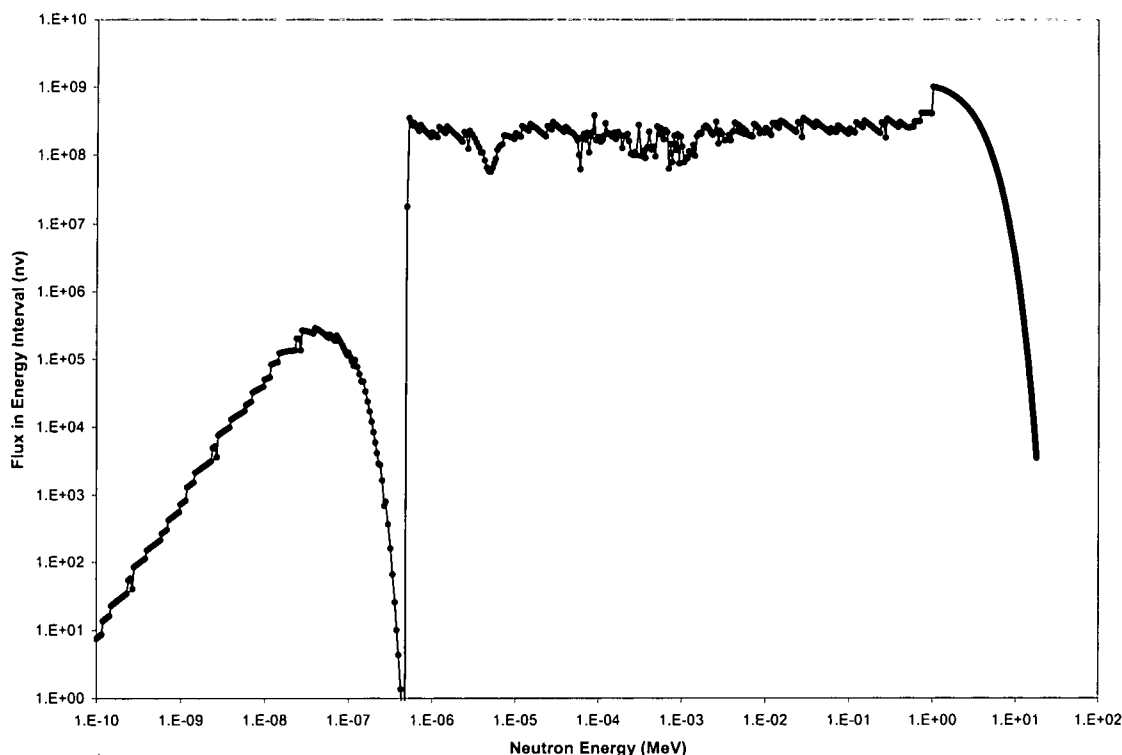


Figure 5.1.3. Differential Flux versus Energy of Research Experiment Package in the OSURR at 450 KW.

The cylindrical ceramic fiber heater used to irradiate the test specimens was wrapped with 0.102 cm thick cadmium sheet material to suppress thermal flux. Cadmium has a large absorption cross-section for neutrons below 0.4 eV and drops off to a negligible level above this energy. As shown in Figure 5.3.1, the cadmium shielding effectively removes “thermal” neutrons below the “cadmium cutoff energy” of 0.4 eV. Approximately, 95% of the flux has energy above the cadmium cutoff energy of 0.4 eV. Therefore, the majority of the neutron flux used to irradiate the test specimens is mostly epithermal flux

5.3.2 Displacement Damage Calculation

A major source of neutron irradiation damage in metals is the displacement of atoms from their normal lattice sites. Hence, an appropriate damage exposure index is the number of times, on the average, that an atom has been displaced during an irradiation. This can be expressed as the total number of displaced atoms per unit volume, per unit mass, or per atom of material. Displacements per atom are the most common way of expressing this quantity and are described quantitatively by the number of displacements per atoms (dpa) over a certain period of time. The dpa number associated with a particular irradiation depends on the amount of energy deposited in the material by the neutrons.

The dpa for T-111 and Ta-10%W for this research was calculated using ASTM Standard E693-01.⁴⁰ Although this practice is specific to iron, the general procedures apply to any material for which a displacement cross section $\sigma_d(E)$ is known. Since the fluence rate spectrum is constant over the duration of the irradiation, the dpa of the materials used in this research is calculated as follows:

$$dpa = \phi_{tot} t \int_0^{\infty} \sigma_d(E) \psi(E, t) dE dt = \phi_{tot} t \bar{\sigma}_d = \phi_{tot} t \left(\frac{\eta \sigma T_{dam}}{2 E_d} \right) (1 \times 10^{-24} \text{ cm}^2 \text{ barns}^{-1}) \quad [5.3.1]$$

Where:

- ϕ_{tot} = Total neutron fluence of (n/cm²-s)
- ψ = Normalized fluence rate (n/cm²)
- $\bar{\sigma}_d$ = Displacement cross section for a particular material (barns)
- σT_{dam} = Averaged damage energy cross-section (barns-keV)
- E_d = Effective threshold displacement energy (keV)
- η = Averaged defect production efficiency
- t = Irradiation time (s)

A considerable body of irradiated materials data has been reported by Broeders and Konobeyev³⁴ and the data associated with the materials of interest to this research are shown in Table 5.3.1. The calculated dpa from equation 5.3.1 is also shown for both Ta-10%W and T-111 in Table 5.3.1.

Element	Neutron Displacement Energy (keV) ³⁴	Damage Energy Production Cross Section (barns-keV) ³⁴	Defect Production Efficiency Factor ³⁴	Particle Flux $\times 10^{10}$ (n/cm ² -s)	Irradiation Time (s)	DPA $\times 10^{-7}$
Ta	0.09	55	0.73	8.23	14400	2.64
W	0.09	55	0.61	8.23	14400	2.21
Hf	0.025	100	0.8	8.23	14400	19.0
					Ta-10%W	2.60
					T-111	2.94

Table 5.3.1. Irradiated Materials Data and dpa Calculation for Ta-10%W and T-111.

5.3.3 Discussion

The approximate atomic displacement damage, described quantitatively by the number of displacements per atoms (dpa) over a certain period of time, for both T-111 and Ta-10%W irradiated test specimens is approximately 3.0×10^{-7} dpa.

Irradiation with fast neutrons affects mechanical properties by:

1. The formation of Frenkel defects (vacancy – interstitial pairs) and;
2. The production of displacement spikes and possibly dislocations.

At fluence levels below 3.0×10^{-19} nvt, lattice parameter and crystal density changes suggest that Frenkel defects or very small cluster defects are formed.⁴¹

Frenkel defects are couples of interstitial atoms and vacancies and play an important role in the physical and mechanical properties of solids. Since they can be induced by neutron irradiation, which knocks atoms out of their lattice positions, they are known to play an essential role in the radiation embrittlement of steels in nuclear devices.⁴²

Under uniform stress Frenkel defects will contribute to the creep rate by their interaction with dislocations. The introduction of these lattice defects makes the glide movement of dislocations more difficult. Although Schoeck states that at temperatures below $0.5 T_m$, a low concentration of Frenkel defects should not have a significant effect on the creep rate when the glide movement of dislocations is rate controlling,⁴³ this is not a universal scientific fact. At low temperatures ($<0.5 T_m$), interstitial partners of Frenkel pairs are mobile and wander through the lattice. They can be trapped by impurities, other interstitials, or dislocation lines; and when any of these occur stable damage is retained in the lattice.⁴¹ It was shown by Saraev⁴² that the presence of point defects alters the deformation and fracture behavior of α -Fe single crystals. From the analysis of stress-strain curves it was concluded that the strength, i.e. the stress values of the respective stress-strain curves, decreases with increasing number of Frenkel defects.

5.3.4 Visible Defect Density

Transmission electron microscopy (TEM) is a very powerful tool for investigating microstructural defects but it has limitations in investigating very low levels of atomic displacement damage (<0.0001 dpa) produced by neutron irradiation. This is because the low fluence levels associated with this research produce a low density of defects that are randomly distributed. According to Zinkle and Matsukawa,⁴⁴ these lower density defects should have a diameters less than 3 nm.

Zinkle and Matsukawa⁴⁴ confirm for both the FCC and BCC metals that most defects are not easily detectable in irradiated materials with atomic displacement damage below 1.0×10^{-4} dpa. The resulting small defect clusters, with diameters less than 3 nm, are generally too small to be seen by most current transmission electron microscopes (TEMs) due to defect invisibility resulting from poor contrast with the surrounding matrix. Foil thicknesses of ~ 100 nm that are commonly used for conventional electron microscopy studies are too thick to accurately observe the small defect clusters produced by low temperature neutron irradiation.

In order to determine the visible defect density of the atomic displacement damage imparted on the two tantalum alloys investigated in this research it is necessary to extrapolate irradiation dose data which is correlated with visible

defect accumulation. Unfortunately, there is insufficient neutron irradiation dose data that is correlated with visible defect accumulation for Ta or Ta-based alloys. However, Zinkle²² did estimate a neutron irradiation damage level ratio of 4:1 between steel and tantalum. Additionally, defect accumulation behavior is initially linear at very low doses (<0.0001) dpa⁴⁵ and approaches a constant density at high doses (>0.1 dpa).⁴⁶ Based on observed trends from multiple sources there appears to be one order of magnitude higher visible defect cluster density for alloys than their base metals. Therefore, based on these observations the approximate observable defect density for Ta-10%W and T-111 can be estimated.

Using Figure 5.3.2 as a guide, the following is the logical progression in estimating the visible defect density of irradiated Ta-10%W and T-111:

- a) Zinkle, et al.,⁴⁵ reported the visible defect density of iron within a range of displacement damages from 10^{-4} to 1 dpa.
- b) Since defect accumulation behavior is linear at very low doses ($<10^{-4}$ dpa)⁴⁶ the visible defect density for iron can be extrapolated for lower damage levels. In this case, down to 10^{-8} dpa.
- c) Zinkle²² states there is a neutron irradiation damage level ratio of 4:1 between steel and tantalum, thus a correlation between displacement

damage and visible defect density can be conservatively calculated for tantalum from iron using the 4:1 ratio.

d) Finally, based on the observation that alloys present one order of magnitude higher visible defect cluster density than their base metals, a correlation between displacement damage and visible defect density for Ta-10%W and T-111 can be estimated as show in Figure 5.3.2.

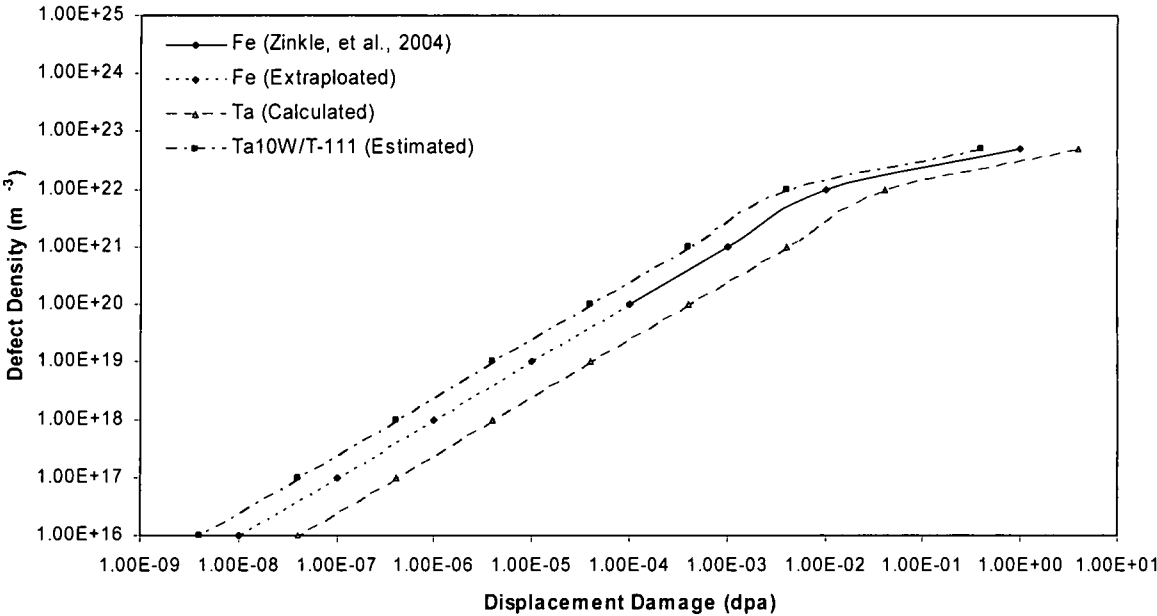


Figure 5.3.2. Observable Defect Density versus Displacement Damage for Fe, Ta, Ta-10%W and T-111.

Based on Figure 5.3.2 the estimated observable defect density for both Ta-10%W and T-111 for a displacement damage of 3.0×10^{-7} dpa is 7.35×10^{17} defects/m³. In effect, this visible defect density means that one irradiation produced defect in the Ta-10%W and T-111 specimens studied in this research may be visible in the TEM images shown in Section 5.8.

Consistent with the observations of Zinkle and Matsukawa,⁴⁴ it can be concluded that the defect clusters produced within irradiated Ta-10%W and T-111 specimens used for this research may not be observable using conventional TEM techniques.

5.4 Tensile Testing of Irradiated and Non-irradiated Specimens

One objective of this research is to characterize the response of the tensile properties of yield strength, UTS, elastic modulus and elongation of both Ta-10%W and T-111 to the variables of irradiation fluence, irradiation temperature and tensile test temperature. The tensile tests were conducted in accordance with the DoE outlined in Table 4.6.2, and the results are shown below in Table 5.4.1.

Test #	Sample S/N	Material	Irrad. Level (10^{15} nvt)	Irrad. Temp (°C)	Tensile Temp (°C)	Yield (MPa)	Tensile (MPa)	Modulus (10^7 MPa)	Elongation (%)
1	1C	Ta10W	0	25	300	502.68	598.94	1.21	15.26
2	T1C	T-111	0	25	25	629.34	696.80	1.09	34.96
3	2C	Ta10W	1.20	108*	25	671.65	731.32	1.11	25.54
4	T2C	T-111	1.20	108*	300	442.57	527.53	1.22	24.75
5	3C	Ta10W	0	350	25	693.35	746.69	1.01	23.69
6	T3C	T-111	0	350	300	427.92	517.64	.095	23.03
7	4C	Ta10W	1.20	350	300	511.69	617.55	1.07	15.35
8	T4C	T-111	1.20	350	25	664.37	740.98	1.15	29.17
9	5C	Ta10W	0	25	25	693.97	734.68	1.06	26.43
10	T5C	T-111	0	25	300	486.97	551.11	.097	26.20
11	6C	Ta10W	1.20	108*	300	548.67	599.08	1.65	15.15
12	T6C	T-111	1.20	108*	25	624.52	696.92	1.05	34.13
13	7C	Ta10W	0	350	300	516.04	607.53	1.07	15.28
14	T7C	T-111	0	350	25	644.15	723.17	1.00	32.77
15	8C	Ta10W	1.20	350	25	719.69	766.19	1.05	24.24
16	T8C	T-111	1.20	350	300	432.34	513.03	1.08	21.87

Table 5.4.1. Tensile test results. * Note: 108°C is the result of self heating during irradiation.

Figure 5.4.1 graphically represents the tensile test results of irradiated and non-irradiated Ta-10%W samples. As can be observed from the data plots, the testing temperature has a significant impact on the yield strength, UTS and elongation of the specimens regardless of the level of neutron radiation

exposure. An increase in test temperature from 25°C to 300°C did not have an effect on the elastic modulus of Ta-10%W but the variation in test temperature did result in an approximate: 29% reduction in yield strength, a 20% reduction in UTS, and a 40% reduction in elongation. The variation in tensile test temperature, as shown in the results of the ANOVA in Appendix B, has a significant response on the dependent variables, which must be taken into consideration when assessing the significance of each main and any interaction effects.

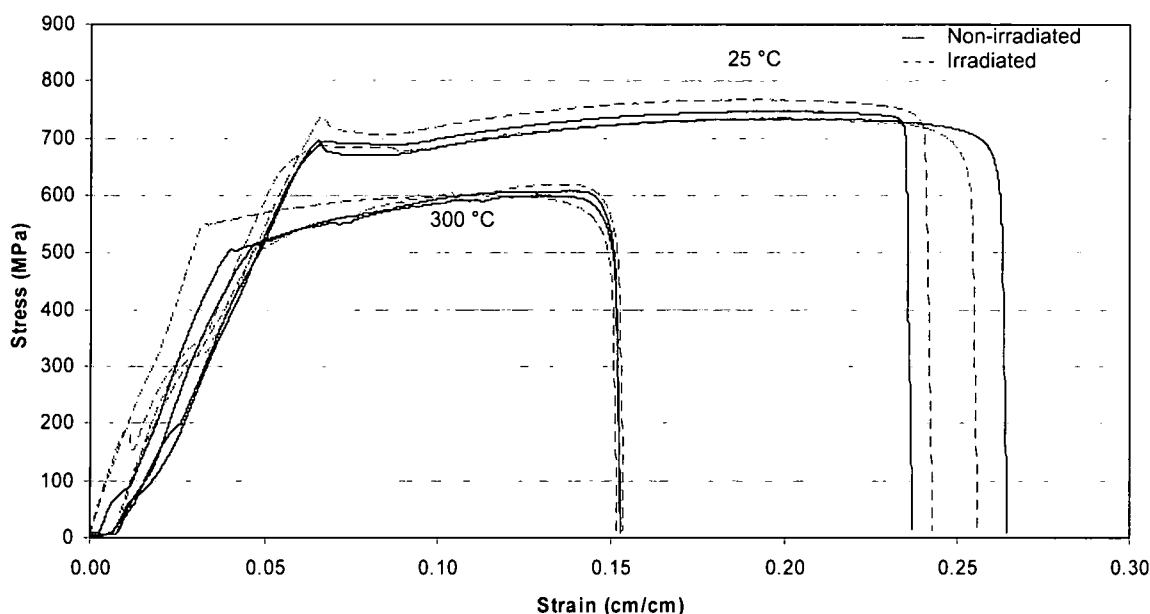


Figure 5.4.1. Tensile test results of irradiated and non-irradiated Ta-10%W samples. The samples with a failure strain of 15% were tested at 300°C; samples with a failure strain of approximately 25% were tested at 25°C.

Statistical Analysis System (SAS) software⁴⁷ was used to conduct an analysis of variance (ANOVA) for the Ta-10%W tensile tests. In addition to the statistical significance of varying the tensile testing temperature, the ANOVA indicated a

statistical difference in the effect of irradiation temperature vs. UTS ($p = 0.0135$). However, since this response is not reflected in the interaction of irradiation fluence level and irradiation temperature it appears that the response of irradiation temperature vs. UTS does not represent an actual significant difference. These results infer that the mechanical properties of Ta-10%W tested at 25°C and 300°C are unaffected when irradiated with a neutron fluence of $\sim 1.2 \times 10^{15}$ nvt at both 25°C and 350°C.

Figure 5.4.2 graphically represents the tensile test results of irradiated and non-irradiated T-111 samples. Similar to Ta-10%W, the results show that tensile testing temperature has a significant impact on the yield strength, UTS and elongation of the specimens regardless of the level of neutron radiation exposure. An increase in tensile test temperature from 25°C to 300°C did not have an effect on the elastic modulus of T-111, but the variation in test temperature results in an approximate: 31% reduction in yield strength, a 28% reduction in UTS, and a 25% reduction in elongation. As shown in the results of the ANOVA in Appendix B, the variations in tensile test temperature has a significant response on the dependent variables, which must be taken into consideration when assessing the significance of each main and any interaction effects.

Statistical Analysis System (SAS) software⁴⁷ was also used to conduct an analysis of variance (ANOVA) for the T-111 tensile tests. In addition to the

statistical significance of varying the tensile testing temperature, the ANOVA indicated a statistically significant difference in the effect of:

- a) Irradiation fluence level vs. elongation ($p = 0.0467$); and
- b) Irradiation temperature vs. elongation ($p = 0.0087$).

These results infer that the tensile property of elongation of T-111 tested at 25°C and 300°C are affected when irradiated with a neutron fluence of $\sim 1.2 \times 10^{15}$ nvt at both 25°C and 350°C. The yield strength, UTS and elastic modulus of T-111 are unaffected by the research parameters for irradiation fluence and irradiation temperature.

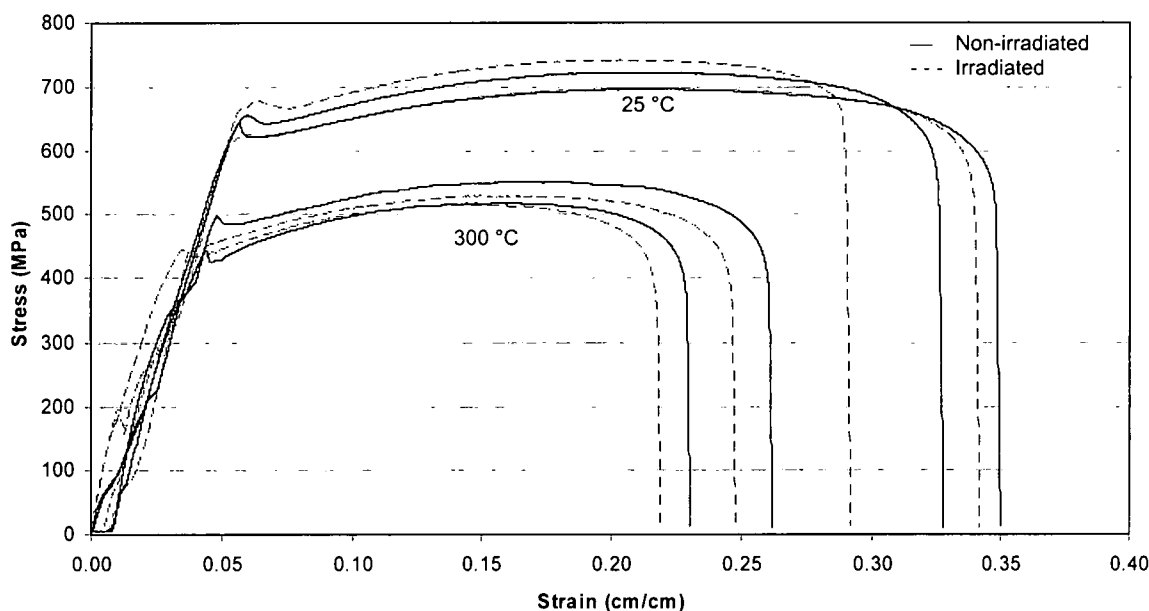


Figure 5.4.2. Tensile test results of irradiated and non-irradiated T-111 samples. The samples with a failure strain between 22-26% were tested at 300°C; samples with a failure strain between 29-35% were tested at 25°C.

5.4.1 Discussion

Referring to Figure 2.1.1, which is a comprehensive literature graph obtained from Dr. Zinkle that presents tensile elongation vs. displacement damage (dpa) of Ta-10%W after neutron irradiation at 70°C.¹⁶ It shows that no data regarding displacement damage at a level less than 0.001 dpa was found in literature, therefore the line labeled "Total Elongation" between 35% and 4% is extrapolated.

Figure 5.4.3, which includes data obtained from this research, graphically depicts the tensile elongation vs. displacement damage (dpa) behavior of Ta-10%W and T-111 after neutron irradiation. The referenced data points above 1.0×10^{-3} dpa are from the literature,^{16,22} and the data points below 3.0×10^{-7} dpa are based on the results of this research. The dashed lines between the known data points represent the Primary Investigator's hypothesized behavior of both alloys to increasing levels of displacement damage.

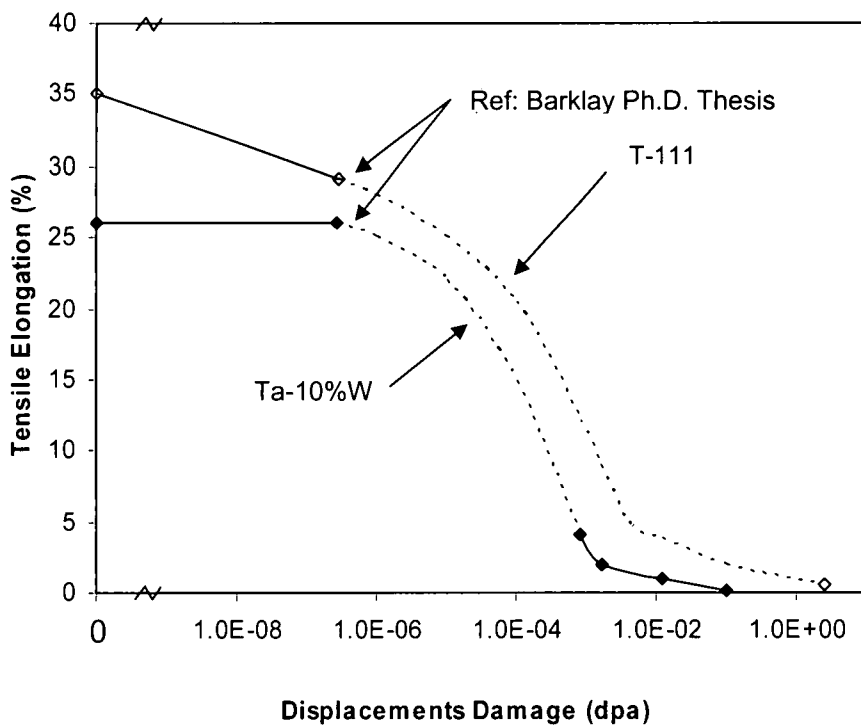


Figure 5.4.3. Tensile elongation vs. displacement damage (dpa) behavior of Ta-10%W and T-111. The dashed lines represent the Primary Investigator's hypothesized behavior of both alloys.

5.5 Low Temperature Creep/Stress Rupture Testing of Irradiated and Non-irradiated Specimens

The objective of these tests are to characterize the response of the rupture time, elongation at rupture and steady state creep rate of both Ta-10%W and T-111 to the variables of material (hafnium level), irradiation fluence, irradiation temperature, creep load and creep test temperature. The low-temperature creep/stress rupture tests were conducted in accordance with the DoE outlined in Table 4.7.2, the results of which are shown in Table 5.5.1.

Test #	Sample S/N	Matl.	Irrad. Level (10 ¹⁵ nvt)	Irrad. Temp (°C)	Load (MPa)	Creep Temp (°C)	Rupture Time (s)	Elong. (cm)	Steady State Creep Rate (m/s)
9	5A/5B	Ta10W	0	25	690	25	5.35E+03	0.5583	1.51E-06
5	3A	Ta10W	0	350	620	25	**	**	3.37E-10
1	1A/1B	Ta10W	0	25	620	300	3.00E+00	0.3203	1.07E-03
13	7B	Ta10W	0	350	606	300	1.10E+02	0.2344	2.13E-05
3	2A	Ta10W	1.20	108*	620	25	**	**	4.13E-10
15	8B/10A	Ta10W	1.20	350	690	25	3.46E+05	0.4394	1.48E-08
11	6A	Ta10W	1.20	108*	634	300	5.00E+00	0.3531	7.06E-04
7	4B	Ta10W	1.20	350	606	300	6.86E+02	0.2306	3.36E-06
2	T1A/T1B	T-111	0	25	620	25	1.59E+05	0.7173	2.13E-08
14	T7A/T7B	T-111	0	350	690	25	6.03E+02	0.3543	1.26E-06
10	T5B	T-111	0	25	490	300	3.36E+02	0.5601	1.67E-05
6	T3B	T-111	0	350	496	300	6.30E+04	0.5062	8.03E-08
12	T6A/T6B	T-111	1.20	108*	690	25	1.20E+02	0.7069	1.89E-05
8	T4A/T4B	T-111	1.20	350	620	25	1.19E+07	0.6269	1.36E-10
4	T2B	T-111	1.20	108*	496	300	2.01E+02	0.5169	1.54E-05
16	T8A/T8B	T-111	1.20	350	496	300	3.13E+04	0.4671	8.34E-08

Table 5.5.1. Creep/stress rupture test results. Notes: * denotes, due to self-heating during irradiation; ** denotes, did not fail.

The 108°C irradiation temperature shown in table 5.5.1 is the result of the specimens “self-heating” during the reactor run. “Self-heating” results from the

transfer of energy from the neutrons emitted from the OSURR reactor core during irradiation to the T-111 and Ta-10W specimens located in ceramic fiber heater within the AIC. Specific to this reactor run, the ceramic heater was turned-off with the initial temperature of 25°C. Once the reactor run was initiated, the specimens continued to self-heat until a thermal equilibrium was established at 108°C.

Similar to the results of this research associated with tensile testing, the creep/stress rupture test temperature has a dramatic impact on the response of the rupture time, elongation at rupture and steady state creep rate for low-temperature creep/stress rupture tests conducted on both Ta-10%W and T-111. The sensitivity of both alloys to the variation of creep/stress rupture test temperature at the 300°C level is sufficiently high enough that the statistical response of both alloys to this test temperature overwhelms the alloy's responses to the remaining independent variables. Therefore, the statistical analysis will only address the responses of both Ta-10%W and T-111 to low-temperature creep/stress rupture at the test temperature of 25°C.

Figure 5.5.1 graphically represents the low-temperature creep/stress rupture test results of irradiated and non-irradiated Ta-10%W samples tested at 25°C with a load of 690 MPa. As can be seen from the plots, there are differences in the response of rupture time, elongation at rupture and steady state creep rate between the irradiated and non-irradiated Ta-10%W specimens. In general at

his load, the differences in the low-temperature/stress rupture behavior between irradiated and non-irradiated Ta-10%W are manifested in an approximate; two-order of magnitude increase in rupture time, a 21% reduction in elongation at rupture, and a two-order of magnitude reduction in steady state creep rate.

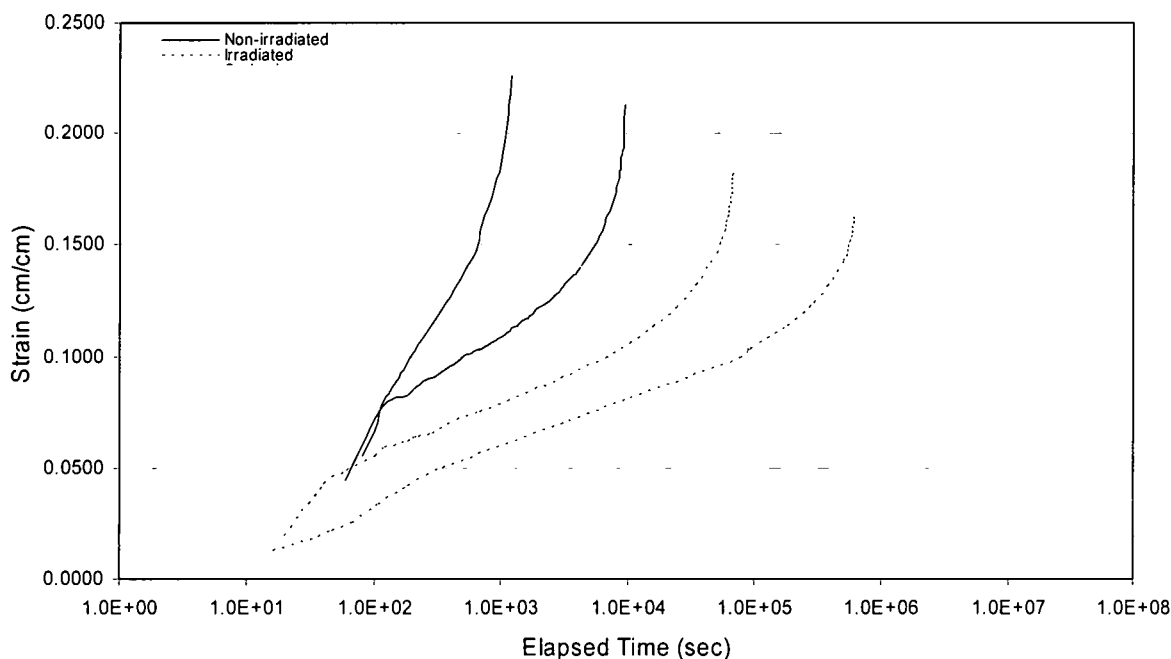


Figure 5.5.1. Creep/stress rupture test results of irradiated (8B/10A) and non-irradiated (5A/5B) Ta-10%W samples tested at 25°C with a load of 100 ksi.

Figure 5.5.2 graphically represents the low-temperature creep/stress rupture test results of irradiated and non-irradiated T-111 samples tested at 25°C with a load of 620 MPa. In contrast to the results for Ta-10%W shown in Figure 5.5.1, the responses of rupture time, elongation at rupture and steady state creep rate for the irradiated and non-irradiated T-111 specimens are a result of a lower static load and hence are more significant. In general, the differences in the low-temperature/stress rupture behavior between irradiated and non-irradiated T-111

are manifested in an approximate: two-order of magnitude increase in rupture time, a 13% reduction in elongation at rupture, and a two-order of magnitude reduction in steady state creep rate.

It should be noted that although the differences in the low-temperature/stress rupture behavior between irradiated Ta-10%W and T-111 ostensibly appear very similar, the variations in the order of magnitude responses of rupture time and steady state creep rate are much more significant in T-111 than in Ta-10%W.

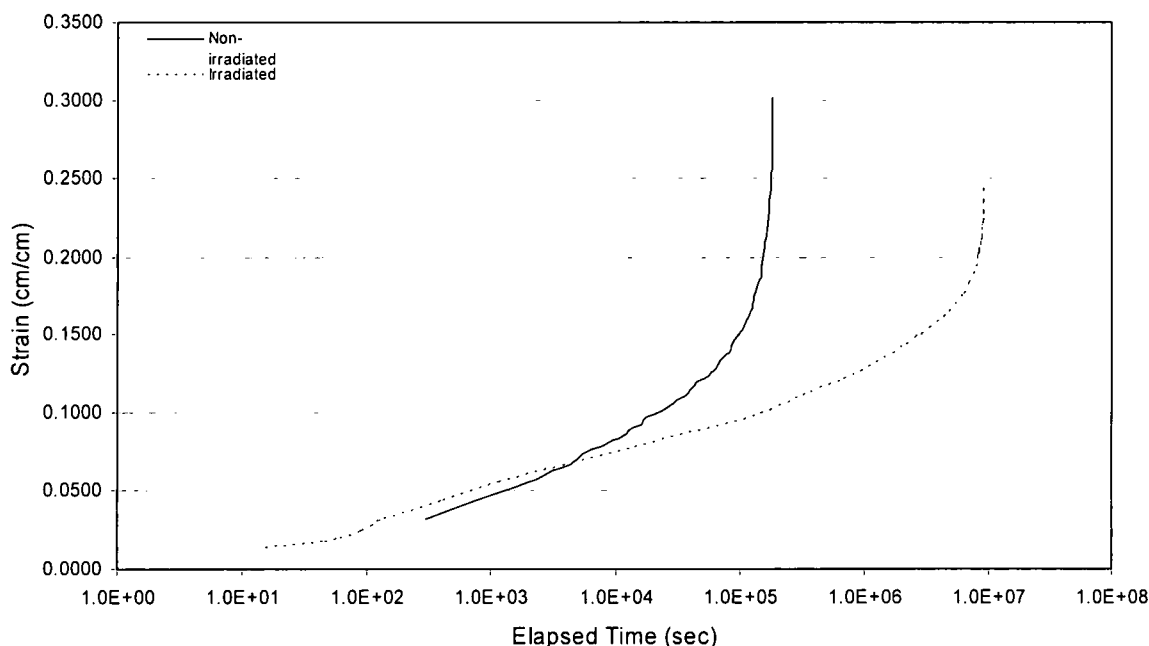


Figure 5.5.2. Creep/stress rupture test results of irradiated (T4A) and non-irradiated (T1A/T1B) T-111 samples tested at 25°C with a load of 90 ksi.

Statistical Analysis System (SAS) software⁴⁷ was used to conduct an analysis of variance (ANOVA) on over 20,000 hours of low-temperature creep/stress rupture data of irradiated and non-irradiated Ta-10%W and T-111 specimens.

Specifically, responses of rupture time, elongation and steady state creep rate were analyzed based on the dependent variables of irradiation level, irradiation temperature, and creep load and test temperature. The results of the ANOVA, shown in Appendix C, indicate statistically significant differences in the effects of:

- a) Hafnium level (i.e. difference between Ta-10%W and T-111) vs. rupture time ($p = 0.0460$);
- b) The interaction of irradiation fluence and irradiation temperature vs. rupture time ($p = 0.0472$)
- c) Creep load level vs. rupture time ($p = 0.0225$)
- d) Hafnium level (i.e. difference between Ta-10%W and T-111) vs. steady state creep rate ($p = 0.0567$);
- e) The interaction of irradiation fluence and irradiation temperature vs. steady state creep rate ($p = 0.0572$)
- f) Creep load level vs. steady state creep rate ($p = 0.0284$)

Although a significance level of $p < 0.05$ was selected as the primary indicator of a statistical difference in the responses of rupture time, elongation and steady state creep rate, the two responses noted above with a significance levels of $p = 0.0567$ and 0.0572 are considered significant.

These experimental results show that the rupture time and steady state creep rate of both Ta-10%W and T-111 tested at 25°C are affected when irradiated with

a neutron fluence of $\sim 1.2 \times 10^{15}$ nvt at both 25°C and 350°C. Additionally, the results demonstrate that the response of rupture time and steady state creep rate for T-111 are more pronounced than for Ta-10%W. Whereas the effects of research parameters associated with irradiation level, irradiation temperature, creep load and test temperature on the elongation at rupture of both alloys are not considered statistically significant.

5.6 Development of Steady-State Creep Model

Various standard analytical techniques were applied to the steady state creep data of both irradiated and non-irradiated T-111 and Ta-10%W specimens. This was preferred to gain a better insight into the creep mechanisms, and to develop a predictive model for determining the secondary creep rates for these materials in the temperature regime of 25-300°C and stress ranges and 496-690 ksi that were employed in this research.

5.6.1 Apparent Activation Energy for Creep

Although the relevance of apparent activation for creep (E_c) at temperatures less than $0.3 T_m$ is somewhat unclear, from a basic material property perspective, its determination is necessary in order to correlate the creep data with a stress function. The strain rate at a constant stress usually increases exponentially with temperature in accordance with an Arrhenius-type relationship. Thus, the apparent activation energy for creep is determined using the following formula:

$$E_c = - \Delta(\ln \dot{\epsilon}) / \Delta(1/RT) \quad [5.6.0]$$

Where, R is the ideal gas constant (8.3145 J/mole-K) and T is the testing temperature in degrees Kelvin. Apparent activations energies for creep were calculated using equation 5.6.0 and the results are presented in Figures 5.6.1 and 5.6.2. The results show a linear relationship over the ranges of temperatures investigated. The apparent activation energies for creep of

irradiated and non-irradiated T-111 and Ta-10%W are the slopes of the plots shown in Figures 5.6.1 and 5.6.2, respectively.

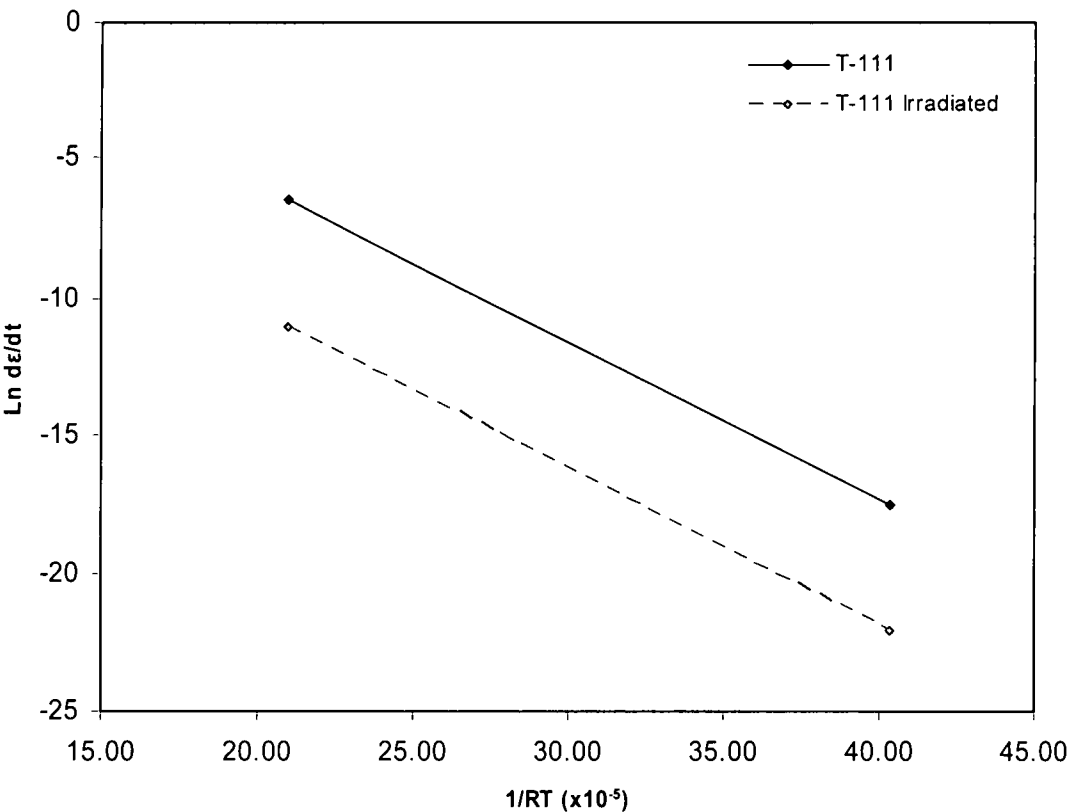


Figure 5.6.1. Determination of Apparent Activation Energy for Creep of Irradiated and Non-irradiated T-111.

The apparent activation energies for creep of irradiated and non-irradiated T-111 and Ta-10%W are shown in Table 5.6.1. Because the activation energies shown in Table 5.6.1 are so close in value it was determined that an average of 57.28 kJ/mole would be used for both materials and both radiation conditions when calculating the stress function in Section 5.6.2 and determining the minimum creep rate equations in Section 5.6.3.

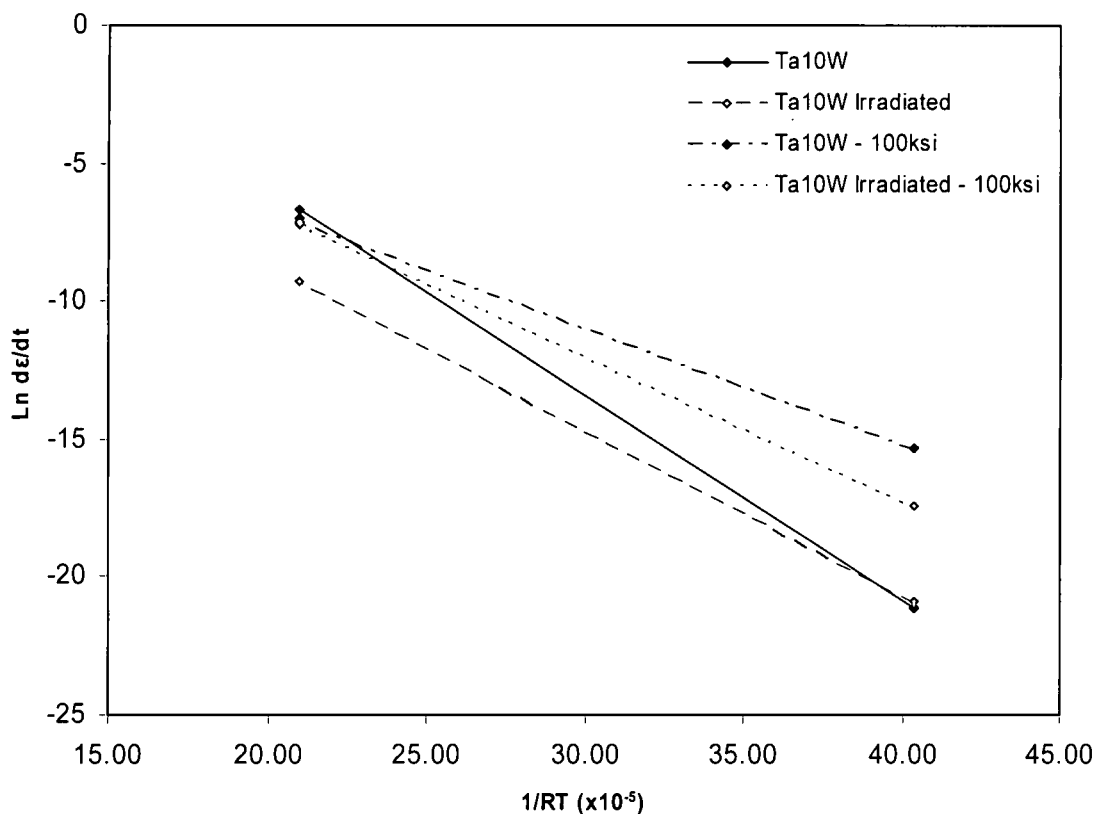


Figure 5.6.2. Determination of Apparent Activation Energy for Creep of Irradiated and Non-irradiated Ta-10%W.

Material	Irrad. Level (10 ¹⁵ nvt)	σ (MPa)	E _c (kJ/mol)
T-111	0	620	57.19
	1.20		56.98
Ta-10%W	0	620	74.75
	1.20		60.11
Ta-10%W	0	690	42.14
	1.20		52.50
			Average

Table 5.6.1. Apparent Activation Energies for Creep of Irradiated and Non-irradiated T-111 and Ta-10%W.

5.6.2 Stress Function Determination

The three primary stress functions commonly found in literature are:¹¹

1. The power law - $\dot{\epsilon} \propto \sigma^n$
2. The exponential Law - $\dot{\epsilon} \propto e^{B\sigma}$
3. The Sinh law - $\dot{\epsilon} \propto [\text{Sinh}(\alpha\sigma)]^n$

After significant analysis it was determined that the creep data associated with this research for both T-111 and Ta-10%W follow a hyperbolic sine relationship since it approximates the power law at low stresses and the exponential law at higher stresses. This is consistent with the observations of Sheffler, et al. regarding T-111.⁹ The following is the Sinh law equation:

$$\dot{\epsilon} = B [\text{Sinh}(\alpha\sigma)]^n e^{\frac{-E_c}{RT}} \quad [5.6.1]$$

Where,

B - Material dependent constant

α - Material dependent constant

n - The stress function, the slope of plots shown in figures 5.6.3 through 5.6.6

E_c - Apparent activation energy, from Table 5.6.2

R - Ideal gas constant (8.3145 J/mole-K)

T - Test temperature in Kelvin.

As stated in Section 5.6.1 it was determined that an average of 57.28 kJ/mole would be used for both materials and both radiation conditions. Additionally, the material constant term, $\alpha = 9.6 \times 10^{-3}$, was converted from the value Sheffler⁹ reported for T-111, and was used for both T-111 and Ta-10%W.

In order to calculate the stress function it is necessary to plot temperature compensated strain rate versus $[\text{Sinh } (\alpha\sigma)]^n$ for each material and condition (irradiated/non-irradiated). The slope of these plots are the stress function for the given material and condition. Once the slope of the temperature compensated strain rate versus $[\text{Sinh } (\alpha\sigma)]^n$ plots (Figures 5.63 through 5.6.6) were determined, the next step was to calculate the material dependent constant B . This was done by substituting in known parameters and strain rates into equation 5.6.1 and solving for the constant B . Table 5.6.2 outlines all the calculated variables associated with equation 5.6.1 for each material and condition.

Material	Irrad. Level (10 ¹⁵ nvt)	B	α	n
T-111	0	4.33×10^{-10}	9.6×10^{-3}	5.14
	1.2	2.15×10^{-16}	9.6×10^{-3}	7.02
Ta-10%W	0	7.40×10^{-12}	9.6×10^{-3}	5.22
	1.2	7.20×10^{-12}	9.6×10^{-3}	5.27

Table 5.6.2. Calculated variables associated with equation 5.6.1.

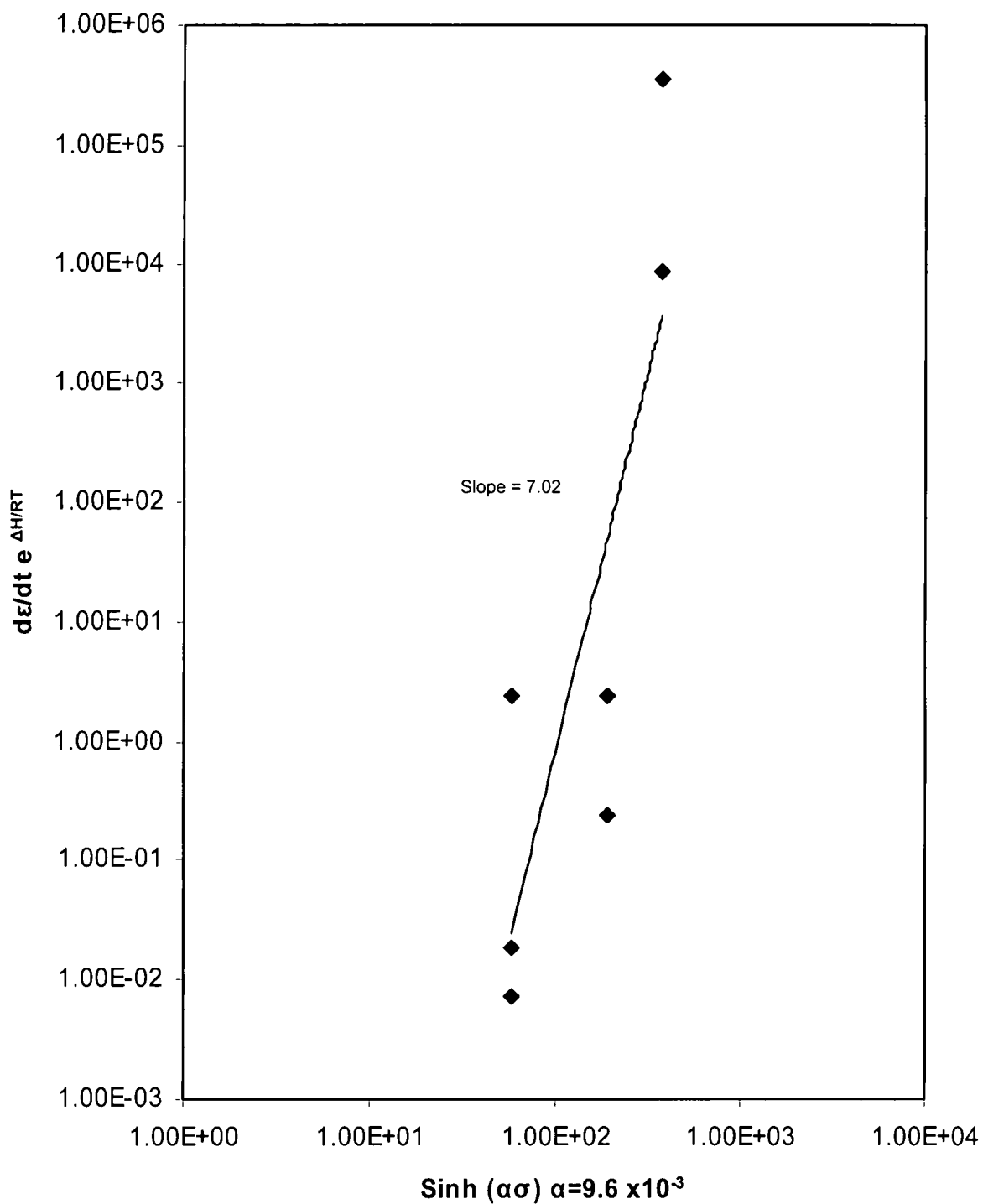


Figure 5.6.3. Variation of Temperature Compensated Strain Rate with $[\text{Sinh}(\alpha\sigma)]^n$ for Irradiated T-111.

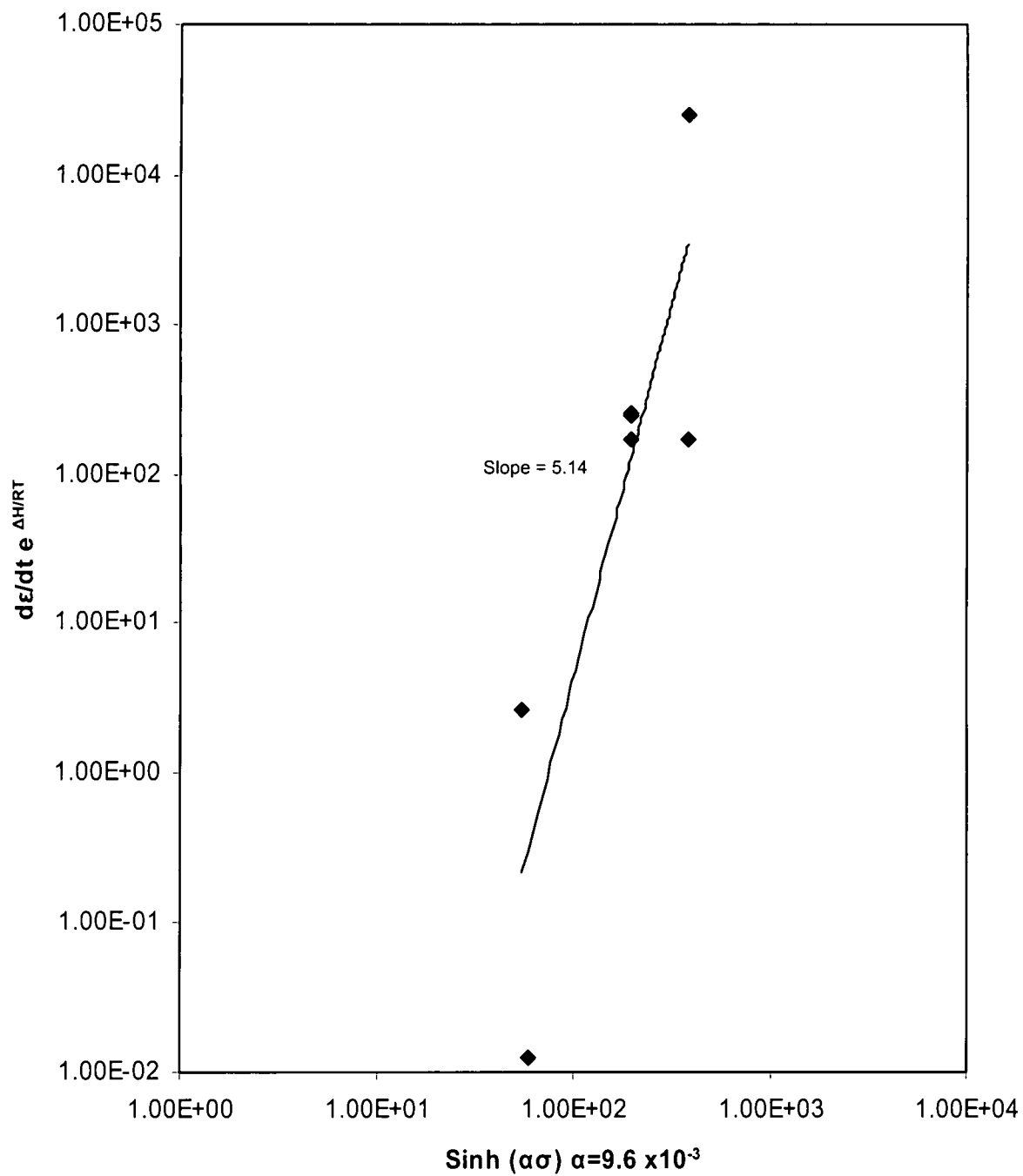


Figure 5.6.4. Variation of Temperature Compensated Strain Rate with $[\text{Sinh}(\alpha\sigma)]^n$ for Non-irradiated T-111.

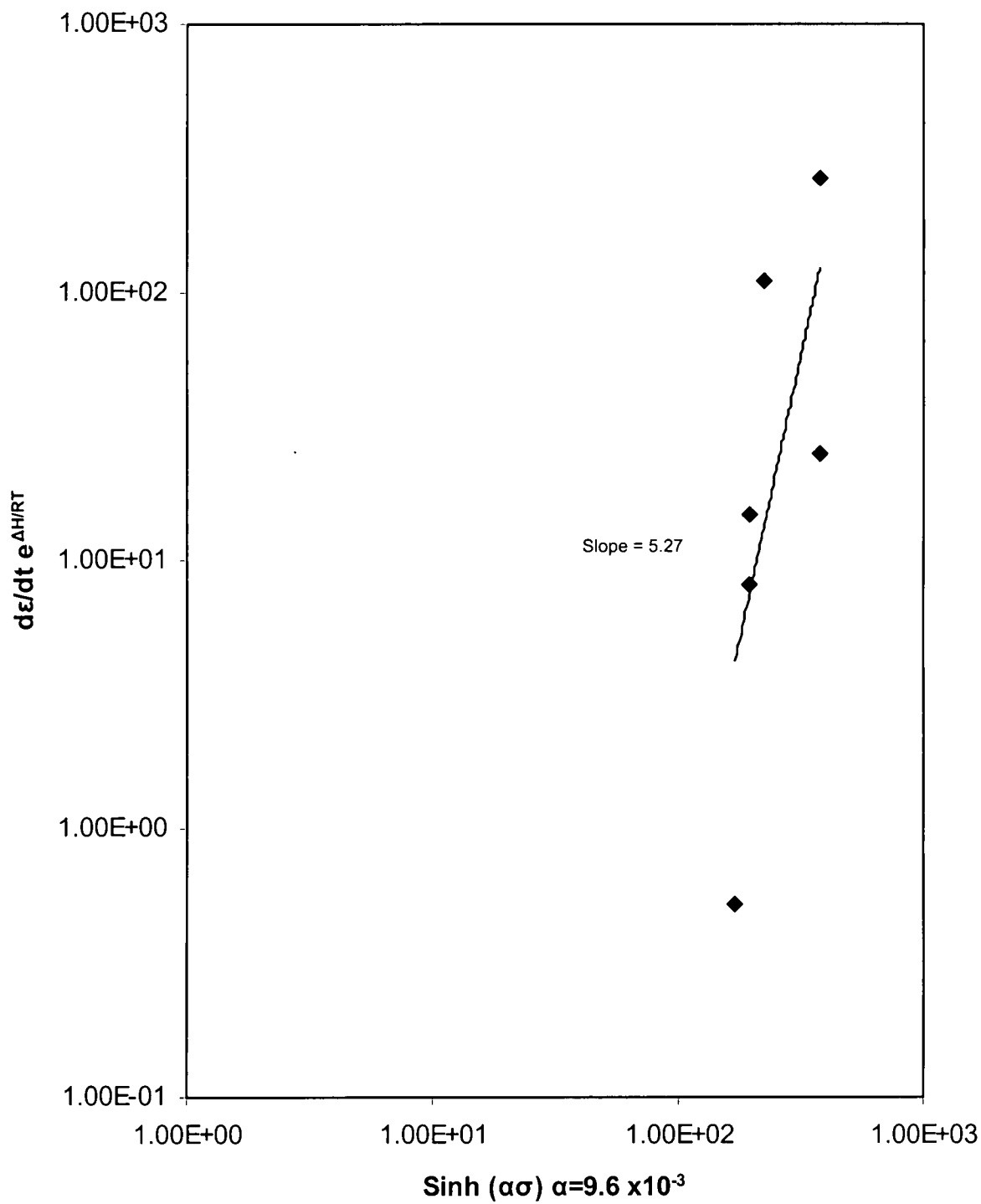


Figure 5.6.5. Variation of Temperature Compensated Strain Rate with $[\text{Sinh}(\alpha\sigma)]^n$ for Irradiated Ta-10%W.

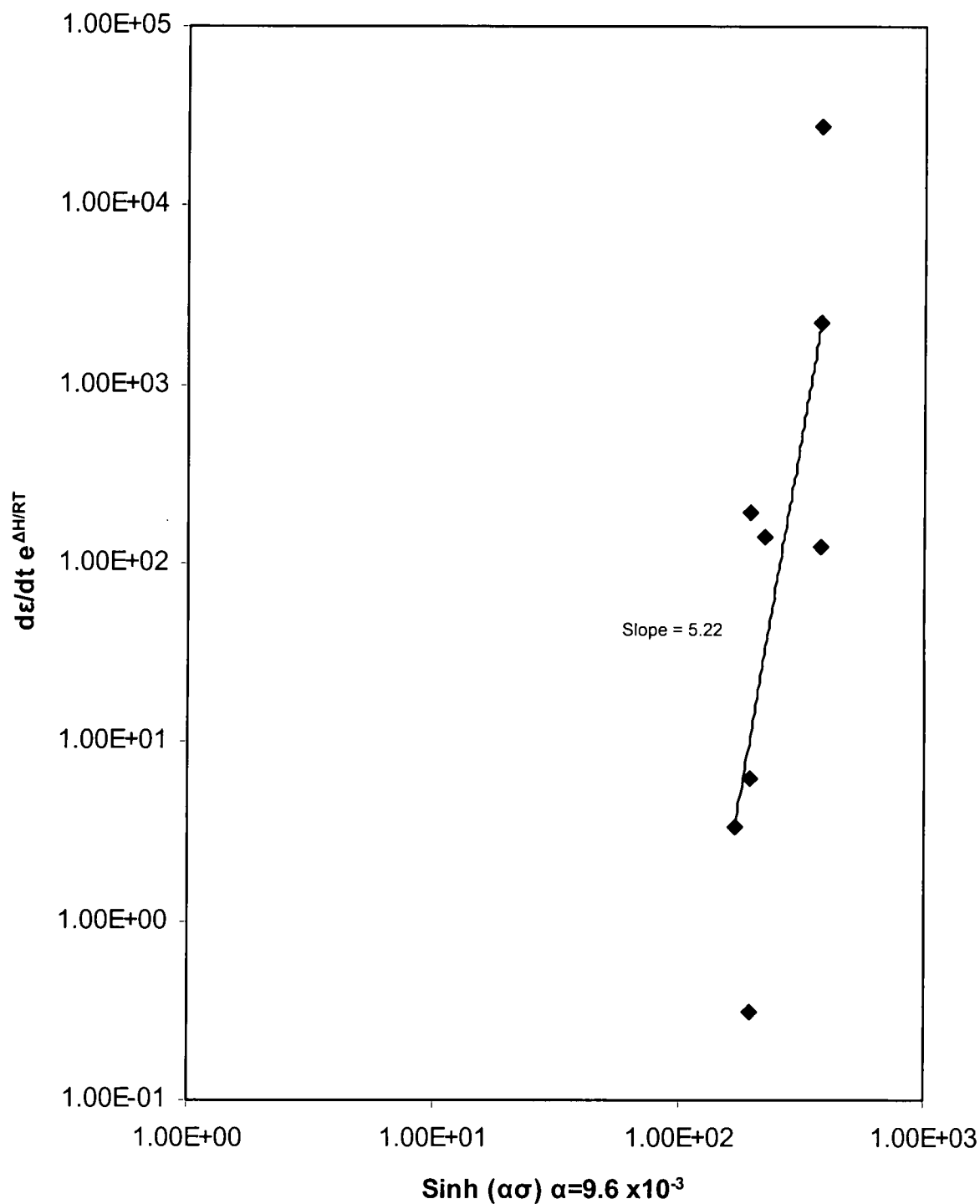


Figure 5.6.6. Variation of Temperature Compensated Strain Rate with $[\sinh(\alpha\sigma)]^n$ for Non-irradiated Ta-10%W.

5.6.3 Minimum Creep Rate Equations

As previously discussed in Section 5.6.2, for this research the hyperbolic sine relationship was used to describe the secondary creep rate for both T-111 and Ta-10%W. The following is the Sinh law equation for both alloys:

$$\dot{\epsilon} = B [\text{Sinh}(9.6 \times 10^{-3} \sigma)]^n e^{-57280/RT} \quad [5.6.1a]$$

Where,

B - Material dependent constant

n - The stress function, the slope of plots shown in figures 5.6.3 through 5.6.6

R - Ideal gas constant (8.3145 J/mole-K)

T - Test temperature in Kelvin.

Substituting in the determined stress functions (n) from Table 5.6.2 and solving for material constant B using the steady state creep data; the minimum creep rate (m/s) for both irradiated and non-irradiated T-111 and Ta-10%W can be described by the expressions:

T-111 (non-irradiated)

$$\dot{\epsilon} = 4.33 \times 10^{-10} [\text{Sinh}(9.6 \times 10^{-3} \sigma)]^{5.14} e^{-57280/RT} \quad [5.6.2]$$

T-111 (Irradiated)

$$\dot{\epsilon} = 2.16 \times 10^{-16} [\text{Sinh}(9.6 \times 10^{-3} \sigma)]^{7.02} e^{-57280/RT} \quad [5.6.3]$$

Ta-10%W (Irradiated and non-irradiated)

$$\dot{\epsilon} = 7.30 \times 10^{-12} [\text{Sinh}(9.6 \times 10^{-3} \sigma)]^{5.25} e^{-57280/RT} \quad [5.6.4]$$

for temperatures from 25 to 300°C and stresses between 496 to 690 MPa.

5.6.4 Correlation of Minimum Creep Rate and Radiation Damage

The next step is to correlate the minimum creep rate equations 5.6.2 through 5.6.4 with the radiation damage calculated in Section 5.3.2 for both Ta-10%W and T-111.

The analysis determined that the minimum creep rate equations for Ta-10%W do not show any significant difference due to the neutron irradiation exposures associated with this research. It is reasonable to hypothesize that the applied neutron irradiation threshold damage necessary to produce sufficient changes to the mechanical properties of Ta-10%W, thereby increasing the stress function, was not achieved at the fluence level of 1.2×10^{15} nvt. Therefore, no correlation was determined between radiation damage and the minimum creep rate equation 5.6.4 for Ta-10%W.

However, a correlation between radiation damage and minimum creep rate equation 5.6.3 can be established for T-111. As determined in Section 5.3.2, the approximate atomic displacement damage, described quantitatively by the number of displacements per atoms (dpa) over a certain period of time, for both T-111 and Ta-10%W irradiated test specimens is approximately 3.0×10^{-7} dpa. Therefore, the following mathematical relationship between the stress function and radiation damage is established:

$$n \propto \beta e^{1+\phi(dpa)}$$

Where,

n - The stress function

β - Derived constant

φ - Derived constant

dpa - Approximate atomic displacement damage

Using the stress functions derived for equations 5.6.2 and 5.6.3 and solving for the two constants β and φ the following equation is derived for the stress function:

$$n = 1.8910e^{1+dpa(1.04 \times 10^6)} \quad [5.6.5]$$

which is valid in the temperature and stress ranges of 25 to 300°C, 496 to 690 MPa for neutron damage levels between 10^{-7} to 10^{-6} dpa for T-111.

Therefore, the minimum creep rate (m/s) for irradiated T-111 can be described by the expression:

$$\dot{\epsilon} = (dpa) 4.33 \times 10^{-10} [\sinh(9.6 \times 10^{-3} \sigma)]^{1.8910e^{1+dpa(1.04 \times 10^6)}} e^{-57280/RT} \quad [5.6.6]$$

for temperatures from 25 to 300°C, stresses between 496 to 690 MPa, and for a neutron damage levels between 10^{-7} to 10^{-6} dpa for T-111.

5.6.5 Discussion

At the temperature and stress levels used in this research, the data reveals that the low temperature creep resistance of both alloys is sensitive to irradiation fluence. This effect is more pronounced in T-111 than in Ta-10%W. Additionally, the neutron irradiated T-111 specimens exhibited a two-order of magnitude decrease in the minimum steady state creep rate and a minor reduction in rupture strain at 25°C.

The values of the stress functions in equations 5.6.2 through 5.6.4 suggest that rate controlling mechanism for steady state creep of these materials is dislocation glide. The increase in stress function from 5.14 to 7.02 for irradiated T-111 specimens further reinforces the conclusion that the fluence levels associated with this research have a pronounced effect on non-conservative dislocation motion for T-111. Additionally, the lack of change in the stress function between the irradiated and non-irradiated Ta-10%W specimens show that within the parameters of this research that neutron irradiation has a negligible effect on the creep properties of Ta-10%W.

5.7 Scanning Electron Microscope Fractography

In this section, the fracture surface characteristics of the Ta-10%W and T-111 creep specimens tested in this research and some of the mechanisms associated with the fracture modes will be presented. The discussion of mechanisms in this section will not include detailed dislocation models or complex mathematical treatment, because these will be addressed in the following sections. However, the discussion in this section will present the mechanisms in more general terms in order to gain a basic understanding of the basic fracture modes.

In general, the SEM images, shown in Figures 5.7.1 through 5.7.4, taken of the fracture surfaces of the stress rupture tested specimens of irradiated and non-irradiated Ta-10%W and T-111 exhibit a ductile failure mode based on the dimples observed throughout the fracture surfaces. All of the fracture surfaces are considerably rough and exhibit elongated dimples of various sizes with relatively flat regions in between. Such features are indicative of ductile failure mechanisms associated with uniaxial tests.⁴⁸

When an alloy is subjected to mechanical overload, it may fail by a process called microvoid coalescence, which is the result of complex slip. Voids nucleate at regions of localized strain discontinuity, mostly associated with second phase particles, inclusions, grain boundaries and dislocation pile-ups.⁴⁹ With increasing

strain, the microvoids grow, coalesce and eventually form a continuous fracture surface, which is characterized by numerous cuplike depressions, also referred to as dimples.⁴⁹ The failure mode of all creep specimens associated with this research can be classified as transgranular microvoid coalescence.

What can be consistently observed between irradiated and non-irradiated specimens of both Ta-10%W and T-111 is the emergence of a bimodal distribution of the mean dimple size of both irradiated alloys when compared with their non-irradiated counterparts.

5.7.1 Fractography of Ta-10%W

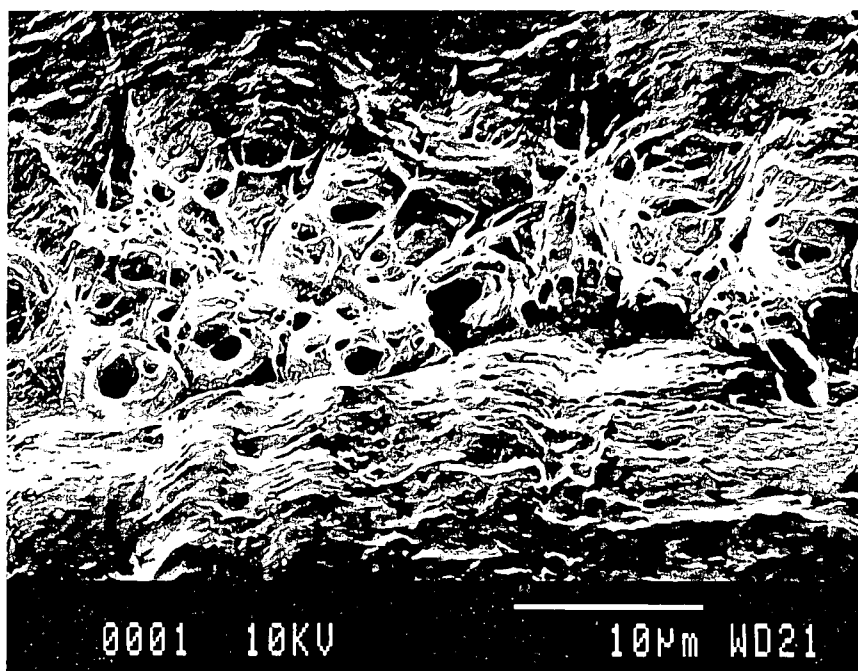


Figure 5.7.1. SEM photomicrograph of fracture surface of a rupture tested non-irradiated Ta-10%W sample (5C).

As seen in Figure 5.7.1 the fracture surface of non-irradiated Ta-10%W has a fairly narrow dimple size distribution, 2 µm maximum estimated diameter. This

type of uniform fracture surface is characteristic of a ductile material. The photomicrograph in Figure 5.7.2 shows the fracture surface of irradiated Ta-10%W. The micrograph shows a bimodal distribution of small and large dimples on the fracture surface and evidence of poorly defined cleavage facets connected by deeply indented dimples. The estimated mean dimple diameters are 2 μm and 7 μm .

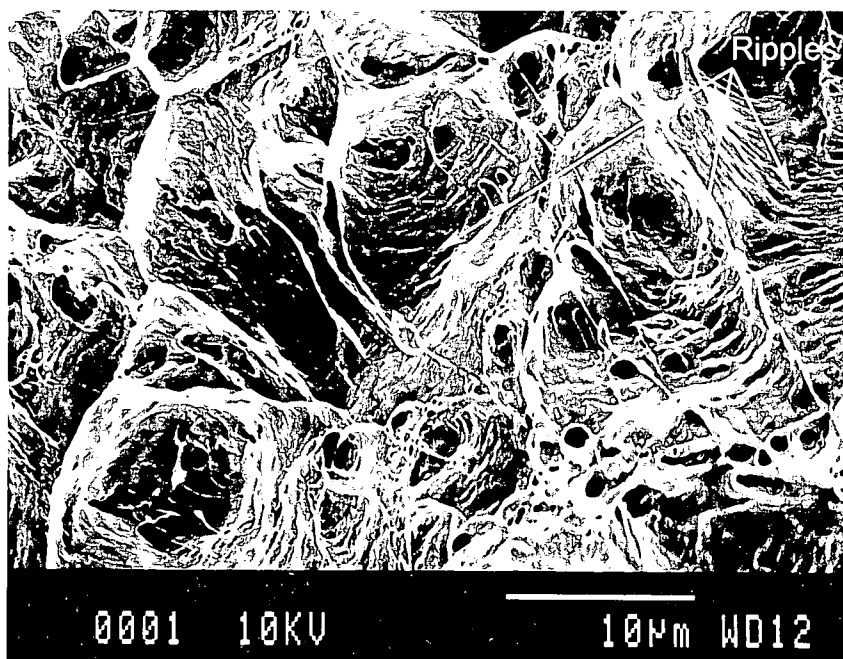


Figure 5.7.2. SEM photomicrograph of fracture surface of a rupture tested non-irradiated Ta-10%W sample (8C).

5.7.2 Fractography of T-111

Similar to Ta-10%W the non-irradiated T-111 rupture tested sample shown in Figure 5.7.3 has a fairly narrow dimple size distribution, 3 μm estimated mean diameter, which is also characteristic of a ductile failure mode. The photomicrograph in Figure 5.7.4 shows the fracture surface of irradiated T-111. The micrograph shows a bimodal distribution of small and large dimples on the

fracture surface and evidence of poorly defined cleavage facets connected by deeply indented dimples. The estimated mean dimple diameters are $<1\text{ }\mu\text{m}$ and $7\text{ }\mu\text{m}$.

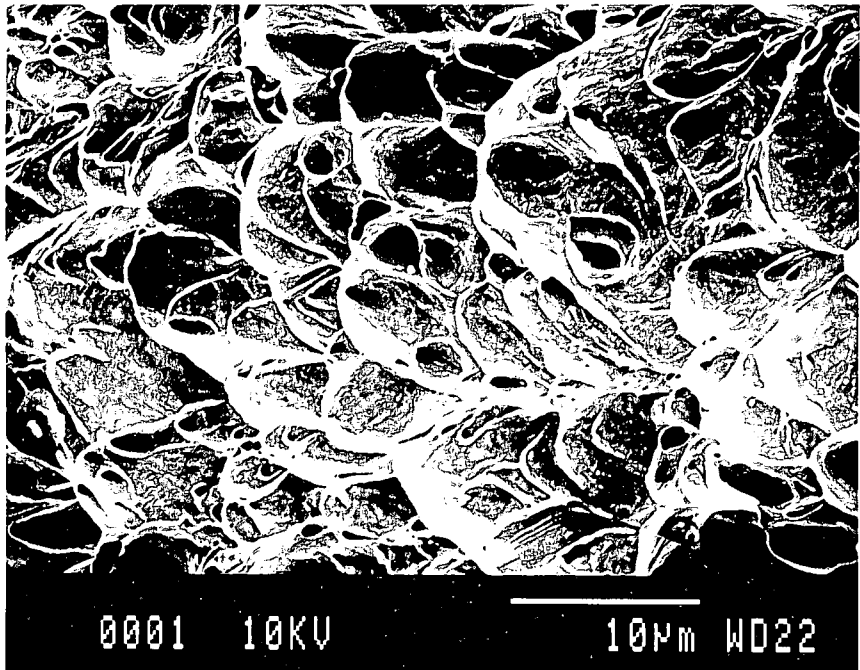


Figure 5.7.3. SEM photomicrograph of fracture surface of a rupture tested non-irradiated T-111 sample (T1C).

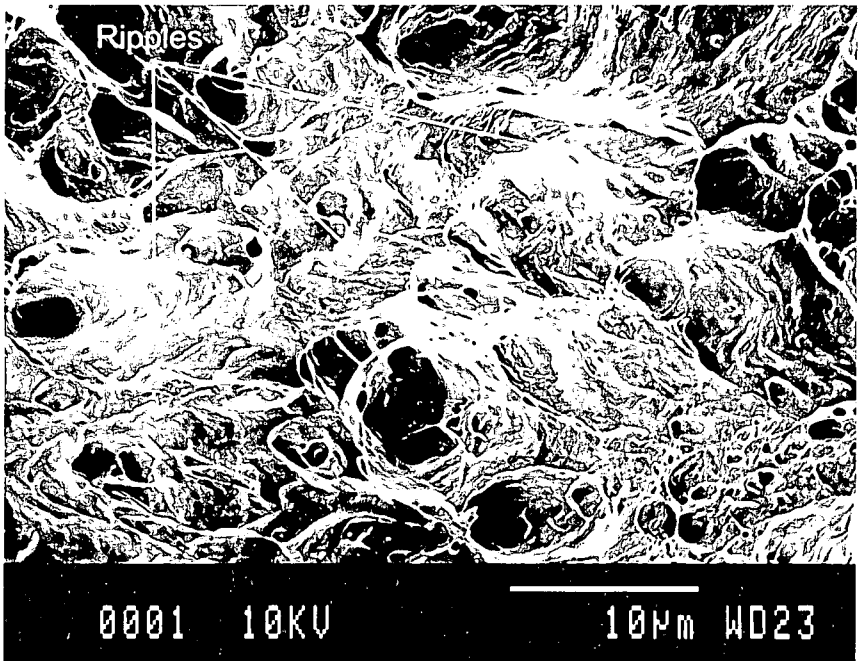


Figure 5.7.4. SEM photomicrograph of fracture surface of a rupture tested irradiated T-111 sample (T4C).

5.7.3 Discussion

The fracture surfaces of the irradiated alloys, which exhibit a statistical difference in elongation in T-111 (Section 5.4) and dramatic increase in rupture time (Section 5.5), clearly exhibit a more planar aspect with shallower dimples and poorly defined cleavage facets, when compared to their non-irradiated counterparts. This is indicative of materials that have experienced a loss of ductility.⁴⁸

It can also be seen that qualitative differences between the irradiated and non-irradiated fracture surfaces are more pronounced in T-111 than in Ta-10%W. Although the fracture surface of the irradiated and non-irradiated samples are different, the failure mode of all samples are essentially transgranular and ductile. The fracture surface of the irradiated creep test specimens shown in Figures 5.7.2 and 5.7.4 exhibit various dimple sizes. This variation in dimple size results from a non-uniform distribution of nucleating particles and the nucleation and growth of isolated microvoids early in the loading cycle,⁴⁸ which is a function of the interaction between dislocations and small defect clusters, produced by low temperature neutron irradiation. This will be discussed in detail in Section 5.8.4.

Another interesting observation regarding the irradiated fracture surfaces shown in Figures 5.7.2 and 5.7.4 is that deformation markings are visible on the dimple walls of both fractographs. These markings occur when slip-planes at the surface of the dimples are favorably oriented to the major stress direction and result in

slip-plane displacement at the surface of the dimple as deformation proceeds.⁴⁸ This suggests that transgranular fracture occurred by ductile rupture along coarse slip bands with ductile tearing between slip band fractures. This is another indication of a reduction of ductility in the irradiated samples due to the interaction between dislocations and small defect clusters, produced by low temperature neutron irradiation. Figure 5.7.5 schematically shows this phenomenon.

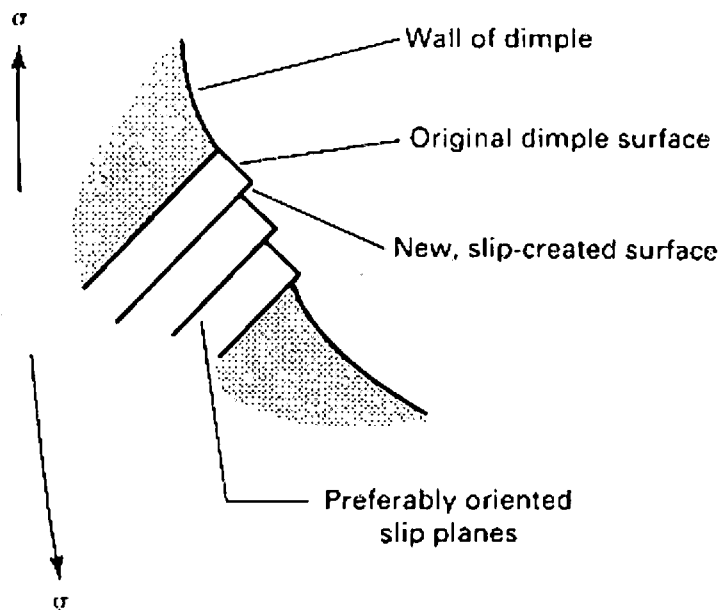


Figure 5.7.5. Slip step formation resulting in serpentine glide and ripples on a dimple wall.⁴⁸

5.8 Transmission Electron Microscopy

5.8.1 Microstructural Analysis of T-111

Transmission electron microscopy is a vital tool because it enables the simultaneous examination of microstructural features through high resolution imaging and the acquisition of chemical and crystallographic information from submicron regions of the specimens.⁴⁸ This information coupled with SEM and mechanical test data provides key information about deformation mechanisms.

Figure 5.8.1 is a TEM image of virgin recrystallized T-111 showing a dislocation density of $\sim 10^{10} \text{ m}^{-2}$. (See Section 5.8.3 for dislocation density determination).

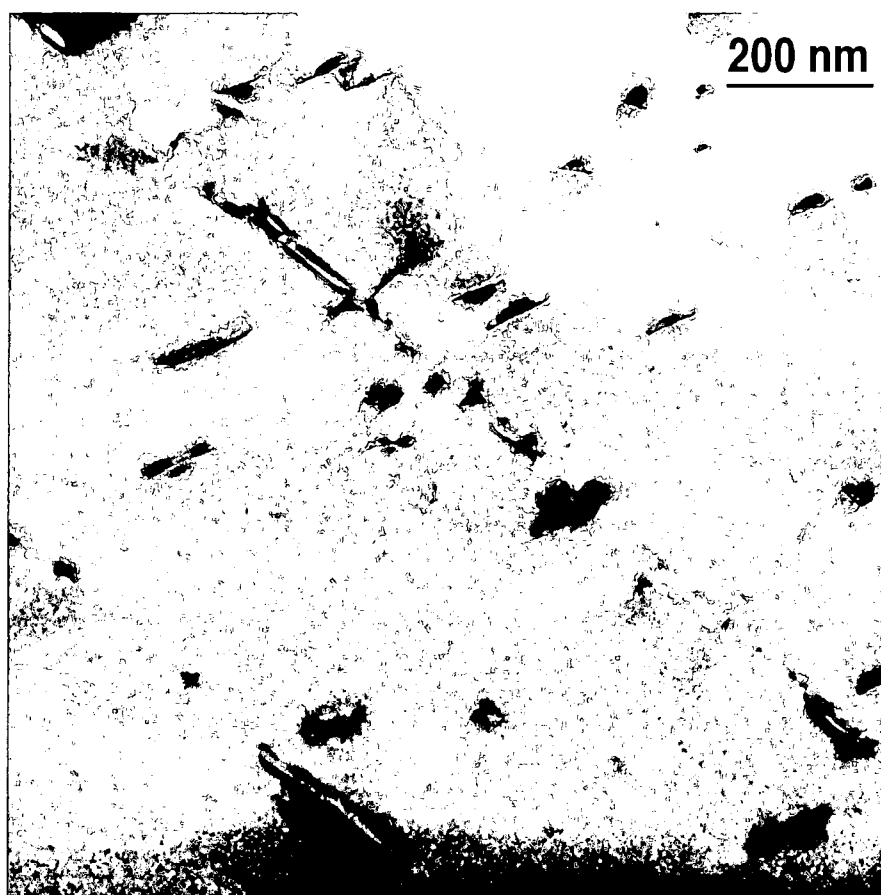


Figure 5.8.1. Bright field TEM image of recrystallized T-111.

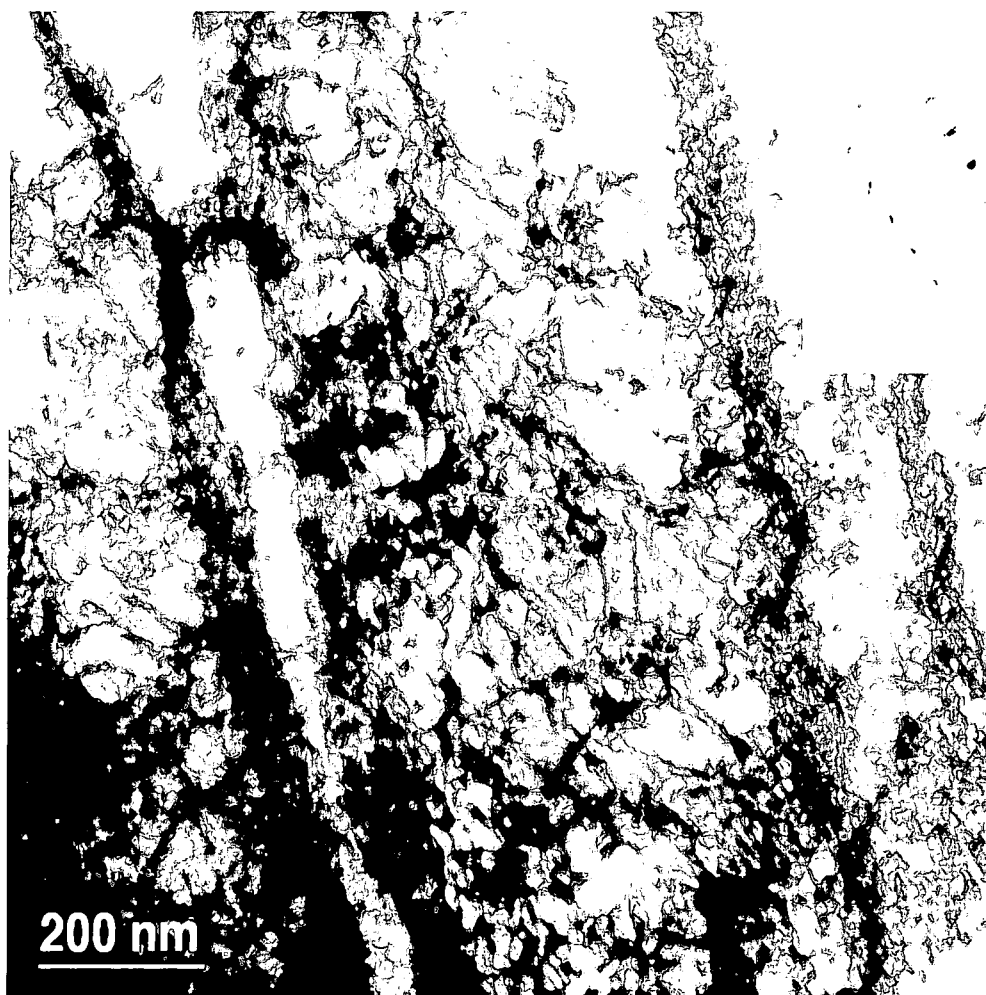


Figure 5.8.2. Bright field TEM image and electron diffraction pattern of a rupture tested non-irradiated T-111 sample.

Figure 5.8.2 is a bright field TEM image and its corresponding electron diffraction pattern of a rupture tested non-irradiated T-111 sample. Figure 5.8.2 reveals that the dislocation activity in this T-111 specimen becomes apparent through the formation of characteristic cellular or subgranular patterns, where dislocations arrange in walls at the boundaries of cells/subgrains with relatively low internal dislocation density. The dislocation density of Figure 5.8.2 is $\sim 10^{16} \text{ m}^{-2}$. Based

on the analysis of the diffraction pattern, this image was taken under a [112] zone-axis condition.

Figure 5.8.3 is a reference [112] zone-axis diffraction pattern⁵⁰ and stereogram centered on [112]. If properly oriented with Figure 5.8.2 the stereogram reveals that the cellular or subgranular patterns are oriented along the {110} family of planes. Wither⁵¹ established that a relationship exists between dislocation boundaries and slip planes. This relationship arises because slip planes and/or slip directions are roughly parallel to the macroscopically most stressed planes. This is scientifically significant because the dislocation densities and the predominate orientation of subgranular patterns, of T-111 and Ta-10%W used in this research, can be roughly correlated with their relative deformation behaviors and mechanisms.

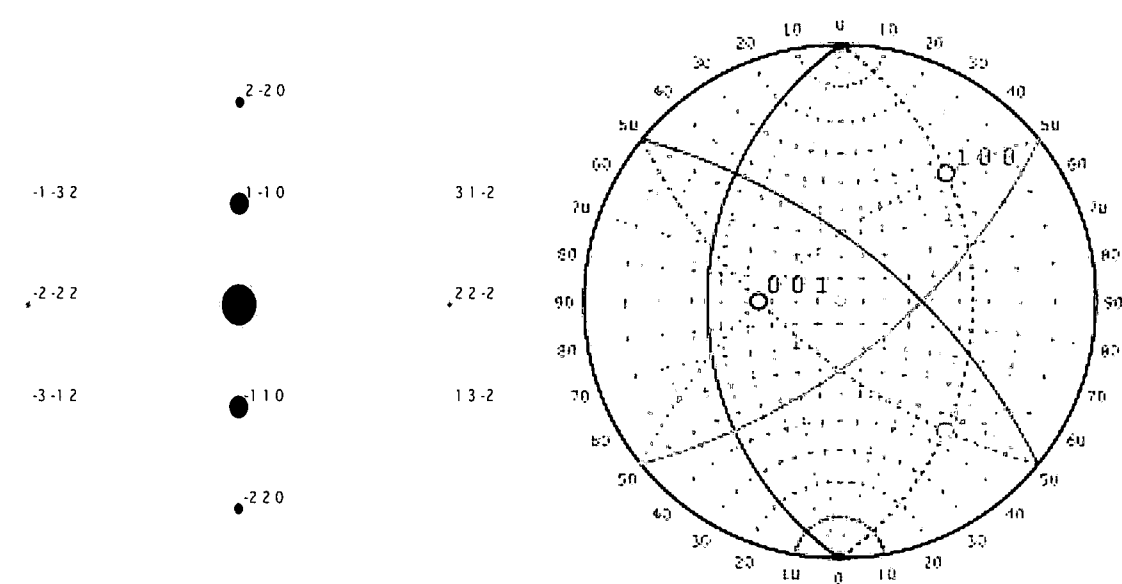


Figure 5.8.3. Reference [112] zone-axis diffraction pattern and stereogram centered on [112].

Figure 5.8.4 is a bright field TEM image of a rupture tested irradiated T-111 specimen also taken under a [112] zone-axis condition. This image shows a dislocation density in the irradiated T-111 rupture tested specimen of approximately $5.0 \times 10^{16} \text{ m}^{-2}$. In comparison to the non-irradiated T-111 rupture tested specimen shown in Figure 5.8.2, this increase in dislocation density is also accompanied by a pronounced mosaic of cells/subgrains. Similar to Figure 5.8.2, the mosaic of cells/subgrains of Figure 5.8.4 are oriented along {110} family of planes. The cells/subgrains oriented $\sim 60^\circ$ to the primary orientation of cells/subgrains appear to be on the $(\bar{1}10)$ plane.

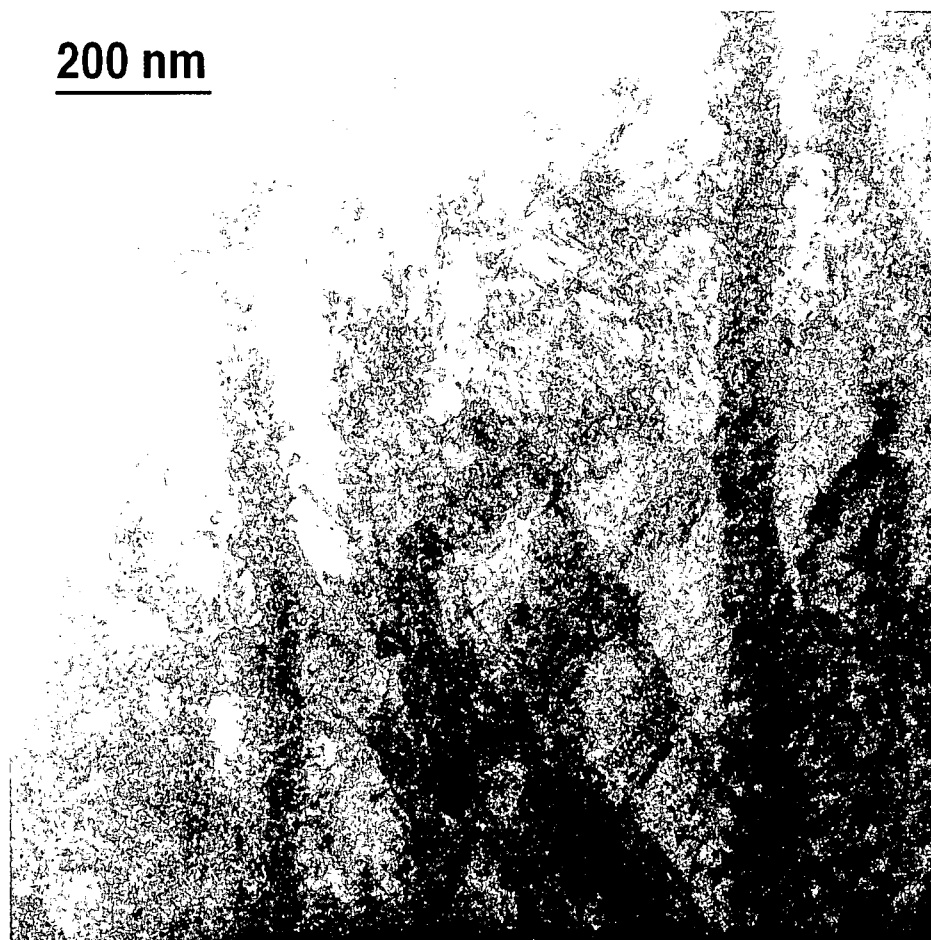


Figure 5.8.4. Bright field TEM image of a rupture tested irradiated T-111 sample.

5.8.2 Microstructural Analysis of Ta-10%W

Figure 5.8.5 is a TEM image of a virgin recrystallized non-irradiated Ta-10%W showing a dislocation density of $\sim 10^{10} \text{ m}^{-2}$.

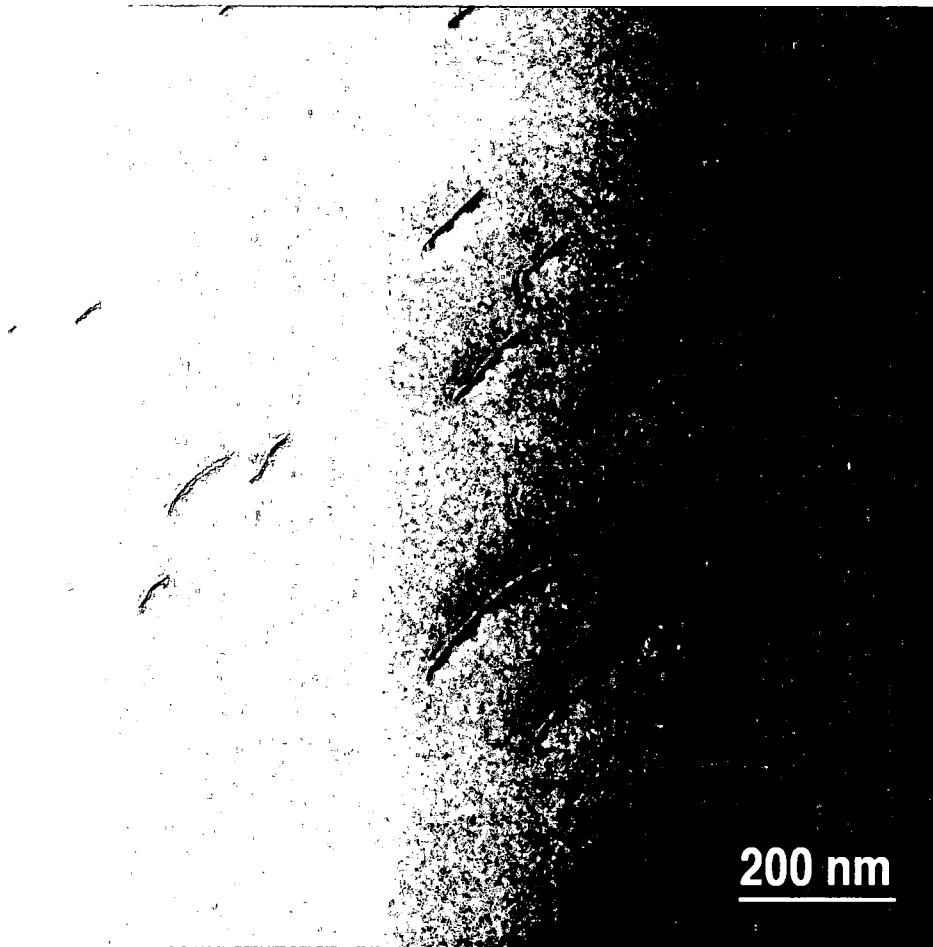


Figure 5.8.5. Bright field TEM image of recrystallized Ta-10%W.

Figure 5.8.6 is a bright field TEM image of a rupture tested non-irradiated Ta-10%W sample. Figure 5.8.6 reveals that the dislocation activity in creep/tensile tested Ta-10%W becomes apparent through the formation of characteristic cellular or subgranular patterns where dislocations arrange in walls at the boundaries of cells/subgrains with a low internal dislocation density. The

dislocation density of Figure 5.8.6 is approximately 10^{15} m^{-2} , which is an order of magnitude less than the T-111 sample shown in Figure 5.8.2.

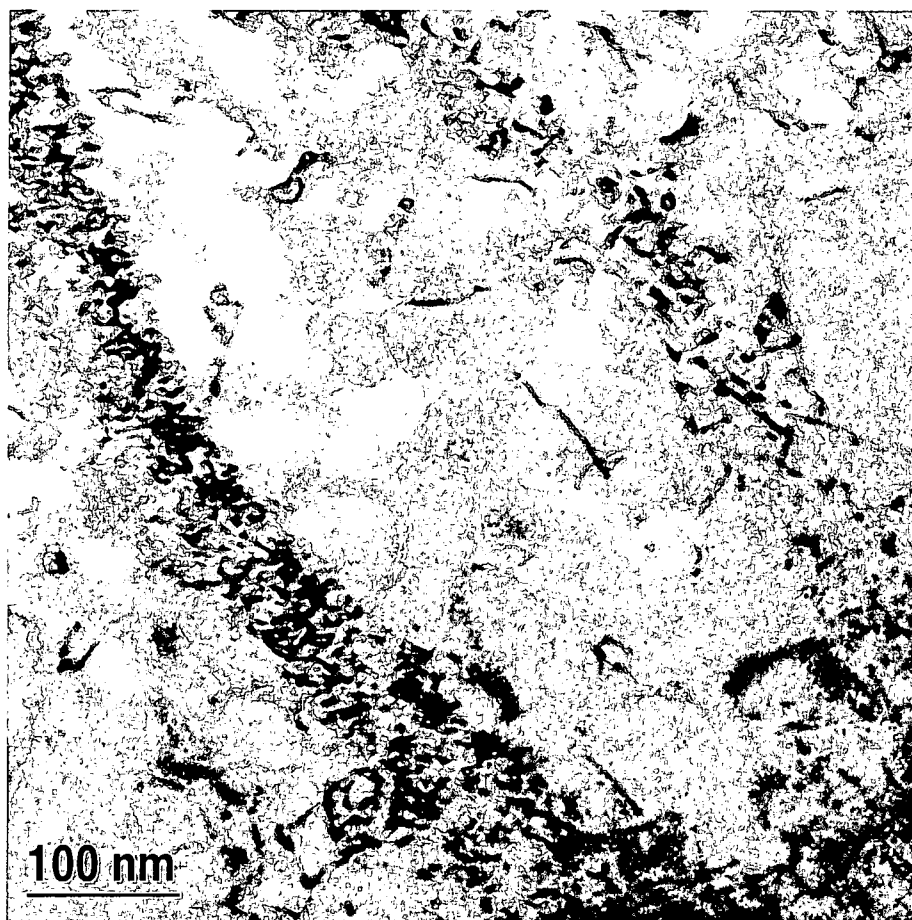


Figure 5.8.6. Bright field TEM image of a rupture tested non-irradiated Ta-10%W sample.

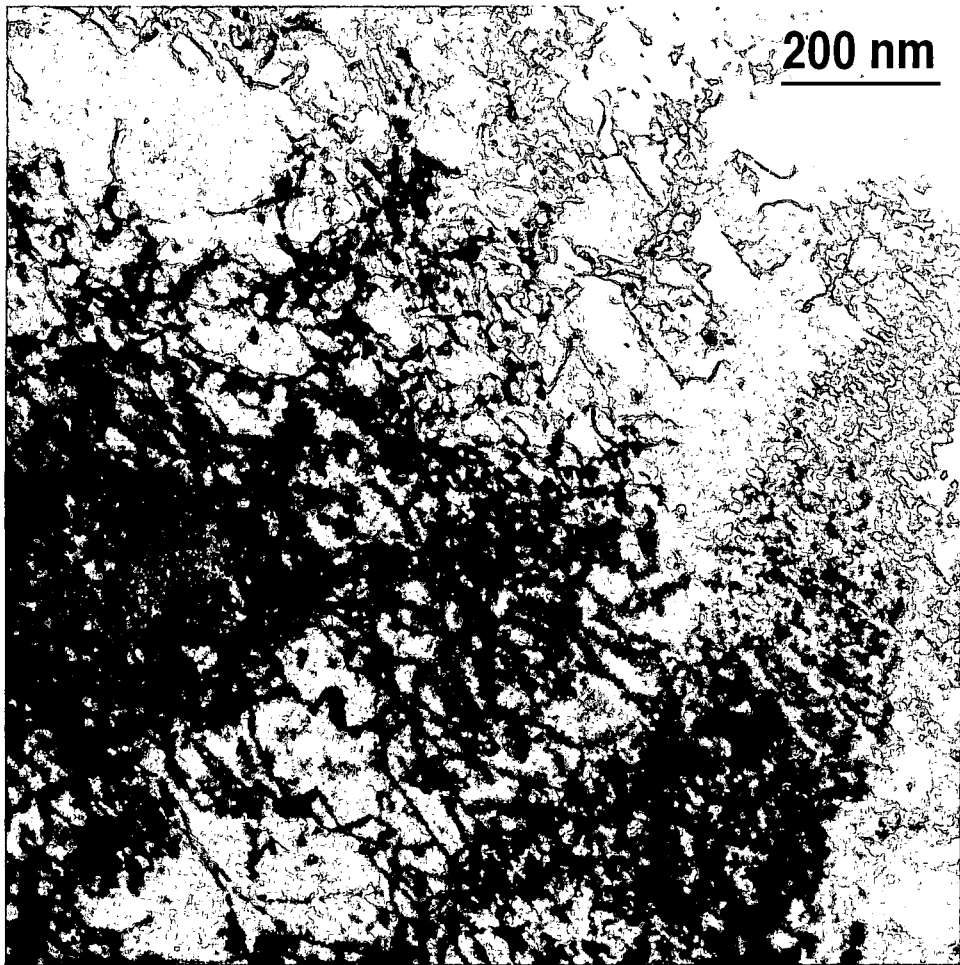


Figure 5.8.7. Bright field TEM image of a rupture tested irradiated Ta-10%W sample.

Figure 5.8.7 is a bright field TEM image that shows a dislocation density in the irradiated Ta-10%W rupture tested specimen of approximately 10^{16} m^{-2} . In comparison to the non-irradiated Ta-10%W rupture tested specimen shown in Figure 5.8.6, this increase in dislocation density is not accompanied by a pronounced mosaic of cells/subgrains, which is in contrast to the irradiated rupture tested T-111 specimen shown in Figure 5.8.4.

5.8.3 Dislocation Density Discussion

Dislocation density is a measure of how many dislocations are present in a quantity of a material. Since a dislocation is a line defect, this is defined as the total length of dislocations per unit volume. Consequently the units are $\text{m}/\text{m}^3 = \text{m}^{-2}$. Equivalently, it is the number of dislocation lines intersecting a unit area. Dislocation density is usually of the order of 10^{10} m^{-2} in a metal, increasing to $\sim 10^{15} \text{ m}^{-2}$ after work hardening. Table 5.8.1 summarizes the dislocation density results associated with this research.

Material/Condition	Recrystallized (m^{-2})	Rupture Tested (Non-Irradiated) (m^{-2})	Rupture Tested (Irradiated) (m^{-2})
T-111	1.04×10^{10}	$\sim 10^{16}$	$\sim 5.0 \times 10^{16}$
Ta-10%W	1.04×10^{10}	$\sim 10^{15}$	$\sim 10^{16}$

Table 5.8.1. Dislocation density (m^{-2}) of T-111 and Ta-10%W in varying conditions.

The TEM investigation of the defect structure of mechanically tested irradiated and non-irradiated Ta-10%W and T-111 specimens primarily focused on discerning qualitative and quantitative differences between the defect structures of sample foils. This was primarily conducted by concentrating on changes in the dislocation arrangements and density as a function of irradiation in order to validate a correlation between the dislocation structures and mechanical test data. It should be noted that TEM observations of thin foils result usually in an underestimation of dislocation density. This is because the image contrast of

dislocations as viewed with a TEM is usually non-uniform over a large area because of the changing contour of the specimen, resulting in some dislocations effectively becoming invisible. Therefore, to obtain a more precise determination of dislocation density, images must be obtained at different diffraction conditions.⁵² Unfortunately, the HF-2000 FEG TEM does not provide sufficient tilt capabilities to observe dislocations at multiple zone-axis and diffraction conditions. To mitigate this limitation the dislocation densities associated with this research were obtained from approximately 15 TEM images, on one zone-axis, for each condition.

Respective of the two alloys, the defect density and arrangement structures of the non-irradiated samples are very similar. As shown in Figure 5.8.1 for T-111 and Figure 5.8.5 for Ta-10%W the microstructures of the recrystallized alloys are relatively free of dislocations. Based on the examination of fifteen areas for each alloy an average dislocation density of $1.04 \times 10^{10} \text{ m}^{-2}$ was determined.

TEM examination of failed non-irradiated specimens of both alloys exhibited very high density cellular or subgranular patterns of dislocations coupled with adjacent areas relatively devoid of dislocations. This observation was fairly consistent throughout the sample areas observed for both non-irradiated alloys. One can see that the microstructures of the samples look similar. However, there is approximately an order of magnitude difference in the measured dislocation density between non-irradiated T-111 and Ta-10%W as shown in Figures 5.8.2

and 5.8.6, respectively. Based on the examination of fifteen areas for each material an approximate dislocation density of 10^{16} m^{-2} and 10^{15} m^{-2} were determined for non-irradiated T-111 and Ta-10%W, respectively.

As shown in Figure 5.8.4, the TEM examination of the irradiated T-111 ruptured specimen showed an increase in dislocation density, compared to its non-irradiated counterpart, accompanied by a pronounced mosaic of cells/subgrains. Whereas, the irradiated Ta-10%W ruptured specimen shown in Figure 5.8.7 reveals a slight increase in dislocation density compared to its non-irradiated counterpart, but does not exhibit a pronounced mosaic of cells/subgrains similar to the irradiated T-111 specimen. Based on the examination of fifteen areas for each material an approximate dislocation density of $1.0 \times 10^{16} \text{ m}^{-2}$ and $5.0 \times 10^{16} \text{ m}^{-2}$ were determined for irradiated T-111 and Ta-10%W, respectively.

5.8.4 Evolution of Dislocation Structure

The evolution of the dislocation structure of Ta-10%W and T-111 subjected to low-dose ($\sim 10^{-7}$ dpa) neutron irradiation then mechanically tested was examined using transmission electron microscopy (TEM). Although the irradiation induced defect structures in both materials were not observable using conventional TEM techniques their results in mechanically tested microstructures are evident.

When fcc and bcc materials are subjected to irradiation with energetic particles (neutrons or protons), internal damage ensues. The effects of neutron dose rate

and temperature are believed to conform to the dislocation pinning theory of Granato and Lücke in that the rate at which dislocations are pinned is directly proportional to neutron dose rate.⁵³ When irradiated, metals undergo significant internal damage accumulation and results in a degradation of mechanical properties, which manifests in a hardening behavior. This irradiation-induced hardening is interpreted in terms of two contributing effects: a) an extensive pinning of screw dislocations; and b) a direct bulk effect due to interstitials and clusters produced by thermal neutrons.

The primary and latent slip systems in tantalum are $\langle 111 \rangle \{110\}$ and $\langle 111 \rangle \{112\}$ respectively. Plastic flow of all bcc metals is controlled by $a_0/2 \langle 111 \rangle$ screw dislocations that possess a high Peierls stress, which leads to a strong temperature dependence of the flow stress at low temperatures. Yang and Moriarty⁵⁴ noted that for tantalum at low temperatures ($<0.3 T_m$), the motion of the screw dislocations is believed to be associated with the formation of mobile kinks on the dislocation line. When moving under the influence of the applied stress, screw dislocations will intersect thus leading to the formation of jogs. The dragging of these jogs by the moving dislocations results in the formation of intrinsic atomic defects, in particular of self-interstitials.⁵⁵ At the low temperature regimes used in the creep/rupture testing for this research ($<0.3 T_m$) screw dislocations can cross-slip to the latent slip plane. However, Seeger noted that alloying reduces the difference in mobility between screw and non-screw dislocations and that the incorporation of foreign atoms in the screw dislocation

cores may suppress slip in the $\{112\}$ latent slip system.⁵⁵ This is significant because it infers that neutron irradiation defects should inhibit cross-slip of screw dislocations onto a latent slip system, thus slip should primarily occur on the $\{110\}$ family of planes.

Stoller, Wirth and Odette⁵⁶ concluded that irradiation induced defect structures in alloys are responsible for evolution of dislocation structures by impeding dislocation motion thus increasing strength and decreasing ductility. As shown in both sections 5.8 and 5.9, the dislocation activity in creep/tensile tested Ta-10%W and T-111 becomes apparent through the formation of characteristic cellular or subgranular patterns where dislocations arrange in walls at the boundaries of cells/subgrains with relatively low internal dislocation density. This is consistent with the observations of Zinkle and Matsukawa⁴⁴ in which the formation of dislocation cells is favored at low doses and high strains. The driving force behind the creation of a mosaic cells/subgrains has long been unclear.⁵⁷ It is understood that dislocations of the same slip system with the same Burgers vector and slip plane interact weakly.

In conjunction with this evolution in dislocation structure is a corresponding increase in work hardening of the irradiated alloys, which is more pronounced in T-111. Work hardening is the increase of a material's resistance to plastic deformation produced by plastic deformation of metals at temperature below about $0.5 T_m$. It results from increasing numbers of dislocations and dislocation

entanglements which is accompanied by reduction in ductility. During primary creep the work-hardening coefficient is relatively small. However, during secondary creep there is a high degree of work hardening as dislocations operate on mutually intersecting slip planes. As a result, they form junctions by recombination and have to intersect their "forest" dislocations during glide thus leading to subgrain formation. The atomistic nature of the interaction between dislocations and small defect clusters, produced by low temperature neutron irradiation, makes these processes very difficult to study using conventional TEM techniques.

Based on the TEM and electron diffraction analysis coupled with the observation of increased work hardening in the irradiated alloys, it is concluded that the interaction of the defects, produced by an atomic displacement damage of approximately 3.0×10^{-7} dpa, with moving $a_0/2\langle 111 \rangle$ screw dislocations in T-111 results in the formation of dislocation jogs, which causes the screw dislocations to cross-slip on $\{110\}$ family of planes.

CHAPTER VI

SUMMARY AND CONCLUSIONS

"When a man finds a conclusion agreeable, he accepts it without argument, but when he finds it disagreeable, he will bring against it all the forces of logic and reason." - Thucydides

6.1 Summary

The $^{238}\text{PuO}_2$ fuel in a RTG produces significant amounts of alpha-particles and neutron displacement damage. The alpha-particles (helium ions) are produced by the radioactive decay of 238-plutonium and result in increasing pressure within the encapsulation layer of a RTG as the unit ages. The potential material "damage" from the emitted neutrons from the $^{238}\text{PuO}_2$ fuel is a function of the proximity of the $^{238}\text{PuO}_2$ fuel to the encapsulation layer of T-111 or Ta-10%W. As previously discussed, the lack of fundamental understanding of the effect of "RTG levels" of neutron irradiation on the deformation and failure mechanisms in two tantalum alloys (T-111 and Ta-10%W) at irradiation temperatures below 350°C led to the initiation of this research. The objectives of this research that were accomplished are:

1. To characterize the low-temperature creep deformation and failure modes and to develop low-temperature creep/stress rupture data for irradiated Ta-10%W and T-111.
2. Neutron Irradiation - To elucidate the interaction of neutron irradiation damage and low-temperature creep/stress rupture mechanisms for T-111 and Ta-10%W, which are not thoroughly discussed in literature or studied in detail.
3. Irradiation Temperature - To determine the effects of the interaction of irradiation fluence and temperature on the mechanical properties of irradiated Ta-10%W and T-111.

The results of this research accomplished all three stated objectives and provide a basic understanding of the strength mechanisms in two tantalum alloys (Ta-10%W and T-111) resulting from the exposure to neutron fluence levels of approximately 1.2×10^{15} nvt at temperatures below 350°C. This will enhance the level of understanding of potential irradiation hardening mechanisms in both Ta-10%W and T-111 alloys.

Thus, space power system designers can more confidently extrapolate relevant mechanical-property trends of T-111 and Ta-10%W encapsulation materials that are subjected to neutron irradiation doses and internal pressure levels which

correspond to actual RTG service lifetimes. This provides space power system designers with information and material options for future applications that will support ambitious long duration and higher power space related missions.

This understanding of these mechanisms is important for the confident extrapolation of mechanical-property trends to the higher doses and gas levels corresponding to actual service lifetimes. When comparing samples of Ta-10%W and T-111 that were subjected to identical neutron fluences and environmental conditions at temperatures $<0.2T_m$ ($\sim 350^\circ\text{C}$), the mechanical testing data clearly shows that the effects of neutron irradiation are more pronounced on T-111 than Ta-10%W. Although the damage defect structures created by the neutron irradiation are approximately equivalent in both tantalum alloys the resulting lattice strain fields will be greater in T-111 due to the additional lattice strain from the presence of hafnium metalloid impurities in the lattice. This additional lattice strain coupled with neutron irradiation defect structures results in more pronounced dislocation networks and minor changes to mechanical properties in T-111.

6.2 Conclusions

Results obtained in the present research significantly contribute to the state-of-the-art in our understanding of the effects of low levels of neutron irradiation which are equivalent to the cumulative fluence associated with a 30-year mission life of a RTG, on Ta-10%W and T-111 at temperatures less than $<0.2 T_m$. The following important conclusions result from this research:

- 1) Approximately 20 $\mu\text{Ci/g}$ of isotope ^{182}Ta are formed in both Ta-10%W and T-111, and 0.2 $\mu\text{Ci/g}$ of isotope ^{181}Hf is formed in T-111 as a result of the slow-neutron capture process.
- 2) An atomic displacement damage of approximately 3.0×10^{-7} dpa is produced, at a fluence level of 1.2×10^{15} nvt, which results in an estimated observable defect density of 7.35×10^{17} defects/ m^3 in both alloys.
- 3) The oxidation of Ta-10%W and T-111 is non-diffusion controlled and primarily superficial.
- 4) An atomic displacement damage of approximately 3.0×10^{-7} dpa produces an approximate 6.6% reduction in the ductility of T-111 at 25°C when subjected to a strain rate of 0.0017 s^{-1} ; the average reduction in elongation was 0.8039 cm (irradiated) compared to 0.8603 cm (non-irradiated). This

was determined to be a statistically significant effect at the 0.01 significance level.

- 5) The effects of neutron irradiation in T-111 are more pronounced at an irradiation temperature of 350°C than at 108°C. This was determined to be a statistically significant effect at the 0.05 significance level.
- 6) An atomic displacement damage of approximately 3.0×10^{-7} dpa did not produce a statistically significant effect on the tensile properties of Ta-10%W when subjected to a strain rate of 0.0017 s^{-1} .
- 7) An atomic displacement damage of approximately 3.0×10^{-7} dpa produces the following statistically significant effects in the low-temperature creep/stress rupture behavior of T-111 :
 - a. An approximate two-order of magnitude increase in the rupture time from $1.59 \times 10^5 \text{ s}$ (non-irradiated) to $9.3 \times 10^6 \text{ s}$ (irradiated). This was determined to be a statistically significant effect at a 0.0472 significance level; and
 - b. A two-order of magnitude reduction in steady state creep rate from $2.13 \times 10^{-8} \text{ m/s}$ (non-irradiated) to $2.48 \times 10^{-10} \text{ m/s}$

(irradiated). This was determined to be a statistically significant effect at a 0.0572 significance level; and

c. Increase in the stress function from 5.14 to 7.02.

8) An atomic displacement damage of approximately 3.0×10^{-7} dpa produces a more significant effect on the on the steady-state creep rate and rupture time for T-111 than for Ta-10%W when subjected to a load of 620 MPa.

9) The interaction of the defects, produced by an atomic displacement damage of approximately 3.0×10^{-7} dpa, with moving $a_0/2\langle 111 \rangle$ screw dislocations in T-111 results in:

a. The formation of dislocation jogs, which causes the screw dislocations to cross-slip on the $\{110\}$ family of planes; and

b. A five-fold increase in dislocation density from approximately 10^{-16} m^{-2} (non-irradiated) to approximately $5.0 \times 10^{-16} \text{ m}^{-2}$ (irradiated); and

c. The ordering of dislocations into mosaic patterns of cellular or subgranular arrangements at the boundaries of cells/subgrains which have a relatively low internal dislocation density.

- 10) A predictive model was developed from the research data for determining the minimum creep rate (m/s) of irradiated T-111 via the following expression:

$$\dot{\epsilon} = (dpa) 4.33 \times 10^{-10} [\sinh(9.6 \times 10^{-3} \sigma)]^{1.8910} e^{1+dpa(1.04 \times 10^{-6})} e^{-57280/RT}$$

Where,

dpa - Neutron irradiation damage

R - Ideal gas constant (8.3145 J/mole-K)

T - Test temperature in Kelvin

which is valid in the temperature range of 25 to 300°C; stress range of 496 to 690 MPa; and for neutron irradiation damage levels in the 10^{-7} dpa regime.

CHAPTER VII

FUTURE RESEARCH

*"To raise new questions, new possibilities, to regard old problems from a new angle requires creative imagination and marks real advances in science."
- Albert Einstein*

Future research should focus on:

1. High resolution Transmission Electron Microscopy (TEM) of Ta-10%W and T-111 irradiated and non-irradiated mechanically tested specimens in order to quantify differences in relative levels of lattice defects between materials. This will require use of the JEOL 2200FS-AC aberration-corrected STEM/TEM at Oak Ridge national Laboratory. This instrument has an achievable resolution in dark-field imaging of 0.07 nm and the capability to obtain chemical species and bonding information to be obtained from single atomic columns.
2. Determining the influence of increased irradiation temperature from 0.2 – 0.5 T_m on the mechanical properties of Ta-10%W and T-111. This will require the application of an ultra-high vacuum irradiation atmosphere to mitigate potential environmental effects from ppm levels of O, N, C and H₂O.

3. Conduct additional mechanical tests such as creep and stress rupture for Ta-10%W and T-111 in order to determine if any statistically significant differences result from increased irradiation levels. This will require the application of an ultra-high vacuum mechanical testing atmosphere for elevated temperature testing ($>0.2 T_m$) to mitigate potential environment effects from ppm levels of O, N, C and H₂O.
4. Determine the activation energies for dislocation movement of irradiated and non-irradiated Ta-10%W and T-111 for elevated temperatures ($>0.2 T_m$) and irradiation levels.

These recommended efforts will provide a level of understanding of irradiation effects of Ta-10%W and T-111 that will enable more confident extrapolation of relevant mechanical-property data. This could be used to predict end-of-service behavior of components made from these alloys. This will provide space power system designers with information and options for future applications supporting ambitious space-related missions.

REFERENCES

- ¹ Jet Propulsion Laboratory, *NASA Facts -Viking Mission to Mars*, National Aeronautics and Space Administration, California Institute of Technology, Pasadena, CA, 1988.
- ² Bennett, G.L., Skrabek, E.A., "Power Performance of U.S. Space Radioisotope Thermoelectric Generators," in proceedings of *Fifteenth International Conference on Thermoelectrics*, Institute of Electrical and Electronics Engineers (IEEE), New York, NY, 1996, pp. 357-372.
- ³ Jet Propulsion Laboratory, *NASA Fact Sheet – Spacecraft power for Cassini*, National Aeronautics and Space Administration, California Institute of Technology, Pasadena, CA, 1999.
- ⁴ Buckman, R.W. Jr., Ammon, R.L., "Evolution of Tantalum Alloy Development," in proceedings of *Evolution of Refractory Metals and Alloys*, Edited by Dalder, E.N.C., Grobstein, T., and Olsen, C.S., Denver, CO, 1994, pp. 49-83.
- ⁵ Brown, W.F. Jr., Gibson, C., Ho, C.Y., *Aerospace Structural Metals Handbook, Volumes 1 - 5*, CINDAS/USAF CRDA Handbooks Operation, Purdue University, West Lafayette, IN, 1997, pp. 5402/1-5403/10.

- ⁶ Buckman, R.W. Jr., "The Creep Behavior of Refractory Metal Alloys," *International Journal of Refractory Metals & Hard Materials*, **18**, pp. 253-257, (2000).
- ⁷ Lassila, D.H., Schwartz, A.J., LeBlanc, M.M., and Wright, S.I., "Mechanical Behavior of Tantalum and Tantalum-Tungsten Alloys: Texture Gradients and Macro/Micro-Response," UCRL-JC-125692, Lawrence Livermore National Laboratory, Livermore, CA, 1996.
- ⁸ Moorhead, P.E., Stone, P.L., *Survey of Properties of T-111 (Tantalum-8 Tungsten-2 Hafnium)*, NASA/D-5873, NASA Lewis Research Center, Cleveland, OH, 1970.
- ⁹ Sheffler, K. D., Sawyer, J. C., and Steigerwald, E. A., *Mechanical Behavior of Tantalum-Base T-111 Alloy at Elevated Temperature*, NASA/CR-1436, NASA Lewis Research Center, Cleveland, OH, 1969.
- ¹⁰ Wang, J.N., Nieh, T.G., "Role of Peierls stress in power law dislocation creep," *Materials Science and Engineering: A*, 202, 1-2, pp. 52-56 (1995).
- ¹¹ Eylon, D., Course Notes, MAT 535 - High Temperature Materials, University of Dayton, Dayton, OH, 2004.

- ¹² Garofalo, F., *Fundamentals of Creep and Creep Rupture in Metals*, Macmillan, New York, NY, 1965.
- ¹³ Dieter, G.E., *Mechanical Metallurgy*, McGraw-Hill, New York, NY, 1976, pp. 119.
- ¹⁴ Kubin, L.P., Devincre, B., Tang, M., "Mesoscopic Modeling and Simulation of Plasticity in fcc and bcc Crystals: Dislocation Intersections and Mobility," *Journal of Computer-Aided Materials Design*, **5**, pp. 31-54, (1998).
- ¹⁵ Klueh, R.L., "Effect of Neutron Irradiation on Properties of Steels," *ASM Handbook-Volume 1, Properties and Selection: Irons, Steels, and High-Performance Alloys*, ASM International, Materials Park, OH, 2002, pp. 653-661.
- ¹⁶ Zinkle, S. J., Private Communications, Oak Ridge National Laboratory, November 14, 2005.
- ¹⁷ Übeyli, M., "Radiation Damage Study on Various Structural Refractory Alloys of a Multi-Purpose Reactor," *Journal of Fusion Energy*, **22**, pp. 251 – 257, (2003).

- ¹⁸ Hashimoto, N., Byun, T.S, Farrell, K, Zinkle, S.J., "Déformation Microstructure of Neutron-Irradiated Pure Polycrystalline Metals," *Journal of Nuclear Materials*, **329-333**, pp. 947-952, (2004).
- ¹⁹ Pavlov, V.A., Shalaev, V.I., Alyabiev, V.M., "Effect of Dislocation-Structure on Creep and Fracture of Metals and Alloys - 2. Irradiation," *Physica Status Solidi A-Applied Research*, **85**, pp. 315-333 (1984).
- ²⁰ Amos, W.R., *Milli-watt Generator Heat Source Progress Report, July 16, 1976 – October 15, 1976*, MLM-MU-76-70-0003, Monsanto Research Corporation, Miamisburg, OH, 1976.
- ²¹ Duty, C.E., Zinkle, S.J., Luther, R.F., Buckman, R.W., Gold, R.E., Ballout, Y.A., "The Potential of Tantalum Alloys for Space Nuclear Applications," in proceedings of *American Nuclear Society Annual Meeting Embedded Topical: Space Nuclear Power 2005*, La Grange Park, IL, 2005, pp. 294-302.
- ²² Zinkle, S. J., *Thermophysical and Mechanical Properties for Ta-8%W-2%Hf*, DOE/ER-313/27, Oak Ridge National Laboratory, Oak Ridge, TN, 2000.
- ²³ Zinkle, S. J., Ghoniem, N.M., "Operating Temperature Windows for Fusion Reactor Structural Materials," *Fusion Engineering and Design*, **51–52**, pp. 55–71 (2000).

- ²⁴ Howell, E.I., Teaney, P.E., *Development Testing of the Two-Watt RTG Heat Source and Hastelloy-S/T-111 Alloy Compatibility Studies*, MLM-3786, EG&G Mound Applied Technologies, Miamisburg, OH, 1993.
- ²⁵ McCoy, H.E., DiStefano, J.R., *The Mechanical Properties of T-111 at Low to Intermediate Temperatures*, TM-13265, Oak Ridge National Laboratory, Oak Ridge, TN, 1997.
- ²⁶ Ruhkamp, J.D., "Design, Development and Testing of 60-Watt Radioisotope Heat Source Strength Member," in proceedings of 12th symposium on space nuclear power and propulsion, edited by El-Genk, M.S., AIP Conference Proceedings, 324, Melville, NY, 1995, pp. 223-228.
- ²⁷ El-Genk, M.S., Tournier, J., "A Review of Refractory Metal Alloys and Mechanically Alloyed-Oxide Dispersion Strengthened Steels for Space Nuclear Power Systems," *Journal of Nuclear Materials*, **340**, pp. 93-112 (2005).
- ²⁸ ASTM International, *Standard Test Methods for Determining Average grain Size, E112-96*, ASTM International, West Conshohocken, PA, 2006.

- ²⁹ ASTM International, *Standard Test Methods for Tension Testing of Metallic Materials, E8-04*, ASTM International, West Conshohocken, PA, 2004.
- ³⁰ ASTM International, *Standard Test Methods for Conducting Creep, Creep-Rupture, and Stress-Rupture Tests of Metallic Materials, E139-00*, ASTM International, West Conshohocken, PA, 2000.
- ³¹ Inoyue, H., "Interactions of Refractory metals with Active Gases in Vacua and Inert Gas Environments," in proceedings of *Refractory Metal Alloys, Metallurgy and Technology*, edited by Machlin, I., Plenum Press, New York, NY, 1968, pp. 165-196.
- ³² Carpenter, R. W., Liu, C. T., "Surface Reaction Controlled Oxygen Absorption in a Ta-8W-2Hf Alloy: Kinetics and Concentrations Gradients," *Met Trans. A*, **6A**, 2235-2241, (1975).
- ³³ Los Alamos, *238-Plutonium Dioxide Fuel Pellet Specification for General Purpose Heat Source (GPHS)*, NMT9-AP-026, Los Alamos National Laboratory, Los Alamos, NM, 2006.
- ³⁴ Broeders, C.H.M., Konobeyev, A.Y., "Defect Production Efficiency in Metals under Neutron Irradiation," *Journal of Nuclear Materials*, **328**, 197-214, (2004).

- ³⁵ United States Department of Transportation, *General Requirements for Shipments and Packaging*, 49 CFR 173, Washington D.C., 2002.
- ³⁶ Gourdin, W.H., Lassila, D.H., Leblanc, M.M., Shields, A.L., "The Influence of Tungsten Alloying on the Mechanical Properties of Tantalum," *Journal De Physique IV*, **4**, pp. 207-212, (1994).
- ³⁷ Box, G. E. P., Hunter, W. G., and Hunter, J. S. (1978), *Statistics for Experimenters: An Introduction to Design, Data Analysis, and Model Building*, Wiley, New York, NY, 1978.
- ³⁸ General Electric, *Eighth Annual Report, AEC Fuels and Materials Development Program*, GEMP-1012, General Electric Company, Cincinnati, OH, 1969.
- ³⁹ Hampel, C. A., "Rare Metals Handbook," edited by Hampel, C. A., Reinhold Publishing Corporation, New York, NY, 1961, pp. 502-506.
- ⁴⁰ ASTM International, *Standard Practice for Characterizing Neutron Exposures in Iron and Low Alloy Steels in Terms of Displacements Per Atom (DPA)*, E 706(ID), E693-01, ASTM International, West Conshohocken, PA, 2002.
- ⁴¹ Crawford, J.H., Jr., Slifkin, L.M., *Point Defects in Solids*, Plenum, New York, NY, 1972, pp. 278-279.

- ⁴² Saraev, D., Kizler, P., Schmauder, S., "The influence of Frenkel defects on the deformation and fracture of α -Fe single crystals," *Modeling and Simulation in Materials Science and Engineering*, **7**, 6, pp. 1013-1023, (1999).
- ⁴³ Schoeck, G., "Influence of Irradiation on Creep," *J. Appl. Phys.*, **29**, 112, (1958).
- ⁴⁴ Zinkle, S. J., Matsukawa, Y., "Observation and Analysis of Defect Cluster Production and Interactions with Dislocations," *Journal of Nuclear Materials*, **329-333**, 88-96, (2004).
- ⁴⁵ Zinkle, S. J., Hashimoto, N., Matsukawa, Y., Stoller, R.E., and Osetsky, Y. N., "Microstructures of Irradiated and Mechanically Deformed Metals and Alloys: Fundamental Aspects", in proceedings of *Radiation Effects and Ion Beam Processing of Materials*, edited by Wang, L.M., et al., Materials Research Society, 792, Warrendale, PA, 2004, pp. 1-10.
- ⁴⁶ Singh, B.N., Zinkle, S.J., "Influence of Irradiation Parameters on Damage Accumulation in Metals and Alloys," *Journal of Nuclear Materials*, **217**, 1-2, pp. 161-171 (1994).

- ⁴⁷ Hatcher, L., Stepanski, E. J., "A Step-By-Step Approach to Using the SAS System for Univariate and Multivariate Statistics, SAS Institute, Cary, NC, 1994.
- ⁴⁸ Kerlins, V., Phillips, A., "Modes of Fracture," *ASM Handbook-Volume 12, Fractography*, ASM International, Materials Park, OH, 2002, pp. 12-71.
- ⁴⁹ Eylon, D., Course Notes, MAT 576/576 – Fracture and Fatigue of metal and Alloys I/II, University of Dayton, Dayton, OH, 1990.
- ⁵⁰ Eichen, E., Laird, C., and Bitler, W.R., *Reciprocal Lattice Diffraction Patterns for FCC, BCC, HCP, and Diamond Cubic Crystal Systems*, Department of Metallurgy, Pennsylvania State University, University Park, PA, 1965.
- ⁵¹ Winther, G., "Slip Patterns and Preferred Dislocation Boundary Planes," *Acta Materialia*, 51, pp. 417-429, (2003).
- ⁵² Bentley, J., Private Communications, Oak Ridge National Laboratory, November 20, 2006.
- ⁵³ Granato, A. Lücke, K., "Theory of Mechanical Dampening due to Dislocations," *Journal of Physics*, **27**, pp. 583-593, (1956).

- ⁵⁴ Yang, L.H., Moriarty, J.A., "Kink-Pair Mechanisms for $a/2$ $\langle 111 \rangle$ Screw Dislocation Motion in BCC Tantalum," *Materials Science and Engineering*, **319-321**, pp. 124 – 129 (2001).
- ⁵⁵ Seeger, A., "Why Anomalous Slip in Body-Centered Cubic Metals?," *Materials Science and Engineering*, **319-321**, pp. 254-260 (2001).
- ⁵⁶ Stoller, R.E., Wirth, B.D., Odette, G.R., "Primary Damage Formation in BCC Iron," *Journal of Nuclear Materials*, **251**, pp. 49-60 (1997).
- ⁵⁷ Sedlacek, R., Blum, W., Kratochvíl, J., Forest, S., "Subgrain Formation during Deformation: Physical Origin and Consequences," *Trans. A*, **33A**, 319-327, (2002).

APPENDIX A
Gamma Spectrometry
Data

Dogbone 8C
May/16/2006 9:47:34AM

HEADER INFORMATION in MCard#2 Dogbone 8C

Identification	Acquisition
User : J. Talnagi	Started : May/16/2006 9:45:
MCard : 2	Stopped : May/16/2006 9:46:
Detector : HPGe	True Time : 72.282 sec
Geometry : 8	Live Time : 25.770 sec
Sample : 8C	Dead Time : 64.35 %
Channels : 8192	Gross Count : 1255184 counts
	Gross Rate : 48707.2 cps

Sample

Sampled from May/16/2006 9:45:02AM to May/16/2006 9:45:02AM
Total Quantity 1 ± 0%

Energy Calibration Jun/5/2003 8:30:29AM ENCAL.S0
Resolution Calibration Jun/5/2003 8:35:27AM ENCAL.S0
Efficiency Calibration Oct/14/2002 10:15:20AM GEOMET-1.S0
Isotope Library ISOTOPE.LIB Oct/26/2005 9:42:31AM

ACTIVITY INFORMATION for MCard#2 Dogbone 8C

Name	Energy keV	Activity Flag uCi	Error
Ta-182	84.68	64.74	± 18.85%
Ta-182	100.11	60.07	± 5.98%
Ta-182	113.67	77.90	± 16.75%
Ta-182	152.43	119.3	± 9.28%
Ta-182	156.38	123.8	± 10.65%
Ta-182	179.39	143.9	± 10.91%
Ta-182	198.35	132.5	± 13.75%
Ta-182	222.10	173.3	± 10.79%
Ta-182	229.32	187.8	± 11.50%
Ta-182	264.07	172.0	± 12.44%
Ta-182	1001.68	181.7	± 25.60%
Ta-182	1121.28	204.6	± 20.91%
Ta-182	1157.40	162.9	± 35.54%
Ta-182	1189.05	195.3	± 21.49%
Ta-182	1221.42	201.3	± 21.61%
Ta-182	1230.97	201.3	± 21.90%
Ta-182	1257.47	195.9	± 28.39%
Ta-182	1289.17	210.7	± 28.36%
Weighted Average		172.9	± 17.92%
Grand Total		172.9	± 17.92%

Activity (uCi) at May/16/2006 9:45:02AM
Errors Quoted at 2 Sigma
MDA's Quoted at 1.645 Sigma

Figure A.1. Gamma-spectrometry Results for Irradiated Ta-10%W Mechanical Test Specimen 8C.

T6C Dogbone
May/16/2006 10:29:07AM

HEADER INFORMATION in MCard#2 T6C Dogbone

Identification	Acquisition
User : J. Tainagi	Started : May/16/2006 10:24
MCard : 2	Stopped : May/16/2006 10:28
Detector : HPGe	True Time : 225.348 sec
Geometry : 8	Live Time : 126.260 sec
Sample : T6C Dogbone	Dead Time : 43.97 %
Channels : 8192	Gross Count : 3585401 counts
	Gross Rate : 28397 cps

Sample

Sampled from May/16/2006 10:24:36AM to May/16/2006 10:24:36AM
Total Quantity 1 ± 0%

Energy Calibration Jun/5/2003 8:30:29AM ENCAL.S0
Resolution Calibration Jun/5/2003 8:35:27AM ENCAL.S0
Efficiency Calibration Oct/14/2002 10:15:20AM GEOMET-1.S0
Isotope Library ISOTOPE.LIB Oct/26/2005 9:42:31AM

ACTIVITY INFORMATION for MCard#2 T6C Dogbone

Name	Energy keV	Activity Flag uCi	Error
Hf-181	133.05	0.9316	± 24.54%
Hf-181	482.16	1.236	± 17.83%
Weighted Average		1.135	± 20.07%
Ta-182	84.68	48.25	± 13.78%
Ta-182	100.11	43.14	± 5.11%
Ta-182	113.67	59.52	± 9.82%
Ta-182	152.43	87.02	± 8.93%
Ta-182	156.38	88.45	± 9.42%
Ta-182	179.39	102.8	± 9.87%
Ta-182	198.35	108.2	± 11.03%
Ta-182	222.10	127.5	± 10.60%
Ta-182	229.32	133.0	± 10.91%
Ta-182	264.07	137.4	± 11.61%
Ta-182	1001.68	169.8	± 21.33%
Ta-182	1121.28	153.7	± 20.85%
Ta-182	1157.40	155.5	± 23.31%
Ta-182	1189.05	150.3	± 21.35%
Ta-182	1221.42	151.3	± 21.54%
Ta-182	1230.97	155.9	± 21.65%
Ta-182	1257.47	139.7	± 23.03%
Ta-182	1273.70	135.2	± 26.81%
Ta-182	1289.17	136.7	± 23.41%
Weighted Average		130.6	± 17.24%
Grand Total		131.7	± 17.09%

Activity (uCi) at May/16/2006 10:24:36AM
Errors Quoted at 2 Sigma

Figure A.2. Gamma-spectrometry Results for Irradiated T-111 Mechanical Test Specimen T6C.

APPENDIX B
Tensile Test ANOVA
Data

The SAS System
The GLM Procedure T-111

Class Level Information

Class	Levels	Values
Rad	2	-1 1
Rad_Temp	2	-1 1
Tensile_Temp	2	-1 1

Number of observations 8

Dependent variable: Yield

Source	DF	Sum of Squares	Mean Square	F Value	Pr > F
Model	4	1586.191250	396.547813	23.82	0.0131
Error	3	49.946550	16.648850		
Corrected Total	7	1636.137800			

R-Square	Coeff Var	Root MSE	Yield Mean
0.969473	5.171155	4.080300	78.90500

Source	DF	Type I SS	Mean Square	F Value	Pr > F
Rad	1	1.584200	1.584200	0.10	0.7779
Rad_Temp	1	0.561800	0.561800	0.03	0.8660
Rad*Rad_Temp	1	14.364800	14.364800	0.86	0.4215
Tensile_Temp	1	1569.680450	1569.680450	94.28	0.0023

Source	DF	Type III SS	Mean Square	F Value	Pr > F
Rad	1	1.584200	1.584200	0.10	0.7779
Rad_Temp	1	0.561800	0.561800	0.03	0.8660
Rad*Rad_Temp	1	14.364800	14.364800	0.86	0.4215
Tensile_Temp	1	1569.680450	1569.680450	94.28	0.0023

The GLM Procedure T-111

Level of Rad	N	-----Yield----- Mean	Std Dev
-1	4	79.350000	15.4440258
1	4	78.460000	17.5023789

Level of Rad_Temp	N	-----Yield----- Mean	Std Dev
-1	4	79.170000	13.8344040
1	4	78.640000	18.8096057

Level of Rad	Level of Rad_Temp	N	-----Yield----- Mean	Std Dev
-1	-1	2	80.955000	14.6017550
-1	1	2	77.745000	22.1819397
1	-1	2	77.385000	18.6605480
1	1	2	79.535000	23.7941432

Level of Tensile_Temp	N	-----Yield----- Mean	Std Dev
-1	4	92.912500	2.59863265
1	4	64.897500	3.92422710

The GLM Procedure T-111

Dependent Variable: UTS

Source	DF	Sum of Squares	Mean Square	F Value	Pr > F
Model	4	1478.569250	369.642313	26.12	0.0115
Error	3	42.450137	14.150046		
Corrected Total	7	1521.019387			

R-Square	Coeff Var	Root MSE	UTS Mean
0.972091	4.177122	3.761655	90.05375

Source	DF	Type I SS	Mean Square	F Value	Pr > F
Rad	1	0.277513	0.277513	0.02	0.8975
Rad_Temp	1	1.336613	1.336613	0.09	0.7787
Rad*Rad_Temp	1	3.524512	3.524512	0.25	0.6520
Tensile_Temp	1	1473.430613	1473.430613	104.13	0.0020

Source	DF	Type III SS	Mean Square	F Value	Pr > F
Rad	1	0.277513	0.277513	0.02	0.8975
Rad_Temp	1	1.336612	1.336612	0.09	0.7787
Rad*Rad_Temp	1	3.524513	3.524513	0.25	0.6520
Tensile_Temp	1	1473.430613	1473.430613	104.13	0.0020

The GLM Procedure T-111

Level of Rad	N	-----UTS-----	-----
		Mean	Std Dev
-1	4	90.240000	14.9199710
1	4	89.8675000	16.8614479

Level of Rad_Temp	N	-----UTS-----	-----
		Mean	Std Dev
-1	4	89.6450000	13.2661336
1	4	90.4625000	18.1816013

Level of Rad	Level of Rad_Temp	N	-----UTS-----	-----
			Mean	Std Dev
-1	-1	2	90.4950000	14.9411663
-1	1	2	89.9850000	21.0788531
1	-1	2	88.7950000	17.3736136
1	1	2	90.9400000	23.3769502

Level of Tensile_Temp	N	-----UTS-----	-----
		Mean	Std Dev
-1	4	103.625000	3.13265063
1	4	76.482500	2.45955789

The GLM Procedure T-111

Dependent Variable: Modulus

Source	DF	Sum of Squares	Mean Square	F Value	Pr > F
Model	4	74053.6851	18513.4213	1.06	0.5021
Error	3	52556.0392	17518.6797		
Corrected Total	7	126609.7243			

R-Square	Coeff Var	Root MSE	Modulus Mean
0.584897	8.594692	132.3581	1539.999

Source	DF	Type I SS	Mean Square	F Value	Pr > F
Rad	1	66097.02611	66097.02611	3.77	0.1474
Rad_Temp	1	5256.71311	5256.71311	0.30	0.6220
Rad*Rad_Temp	1	1692.16531	1692.16531	0.10	0.7763
Tensile_Temp	1	1007.78051	1007.78051	0.06	0.8259

Source	DF	Type III SS	Mean Square	F Value	Pr > F
Rad	1	66097.02611	66097.02611	3.77	0.1474
Rad_Temp	1	5256.71311	5256.71311	0.30	0.6220
Rad*Rad_Temp	1	1692.16531	1692.16531	0.10	0.7763
Tensile_Temp	1	1007.78051	1007.78051	0.06	0.8259

The GLM Procedure T-111

Level of Rad	N	-----Modulus-----	
		Mean	Std Dev
-1	4	1449.10250	89.506135
1	4	1630.89500	110.270355

Level of Rad_Temp	N	-----Modulus-----	
		Mean	Std Dev
-1	4	1565.63250	152.460961
1	4	1514.36500	131.174155

Level of Rad	Level of Rad_Temp	N	-----Modulus-----	
			Mean	Std Dev
-1	-1	2	1489.28000	122.357757
-1	1	2	1408.92500	51.046039
1	-1	2	1641.98500	177.321168
1	1	2	1619.80500	67.408489

Level of Tensile_Temp	N	-----Modulus-----	
		Mean	Std Dev
-1	4	1551.22250	94.154524
1	4	1528.77500	181.665187

The GLM Procedure T-111

Dependent Variable: Elongation

Source	DF	Sum of Squares	Mean Square	F Value	Pr > F
Model	4	0.01834481	0.00458620	79.27	0.0023
Error	3	0.00017358	0.00005786		
Corrected Total	7	0.01851838			

R-Square	Coeff Var	Root MSE	Elongation Mean
0.990627	2.682111	0.007606	0.283600

Source	DF	Type I SS	Mean Square	F Value	Pr > F
Rad	1	0.00061952	0.00061952	10.71	0.0467
Rad_Temp	1	0.00217800	0.00217800	37.64	0.0087
Rad*Rad_Temp	1	0.00007688	0.00007688	1.33	0.3325
Tensile_Temp	1	0.01547041	0.01547041	267.38	0.0005

Source	DF	Type III SS	Mean Square	F Value	Pr > F
Rad	1	0.00061952	0.00061952	10.71	0.0467
Rad_Temp	1	0.00217800	0.00217800	37.64	0.0087
Rad*Rad_Temp	1	0.00007688	0.00007688	1.33	0.3325
Tensile_Temp	1	0.01547041	0.01547041	267.38	0.0005

The GLM Procedure T-111

Level of Rad	N	-----Elongation-----	
		Mean	Std Dev
-1	4	0.29240000	0.05567315
1	4	0.27480000	0.05354238

Level of Rad_Temp	N	-----Elongation-----	
		Mean	Std Dev
-1	4	0.30010000	0.05280802
1	4	0.26710000	0.05155683

Level of Rad	Level of Rad_Temp	N	-----Elongation-----	
			Mean	Std Dev
-1	-1	2	0.30580000	0.06194255
-1	1	2	0.27900000	0.06887220
1	-1	2	0.29440000	0.06632662
1	1	2	0.25520000	0.05161880

Level of Tensile_Temp	N	-----Elongation-----	
		Mean	Std Dev
-1	4	0.32757500	0.02556369
1	4	0.23962500	0.01903915

The GLM Procedure Ta-10%w

Class Level Information

Class	Levels	Values
Rad	2	-1 1
Rad_Temp	2	-1 1
Tensile_Temp	2	-1 1

Number of observations 8

Dependent Variable: Yield

Source	DF	Sum of Squares	Mean Square	F Value	Pr > F
Model	4	1293.469950	323.367488	22.66	0.0141
Error	3	42.811937	14.270646		
Corrected Total	7	1336.281888			

R-Square	Coeff Var	Root MSE	Yield Mean
0.967962	4.289434	3.777651	88.06875

Source	DF	Type I SS	Mean Square	F Value	Pr > F
Rad	1	5.461513	5.461513	0.38	0.5800
Rad_Temp	1	1.487813	1.487813	0.10	0.7680
Rad*Rad_Temp	1	0.007813	0.007813	0.00	0.9828
Tensile_Temp	1	1286.512813	1286.512813	90.15	0.0025

Source	DF	Type III SS	Mean Square	F Value	Pr > F
Rad	1	5.461512	5.461512	0.38	0.5800
Rad_Temp	1	1.487812	1.487812	0.10	0.7680
Rad*Rad_Temp	1	0.007813	0.007813	0.00	0.9828
Tensile_Temp	1	1286.512813	1286.512813	90.15	0.0025

The GLM Procedure Ta-10%w

Level of Rad	N	-----Yield-----	
		Mean	Std Dev
-1	4	87.2425000	15.4500429
1	4	88.8950000	14.3144321

Level of Rad_Temp	N	-----Yield-----	
		Mean	Std Dev
-1	4	87.6375000	13.4987589
1	4	88.5000000	16.2084813

Level of Rad	Level of Rad_Temp	N	-----Yield-----	
			Mean	Std Dev
-1	-1	2	86.7800000	19.6151421
-1	1	2	87.7050000	18.1797153
1	-1	2	88.4950000	12.6077139
1	1	2	89.2950000	21.3334116

Level of Tensile_Temp	N	-----Yield-----	
		Mean	Std Dev
-1	4	100.750000	2.85064905
1	4	75.387500	2.90920808

The GLM Procedure Ta-10%w

Dependent Variable: UTS

Source	DF	Sum of Squares	Mean Square	F Value	Pr > F
Model	4	831.4691000	207.8672750	396.93	0.0002
Error	3	1.5710500	0.5236833		
Corrected Total	7	833.0401500			

R-Square	Coeff Var	Root MSE	UTS Mean
0.998114	0.738899	0.723660	97.93750

Source	DF	Type I SS	Mean Square	F Value	Pr > F
Rad	1	1.8240500	1.8240500	3.48	0.1588
Rad_Temp	1	14.3648000	14.3648000	27.43	0.0135
Rad*Rad_Temp	1	2.8322000	2.8322000	5.41	0.1026
Tensile_Temp	1	812.4480500	812.4480500	1551.41	<.0001

Source	DF	Type III SS	Mean Square	F Value	Pr > F
Rad	1	1.8240500	1.8240500	3.48	0.1588
Rad_Temp	1	14.3648000	14.3648000	27.43	0.0135
Rad*Rad_Temp	1	2.8322000	2.8322000	5.41	0.1026
Tensile_Temp	1	812.4480500	812.4480500	1551.41	<.0001

The GLM Procedure Ta-10%w

Level of Rad	N	-----UTS----- Mean	Std Dev
-1	4	97.460000	11.5453627
1	4	98.415000	11.9906894

Level of Rad_Temp	N	-----UTS----- Mean	Std Dev
-1	4	96.5975000	11.2225885
1	4	99.2775000	12.1220993

Level of Rad	Level of Rad_Temp	N	-----UTS----- Mean	Std Dev
-1	-1	2	96.715000	13.9229325
-1	1	2	98.205000	14.2764859
1	-1	2	96.480000	13.5623081
1	1	2	100.350000	15.2452222

Level of Tensile_Temp	N	-----UTS----- Mean	Std Dev
-1	4	108.015000	2.28651846
1	4	87.860000	1.27901003

The GLM Procedure Ta-10%W

Dependent Variable: Modulus

Source	DF	Sum of Squares	Mean Square	F Value	Pr > F
Model	4	459518.3723	114879.5931	1.93	0.3080
Error	3	178622.5555	59540.8518		
Corrected Total	7	638140.9278			

R-Square	Coeff Var	Root MSE	Modulus Mean
0.720089	14.58948	244.0099	1672.506

Source	DF	Type I SS	Mean Square	F Value	Pr > F
Rad	1	73243.0401	73243.0401	1.23	0.3483
Rad_Temp	1	179637.1830	179637.1830	3.02	0.1808
Rad*Rad_Temp	1	50646.3051	50646.3051	0.85	0.4244
Tensile_Temp	1	155991.8440	155991.8440	2.62	0.2040

Source	DF	Type III SS	Mean Square	F Value	Pr > F
Rad	1	73243.0401	73243.0401	1.23	0.3483
Rad_Temp	1	179637.1830	179637.1830	3.02	0.1808
Rad*Rad_Temp	1	50646.3051	50646.3051	0.85	0.4244
Tensile_Temp	1	155991.8440	155991.8440	2.62	0.2040

The GLM Procedure Ta-10%w

Level of Rad	N	-----Modulus-----	
		Mean	Std Dev
-1	4	1576.82250	127.948596
1	4	1768.19000	414.642560

Level of Rad_Temp	N	-----Modulus-----	
		Mean	Std Dev
-1	4	1822.35500	388.845016
1	4	1522.65750	40.424439

Level of Rad	Level of Rad_Temp	N	-----Modulus-----	
			Mean	Std Dev
-1	-1	2	1647.10500	160.605163
-1	1	2	1506.54000	59.665670
1	-1	2	1997.60500	552.229183
1	1	2	1538.77500	17.416040

Level of Tensile_Temp	N	-----Modulus-----	
		Mean	Std Dev
-1	4	1532.86750	58.451090
1	4	1812.14500	396.610428

The GLM Procedure Ta-10%W

Dependent Variable: Elongation

Source	DF	Sum of Squares	Mean Square	F Value	Pr > F
Model	4	0.01909326	0.00477332	57.78	0.0036
Error	3	0.00024782	0.00008261		
Corrected Total	7	0.01934108			

R-Square	Coeff Var	Root MSE	Elongation Mean
0.987187	4.517822	0.009089	0.201175

Source	DF	Type I SS	Mean Square	F Value	Pr > F
Rad	1	0.00000181	0.00000181	0.02	0.8919
Rad_Temp	1	0.00018241	0.00018241	2.21	0.2340
Rad*Rad_Temp	1	0.00003281	0.00003281	0.40	0.5733
Tensile_Temp	1	0.01887625	0.01887625	228.51	0.0006

Source	DF	Type III SS	Mean Square	F Value	Pr > F
Rad	1	0.00000180	0.00000180	0.02	0.8919
Rad_Temp	1	0.00018240	0.00018240	2.21	0.2340
Rad*Rad_Temp	1	0.00003281	0.00003281	0.40	0.5733
Tensile_Temp	1	0.01887625	0.01887625	228.51	0.0006

The GLM Procedure Ta-10%w

Level of Rad	N	-----Elongation-----	
		Mean	Std Dev
-1	4	0.20165000	0.05761889
1	4	0.20070000	0.05591500

Level of Rad_Temp	N	-----Elongation-----	
		Mean	Std Dev
-1	4	0.20595000	0.06234594
1	4	0.19640000	0.04999207

Level of Rad	Level of Rad_Temp	N	-----Elongation-----	
			Mean	Std Dev
-1	-1	2	0.20845000	0.07898383
-1	1	2	0.19485000	0.05946768
1	-1	2	0.20345000	0.07346839
1	1	2	0.19795000	0.06286179

Level of Tensile_Temp	N	-----Elongation-----	
		Mean	Std Dev
-1	4	0.24975000	0.01242001
1	4	0.15260000	0.00082865

APPENDIX C
Creep/Stress Rupture
Test ANOVA Data

The GLM Procedure

Class Level Information

Class	Levels	Values
Hf	2	-1 1
Rad	2	-1 1
Rad_Temp	2	-1 1
Load	2	-1 1

Number of observations 8

Dependent Variable: Rupture_Time

Source	DF	Sum of Squares	Mean Square	F Value	Pr > F
Model	5	1.3829093E15	2.7658186E14	17.02	0.0564
Error	2	3.2491995E13	1.6245998E13		
Corrected Total	7	1.4154013E15			

R-Square	Coeff Var	Root MSE	Rupture_Time Mean
0.977044	42.75905	4030632	9426384

Source	DF	Type I SS	Mean Square	F Value	Pr > F
Hf	1	3.2885388E14	3.2885388E14	20.24	0.0460
Rad	1	1.8244325E13	1.8244325E13	1.12	0.4003
Rad_Temp	1	1.8247242E13	1.8247242E13	1.12	0.4003
Rad*Rad_Temp	1	3.1992323E14	3.1992323E14	19.69	0.0472
Load	1	6.9764062E14	6.9764062E14	42.94	0.0225

Source	DF	Type III SS	Mean Square	F Value	Pr > F
Hf	1	3.2885388E14	3.2885388E14	20.24	0.0460
Rad	1	1.8244325E13	1.8244325E13	1.12	0.4003
Rad_Temp	1	1.8247242E13	1.8247242E13	1.12	0.4003
Rad*Rad_Temp	1	3.1992323E14	3.1992323E14	19.69	0.0472
Load	1	6.9764062E14	6.9764062E14	42.94	0.0225

The GLM Procedure

Level of Hf	N	-----Rupture_Time----- Mean Std Dev	
-1	4	15837837.5	18085642.2
1	4	3014930.8	5923851.6

Level of Rad	N	-----Rupture_Time----- Mean Std Dev	
-1	4	7916238.3	15722680.0
1	4	10936530.0	14782297.5

Level of Rad_Temp	N	-----Rupture_Time----- Mean Std Dev	
-1	4	7916117.5	15722761.0
1	4	10936650.8	14782178.4

Level of Rad	Level of Rad_Temp	N	-----Rupture_Time----- Mean Std Dev	
-1	-1	2	82175.0	108647.0
-1	1	2	15750301.5	22273437.2
1	-1	2	15750060.0	22273778.8
1	1	2	6123000.0	8169911.7

Level of Load	N	-----Rupture_Time----- Mean Std Dev	
-1	4	18764750.0	15466866.9
1	4	88018.3	172004.0

The GLM Procedure

Dependent Variable: Elongation

Source	DF	Sum of Squares	Mean Square	F Value	Pr > F
Model	5	0.07650680	0.01530136	0.98	0.5756
Error	2	0.03128475	0.01564238		
Corrected Total	7	0.10779155			

R-Square	Coeff Var	Root MSE	Elongation Mean
0.709766	22.21927	0.125069	0.562888

Source	DF	Type I SS	Mean Square	F Value	Pr > F
Hf	1	0.01183491	0.01183491	0.76	0.4761
Rad	1	0.00256686	0.00256686	0.16	0.7246
Rad_Temp	1	0.03946645	0.03946645	2.52	0.2531
Rad*Rad_Temp	1	0.00408156	0.00408156	0.26	0.6603
Load	1	0.01855701	0.01855701	1.19	0.3898

Source	DF	Type III SS	Mean Square	F Value	Pr > F
Hf	1	0.01183491	0.01183491	0.76	0.4761
Rad	1	0.00256686	0.00256686	0.16	0.7246
Rad_Temp	1	0.03946645	0.03946645	2.52	0.2531
Rad*Rad_Temp	1	0.00408156	0.00408156	0.26	0.6603
Load	1	0.01855701	0.01855701	1.19	0.3898

The GLM Procedure

Level of Hf	N	-----Elongation-----	
		Mean	Std Dev
-1	4	0.52442500	0.05681821
1	4	0.60135000	0.16957959

Level of Rad	N	-----Elongation-----	
		Mean	Std Dev
-1	4	0.54497500	0.14861098
1	4	0.58080000	0.11397225

Level of Rad_Temp	N	-----Elongation-----	
		Mean	Std Dev
-1	4	0.63312500	0.09135412
1	4	0.49265000	0.12012267

Level of Rad	Level of Rad_Temp	N	-----Elongation-----	
			Mean	Std Dev
-1	-1	2	0.63780000	0.11242998
-1	1	2	0.45215000	0.13838080
1	-1	2	0.62845000	0.11094505
1	1	2	0.53315000	0.13258252

Level of Load	N	-----Elongation-----	
		Mean	Std Dev
-1	4	0.61105000	0.07957070
1	4	0.51472500	0.15301421

The GLM Procedure

Dependent Variable: Creep_Rate

Source	DF	Sum of Squares	Mean Square	F Value	Pr > F
Model	5	1.9788122E21	3.9576244E20	13.58	0.0700
Error	2	5.8271846E19	2.9135923E19		
Corrected Total	7	2.037084E21			

R-Square	Coeff Var	Root MSE	Creep_Rate Mean
0.971394	48.53894	5397770204	1.11205E10

Source	DF	Type I SS	Mean Square	F Value	Pr > F
Hf	1	4.7024871E20	4.7024871E20	16.14	0.0567
Rad	1	5.5822392E19	5.5822392E19	1.92	0.3005
Rad_Temp	1	4.4023768E18	4.4023768E18	0.15	0.7350
Rad*Rad_Temp	1	4.6571901E20	4.6571901E20	15.98	0.0572
Load	1	9.8261969E20	9.8261969E20	33.73	0.0284

Source	DF	Type III SS	Mean Square	F Value	Pr > F
Hf	1	4.7024871E20	4.7024871E20	16.14	0.0567
Rad	1	5.5822392E19	5.5822392E19	1.92	0.3005
Rad_Temp	1	4.4023768E18	4.4023768E18	0.15	0.7350
Rad*Rad_Temp	1	4.6571901E20	4.6571901E20	15.98	0.0572
Load	1	9.8261969E20	9.8261969E20	33.73	0.0284

The GLM Procedure

Level of Hf	N	-----Creep_Rate-----	
		Mean	Std Dev
-1	4	1.878738E+10	2.182918E+10
1	4	3.453612E+09	6.764999E+09

Level of Rad	N	-----Creep_Rate-----	
		Mean	Std Dev
-1	4	8.478943E+09	1.681433E+10
1	4	1.376205E+10	1.943447E+10

Level of Rad_Temp	N	-----Creep_Rate-----	
		Mean	Std Dev
-1	4	1.037867E+10	2.061446E+10
1	4	1.186232E+10	1.589354E+10

Level of Rad	Level of Rad_Temp	N	-----Creep_Rate-----	
			Mean	Std Dev
-1	-1	2	1.072550E+08	1.495460E+08
-1	1	2	1.685063E+10	2.382861E+10
1	-1	2	2.065009E+10	2.920338E+10
1	1	2	6.874000E+09	9.512000E+09

Level of Load	N	-----Creep_Rate-----	
		Mean	Std Dev
-1	4	2.220325E+10	1.874787E+10
1	4	3.773975E+07	7.350907E+07

DISCLAIMER

This report was prepared as an account of work sponsored by an agency of the United States Government. Neither the United States Government nor any agency thereof, nor any of their employees, makes any warranty, expressed or implied, or assumes any legal liability or responsibility for the accuracy, completeness, or usefulness of any information, apparatus, product, or process disclosed, or represents that its use would not infringe privately owned rights. Reference herein to any specific commercial product, process, or service by trade name, trademark, manufacturer, or otherwise, does not necessarily constitute or imply its endorsement, recommendation, or favoring by the United States Government or any agency thereof. The views and opinions of authors expressed herein do not necessarily state or reflect those of the United States Government or any agency thereof.

R702033432